PROMPT D^0 MESON NUCLEAR MODIFICATION FACTOR AND AZIMUTHAL ANISOTROPY IN HEAVY ION COLLISIONS WITH CMS

A Dissertation

Submitted to the Faculty

of

Purdue University

by

Jian Sun

In Partial Fulfillment of the

Requirements for the Degree

of

Doctor of Philosophy

May 2018

Purdue University

West Lafayette, Indiana

ACKNOWLEDGMENTS

The work in this thesis would not be possible without the great assistance and support from my family, my adviser, colleagues and friends. I am fortunate to have these amazing people on my journey towards the doctoral degree.

First and foremost, I would like to thank my parents and my wife for their support, encouragement, love and understanding. My parents have raised me and have always been there for me, providing both emotional and financial assistance during my undergraduate and graduate studies. My wife, Xingyun Zhao, has also been incredibly supportive and patient in the past years as I have worked and traveled to complete the work in this thesis.

I would like to express my sincere gratitude to my adviser, Professor Wei Xie, for his persistent support and guidance with my research and career over years. Prof. Xie has taught me what it means to be a physicist, how to approach a problem from an unbiased perspective, and how to overcome the bottlenecks with persistent effort and inspiring ideas. I also would like to thank Professor Fuqiang Wang for his helpful advice and discussions on my research, and Professor Martin Kruczenski and Professor Denes Molnar for serving on my thesis committee.

It has been a great experience to study and work in the heavy ion physics group at Purdue. I would like to express my thanks to the graduate and postdoctoral group members for the daily discussions: Kurt Jung, Lingshan Xu, Hao Qiu, Kun Jiang, Li Yi, Liang He, Deke Sun, Cheng-Chieh Peng, Rui Xiao, Jie Zhao, Terrence Edmonds, Liang Zhang, and An Gu. They have made the office hours enjoyable. I would like to thank Kurt Jung and LingShan Xu for teaching me the CMS software and providing help at the beginning of my studies, and Hao Qiu for contributing to part of the work in this thesis. I also would like to thank my other friends at Purdue, who have made the PhD life full of fun.

I also would like to thank the CMS collaborators from other institutions, who constributed part of the work presented in this thesis: Jing Wang, Ta-Wei Wang, Gian Michele Innocenti, Quan Wang, Yen-Jie Lee, and Stephen James Sanders. I also would like to acknowledge the people, who were involved in the LHC operation, CMS data taking, and software development. Without their effort, there would not be the high quality data, with which my thesis work is performed.

TABLE OF CONTENTS

Page

LIST OF TABLES

LIST OF FIGURES

Figure Page

ABSTRACT

Sun, Jian PhD, Purdue University, May 2018. Prompt D^0 Meson Nuclear Modification Factor and Azimuthal Anisotropy in Heavy Ion Collisions with CMS . Major Professor: Wei Xie.

The primary goal of heavy ion physics is to study the properties of the Quark Gluon Plasma (QGP), a state of matter comprising deconfined quarks and gluons. Heavy quarks (charm and bottom) are effective probes to study the properties of the QGP produced in heavy ion collisions. Because of their large masses, heavy quarks are primarily produced via initial hard scatterings in heavy ion collisions. They are expected to interact with the QGP differently than light quarks and gluons. The comparison between the nuclear modification factors of heavy flavor and light hadrons can provide insights into the expected flavor dependence of parton energy loss. The azimuthal anisotropy of heavy flavor hadrons can help quantify the interaction strength between the heavy quarks and the QGP medium at low transverse momentum (p_{T}), and provide unique information about the path length dependence of heavy quark energy loss at high p_{T}.

This dissertation presents the measurements of the prompt D^0 meson nuclear modification factor (R_{AA}) and azimuthal anisotropy coefficients v_2 and v_3 in PbPb collisions with the CMS detector at the CERN LHC. The D^0 meson production is found to be strongly suppressed in heavy ion collisions and the suppression has strong dependence on centrality and p_{T}. The suppression of D^0 mesons is consistent with that of light hadrons for $p_{\mathrm{T}} > 5$ GeV/c, while a hint of smaller supression is observed for $p_{\mathrm{T}} < 5$ GeV/c. The v_2 values are found to be positive in the p_{T} range of 1 to 40 GeV/c. The v_3 is measured for the first time and positive values are observed for $p_{\mathrm{T}} < 6$ GeV/c. Compared to those of light hadrons, the D^0 meson v_2 and v_3 coefficients are found to be smaller for $p_{\mathrm{T}} < 6$ GeV/c. Through the comparison with

theoretical calculations, the v_2 and v_3 results at low p_{T} suggest that the charm quarks take part in the collective motion of the medium. The R_{AA}, v_2, and v_3 results provide new constraints on the models of the interactions between the charm quarks and the QGP medium, and the charm quark energy loss mechanisms.

1. Introduction

This chapter presents the theoretical basis of the experimental studies in this dissertation.

1.1 Standard Model

One of the major goals of physics is to explore the elementary particles and fundamental principles of the universe. A remarkable picture of the fundamental structure of matter is formed by the efforts of generations of physicists. It is found that a few elementary particles (six types of quarks, six types of leptons, four types of force carrier particles, and the Higgs particle) are the basic building blocks of everything in the known universe, and all known interactions can be categorized into four fundamental types of interactions (the gravitational interaction, the electromagnetic interaction, the strong interaction, and the weak interaction). The Standard Model of particle physics is currently the best understanding of how these elementary particles and three of the fundamental interactions (electromagnetic, strong, and weak) are related to each other [1–3]. In this section, some basic concepts of the Standard Model will be presented. A comprehensive review can be found in Ref. [4].

Figure 1.1 shows the elementary particles in the Standard Model. All particles can be categorized into two types: fermions (particles with half-integer spin) and bosons (particles with integer spin). All six types of quarks and six types of leptons are fermions and can be further grouped into three generations, each including two types of quarks and two types of leptons. The gluon is the force carrier of the strong interaction, the photon is the force carrier of the electromagnetic interaction, and the W and Z bosons are the force carriers of the weak interaction. The Higgs boson,

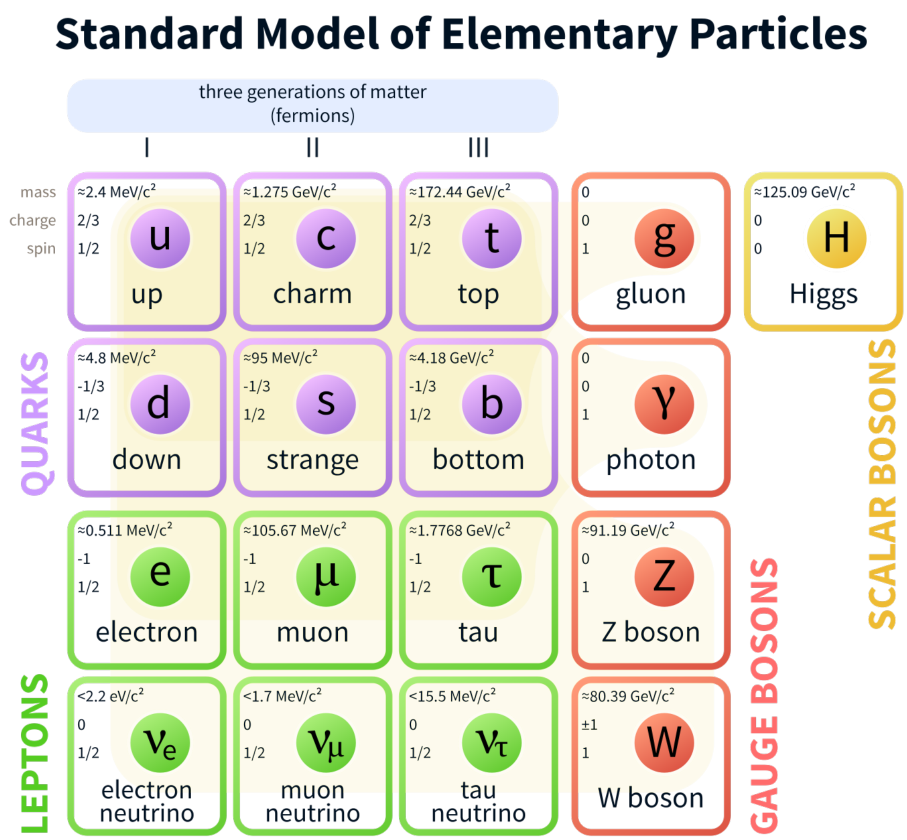

Figure 1.1.: The current elementary particles in Standard Model (taken from Wikipedia [5]).

which was discovered recently at the Large Hadron Collider (LHC) [6, 7], explains how most elementary particles acquire their mass [8].

Table 1.1 shows the fundamental interactions and some of their properties. Detailed discussion about the fundamental interactions can be found below.

The gravitational interaction acts on all particles having mass and is a long-range force. It is responsible for large-scale phenomena such as the falling apples, the motion of the Earth around the Sun, and the expansion of the universe, because these big bodies mostly contain zero net electric charges and the scale is out of the interaction ranges of weak and strong interactions. Unlike the other three interactions, the force

Table 1.1.: The fundamental interactions and some of their properties. The relative strength values are taken from Ref. [9] and reflect the relative magnitudes of the various forces as they act on a pair of protons in an atomic nucleus.

	Force carrier	Range (m)	Relative strength
Gravitational	Not yet observed	∞	1
Electromagnetic	Photon	∞	10^{35}
Weak	$W^{\pm}$, Z^0	10^{-18}	10^{24}
Strong	Gluon	10^{-15}	10^{37}

carrier of gravitational interaction has not been discovered and the Standard Model cannot describe it.

The electromagnetic interaction occurs between electrically charged particles and is a long-range force. It describes most of the phenomena of everyday experience such as friction, rainbows, lightning and all the electric devices, such as computers, microwave oven, television and computers. It is also the reason that the electrons are bounded around nuclei to form atoms.

The weak interaction is a short-range interaction, on the order of 10^{-18} m and affects all the quarks and leptons. It is the reason behaind certain nuclear phenomena such as the β decay. It is the only interaction which can change the type (or flavor) of quarks and leptons. The heavier quarks rapidly change into up and down quarks through weak interaction and that is why up and down quarks are most common in the universe. Unlike the other three interactions, the weak interaction does not act as bounding force for any objects.

The strong interaction occurs among partons (quarks and gluons) and is a short-range interaction, on the order of 10^{-15} m. It is the reason why the positive charged protons along with neutrons can be bound together in the atomic nucleus, and the quarks can be bound together to form hadrons, such as protons and neutrons. The strong interaction is described by Quantum Chromodynamics (QCD) [10, 11] in the Standard Model. In QCD, gluons interact with quarks and other gluons via the so-called color charge. The relation between color charge and strong interaction is analogous to that between electric charge and electromagnetic interaction, but the color charge comes in three types (red, green, and blue). There are two main properties in QCD: color confinement and asymptotic freedom. Color confinement is the phenomenon that observable particles are all color neutral, and color charged particles such as individual quark or gluon cannot be isolated [12]. As the energy scale increases or the distance between color charges decreases, the strong interaction between color charges decreases and this is called asymptotic freedom [11, 13, 14].

1.2 Quark Gluon Plasma

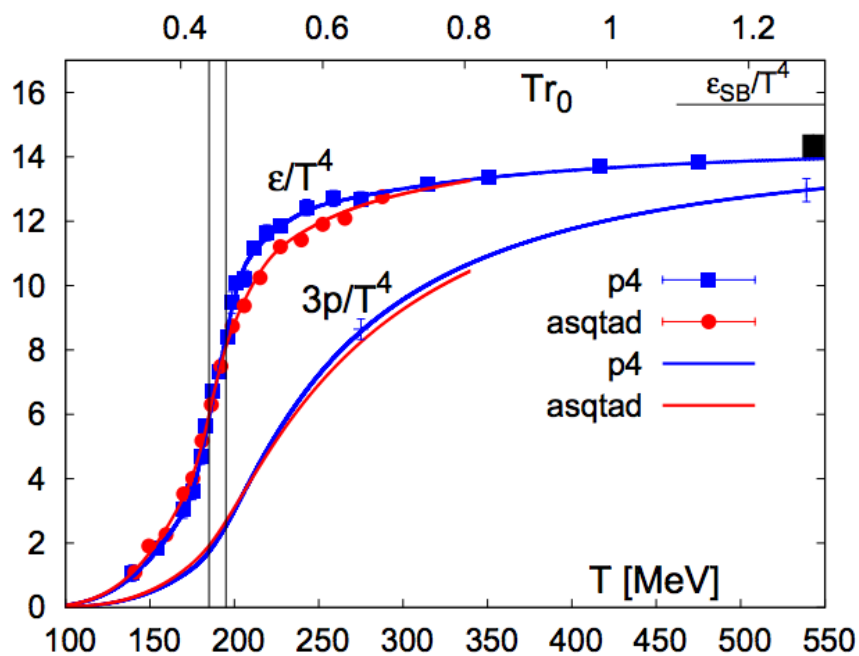

Figure 1.2.: Lattice QCD calculation of the energy density and pressure normalized by T^4 vs temperature T of equilibrant quark-gluon matter. Figure taken from Ref. [15].

Lattice QCD calculations predict a color-deconfined state of quarks and gluons, which is defined as the Quark Gluon Plasma (QGP) [15–19]. Figure 1.2 shows the lattice QCD calculation of the energy density and pressure normalized by T^4 vs temperature T [15]. A rapid rise in the energy density of matter around a critical temperature of $T_c \sim 185 - 195$ MeV corresponds to a transition to a state with deconfined quarks and gluons, the QGP. The formation of the QGP has been observed in experiments performed at the Relativistic Heavy Ion Collider (RHIC) [20–23] and at the LHC [24, 25].

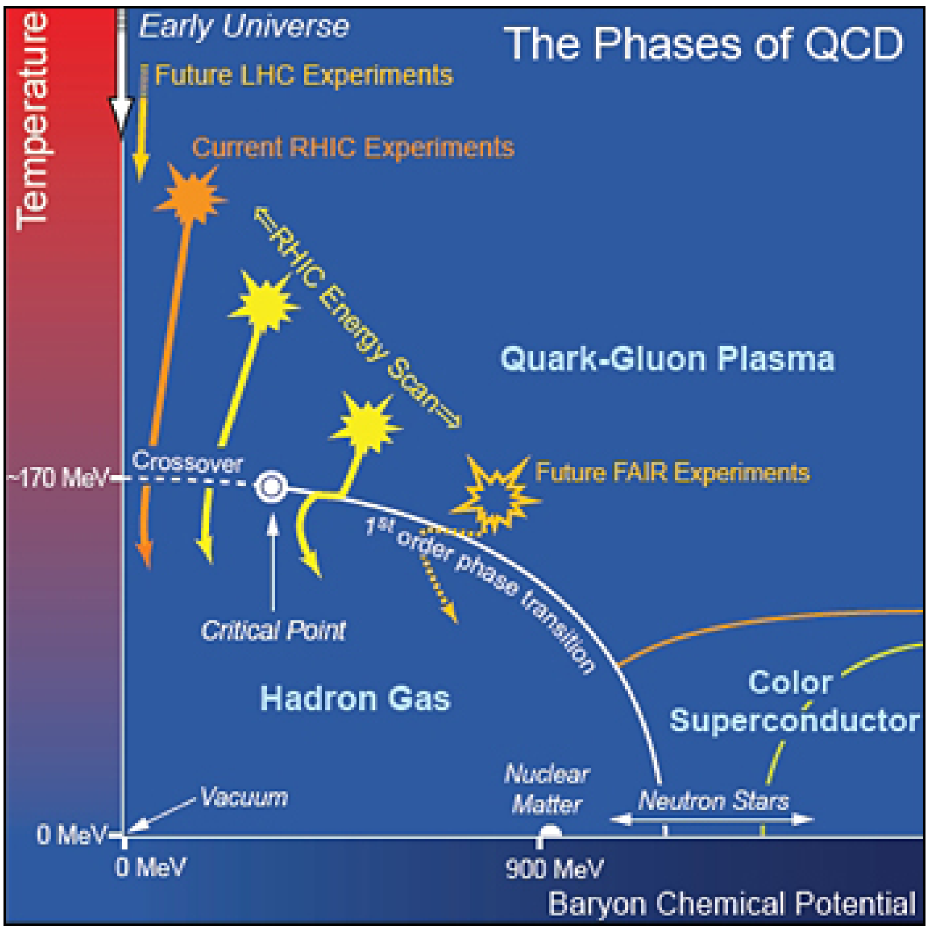

Figure 1.3.: An illustration of the QCD phase diagram from Ref. [26].

Figure 1.3 shows an illustration of the QCD phase diagram from Ref. [26]. There are three major states for the QCD system: hadron gas, the QGP state, and the color superconductor. Because of color confinement, the quarks and gluons are defined in hadrons in normal environment, lying near the bottom right at cold temperatures and high baryon chemical potentials in Fig. 1.3. With an increase of temperature and/or density, the deconfinement of quarks and gluons occurs as a consequence of the asymptotic freedom and results in the formation of the QGP. The universe is also predicted to have been in the QGP state for a few milliseconds after the Big Bang. Another interesting state is the color superconductor in the large baryon chemical potential region at low temperature. In this region, as the normal electric charges behave to form superconductor, the quarks and gluons can form cooper pairs and stop from being scattered by the lattice.

1.3 Heavy Ion Collisions

Ultra-relativistic heavy ion collisions (referred as heavy ion collisions for short in later discussion) in the top left of Fig. 1.3 are used to create the QGP experimentally. In heavy ion collisions, the nuclei are accelerated close to the speed of light ($> 0.999c$) and thus are Lorentz contracted. When two nuclei collide with each other, the energy carried by the nuclei will be released in a small volume and a short time, and then the condition of high energy density and temperature can be fulfilled. The primary goal of heavy ion physics is to study the properties of the QGP, such as temperature, the equation of state, and the transport properties, in order to provide essential insights into the QCD and the early evolution of the universe.

In this section, the centrality of heavy ion collisions is first introduced, and then two key signatures of the QGP created in heavy ion collisions, parton energy loss and collective flow, will be discussed.

1.3.1 Centrality

The size of the proton is negligible in proton-proton collisions and the collision area can be taken as one point. However, for nucleus-nucleus (AA) collisions, such

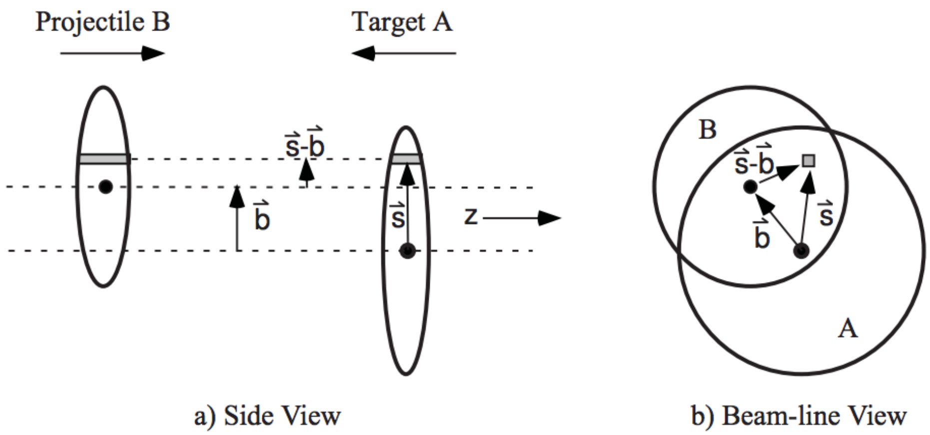

Figure 1.4.: Schematic view of a nucleus-nucleus collision in the longitudinal (left) and transverse (right) plane. Figure taken from Ref. [27].

as Lead-Lead (PbPb) nucleus collisions, the size of the nuclei cannot be ignored. Figure 1.4 shows a schematic view of a nucleus-nucleus collision, where the impact parameter b, the distance between the centers of the two colliding nuclei, is marked. One important concept is the centrality, which is used to evaluate the degree of the overlap of the two colliding nuclei. The centrality ranges 0–100%, where the centrality class of 0–10% corresponds to the 10% of collisions with the largest overlap of the two nuclei. Clearly, there is a direct relation between centrality and b. One PbPb collision can include a few to almost two thousand binary nucleon-necleon collisions depending on the centrality. However, the collision geometry cannot be measured directly experimentally and only final-state observables are available. Fortunately, there is a direct correlation between the degree of the overlap of the collision and certain final-state observables, such as the number of final-state particles produced transerse to the beam direction, and the total energy deposited in very forward detectors. In the CMS experiment, the centrality is determined by the total energy deposited in both sides of the hadronic forward calorimeters (HF) discussed in Chapter 2, at pseudorapidities of $3 < \eta < 5$. The distribution of the total energy deposited of a large minimum bias collisions is measured, and is used to devide the data sample into centrality classes, for example the top 10% most energy deposited corresponds to centrality class 0–10%. Figure 1.5 shows the distribution measured for PbPb collisions at 2.76 TeV [28]. The centrality can also be determined with other final-state observables, but the basic principle is the same.

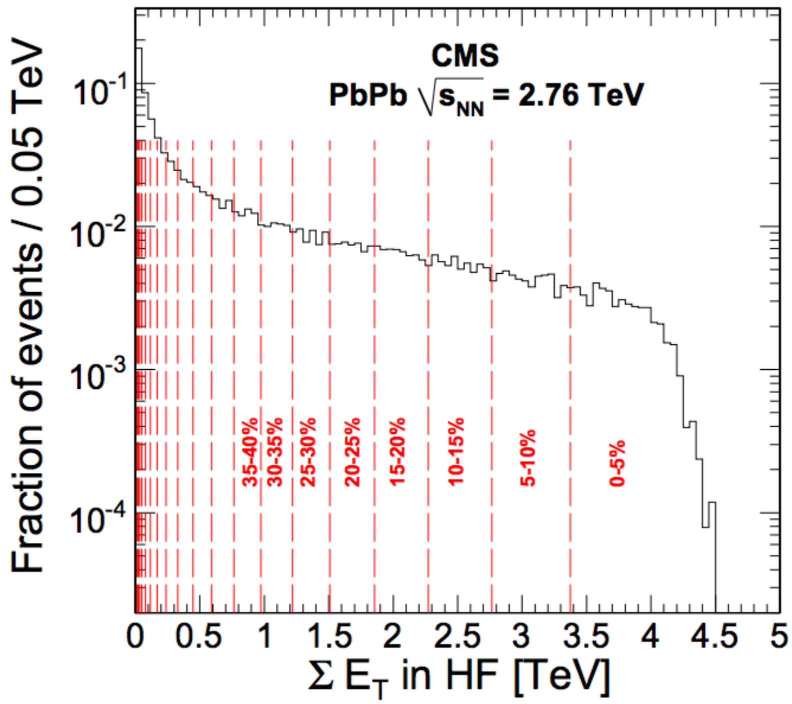

Figure 1.5.: Distribution of the total transverse energy in the HF used to determine the centrality of the PbPb collisions at 2.76 TeV. The centrality boundaries for each 5% centrality interval are shown. Figure taken from Ref. [28].

The geometric quantities of heavy ion collisions can be calculated using the Glauber model [27], where heavy ion collisions are described as a superposition of independent nucleon-nucleon collisions. The position of each nucleon in a nucleus is determined according to the Woods-Saxon distribution [29]. For the collisions between two nuclei A and B, the hard scattering cross section (σ_{AB}^{hard}), the nuclear overlap function (T_{AB}), the number of participant nucleons (N_{part}), the number of binary nucleon-

nucleon collisions (N_{coll}), and their relations can all be calculated (for more details see Ref. [27]).

1.3.2 Signature of the QGP

The QGP state produced in heavy ion collisions can just exist for a short time of a few fm/c and cannot be directly observed. The properties of the QGP must be inferred from the final-state observables. This section will introduce two important signatures of the QGP: parton energy loss and collective flow.

Parton Energy Loss

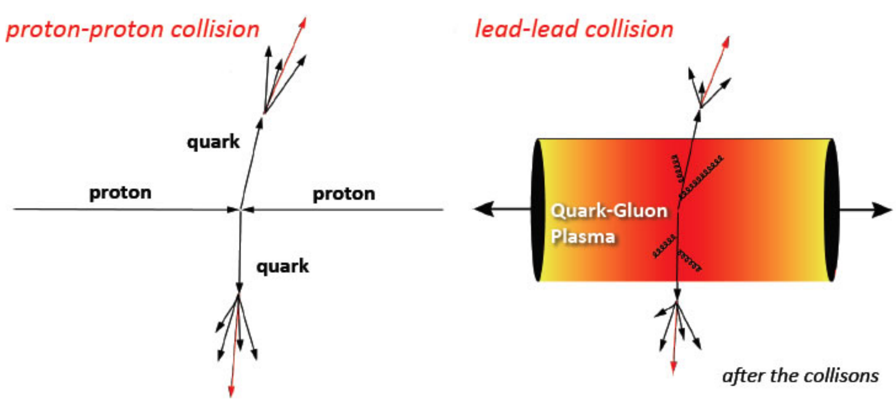

Figure 1.6.: Cartoon of a hard scattering in pp (left) and PbPb (right) collisions. Figure taken from Ref. [30].

Figure 1.6 depicts the hard scatterings in pp and AA collisions [30]. Hard scatterings between two partons can create two or more partons with high transverse momentum (p_{T}). In PbPb collisions, where the QGP is produced, the out-going partons can lose significant amount of energy as they traverse the medium, primarily through gluon radiation [31–33] and collisional energy loss [34, 35]. The spectra of produced hadrons will shift toward lower p_{T} region in AA collisions compared to pp collisions and hence appear suppressed at high p_{T}.

One observable to quantify the parton energy loss is the nuclear modification factor (R_{AA}) defined as the ratio of the yield in AA collision to that in pp collision scaled by the number of binary nucleon-nucleon collisions N_{coll}:

$$R_{\mathrm{AA}} = \frac{1}{N_{coll}} \frac{dN_{PbPb}}{dp_{\mathrm{T}}} \Big/ \frac{dN_{pp}}{dp_{\mathrm{T}}} = \frac{1}{T_{\mathrm{AA}}} \frac{dN_{PbPb}}{dp_{\mathrm{T}}} \Big/ \frac{d\sigma_{pp}}{dp_{\mathrm{T}}} \ . \tag{1.1}$$

The R_{AA} can be measured differentially in p_{T} or η, for a specific centrality class, or for a specific particle specie. $R_{\mathrm{AA}} = 1$ means that the production is not modified relative to pp collisions. When $R_{\mathrm{AA}} < 1$, the production is suppressed, which is the general expectation for hadrons with high p_{T} as a consequence of the in-medium parton energy loss. For $R_{\mathrm{AA}} > 1$, the production is enhanced. Apart from parton energy loss, initial-state effects [36–38] could also affect the production of particles in heavy ion collisions. To quantify the impact from the initial-state effects, studies have been performed in proton-nucleus (pA) collisions [39–42], and it is found that the initial-state effects don't account for the suppression of high-p_{T} particles in AA collisions. The R_{AA} of high-p_{T} particles is one of the key signatures of the QGP formation, and has been widely measured at RHIC [20–23] and LHC [24, 25] to study the properties of the QGP produced in heavy ion collisions Figure 1.7 shows the R_{AA} of charged particles in PbPb collisions at a center-of-mass energy $\sqrt{s_{\mathrm{NN}}} = 5.02\mathrm{TeV}$ per nucleon pair as a function of p_{T} for six centrality classes measured with the CMS detector [43]. Clearly, the production of charged particles is suppressed in PbPb collisions, and the supression has strong p_{T} and centrality dependence.

Azimuthal Anisotropy

The collective motion of the emitted particles is an important signature of the QGP produced in heavy ion collisions, and suggests that the QGP is strongly coupled [45, 46]. In this thesis, we will focus on the azimuthal anisotropy, which is an important type of the collective motion. In noncentral collisions, the reaction plane

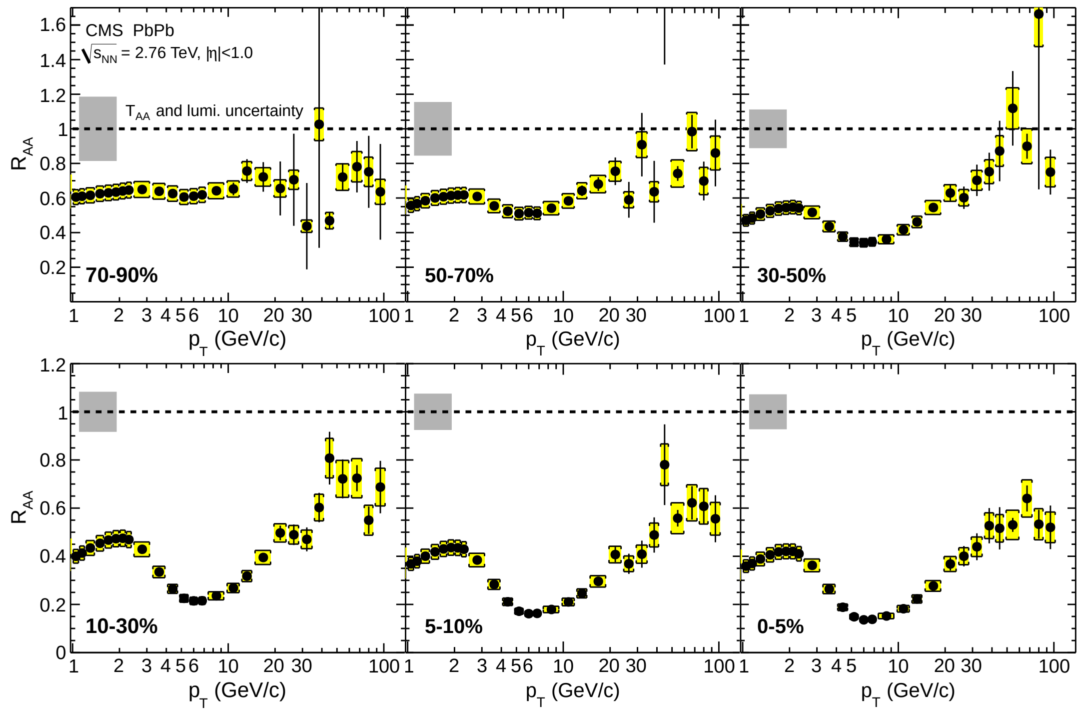

Figure 1.7.: The R_{AA} of charged particles in PbPb collisions at $\sqrt{s_{\mathrm{NN}}} = 2.76$ TeV as a function of p_{T} for six centrality classes measured with the CMS detector [43].

for each event is defined as the plane formed by the beam direction and the impact parameter vector. As shown in Fig. 1.8, the overlap region of the two nuclei is spatially asymmetric like an almond shape if the nucleon density is continuous. However, in reality, the overlap region has a more irregular shape because the nucleon density is not continuous as showed in Fig. 1.9. The azimuthal anisotropy can be quantified by the Fourier coefficients v_n in the azimuthal angle distribution of the hadron yield:

$$E\frac{d^3N}{d^3p} = \frac{1}{2\pi}\frac{d^2N}{p_T dp_T dy}\left(1 + \sum_{n=1}^{\infty} 2v_n \cos\left[n\left(\phi - \Psi_n\right)\right]\right), \tag{1.2}$$

where ϕ, E, y and p_{T} are the particle's azimuthal angle, energy, rapidity, and transverse momentum, respectively. Here, Ψ_n is the participant plane angle corresponding to the nth harmonic, defined as the azimuthal angle of the direction of the maximum particle density corresponding to the nth harmonic in the transverse plane [47]. The

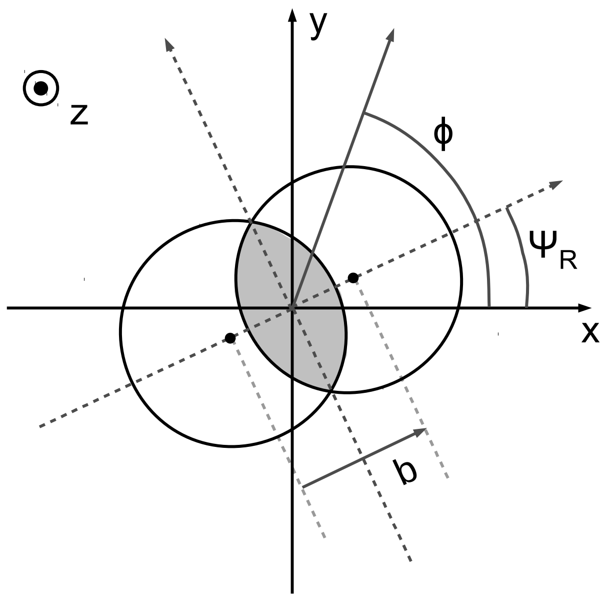

Figure 1.8.: A schematic diagram of a noncentral AA collision viewed in the transerse plane, indicating the azimuthal angle ϕ, the impact parameter b, and the reaction plane Ψ_R. Figure taken from Ref. [44].

v_2 and v_3 coefficients are commonly called elliptic flow and triangular flow, respectively. Figure 1.9 shows the decomposition of one initial condition into its first 4 harmonic deformations.

The azimuthal anisotropy originates from the initial geometry of the overlap region of the two colliding nuclei. Generally, two mechanisms account for the azimuthal anisotropy: at low and intermediate p_{T} (p_{T} lower than 5–8 GeV/c), the azimuthal anisotropy is from the collective expansion of the medium through the interactions among the medium constituents; at high p_{T}, the path length dependence of parton energy loss can give rise to positive azimuthal anisotropy [48, 49].

However, neither the reaction plane or the participant planes can be measured directly experimentally. There are several experimental methods developed to eval-

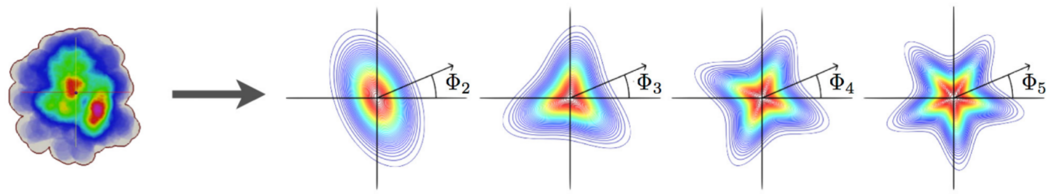

Figure 1.9.: Decomposition of one initial condition into its first 4 harmonic deformations. Here, ϕ_n stands for the participant plane angle for the nth harmonic. Figure taken from Ref. [50].

uate the anisotropic flow based on the final-state particle distributions. One of the method is to reconstruct the event plane for each event. With the final state particles, the event plane can be built experimentally with the beam direction and the direction of the maximal flow determined from the azimuthal distributions of the final-state particles. Under reasonable assumptions, the event plane is expected to coincide with the participant plane [51]. The theoretical calculations also confirm that there is a strong event by event correlation between the the event plane and the participant plane [52–55]. More details about the event plane reconstruction with the CMS detector used in this thesis can be found in Refs. [44, 56].

Figure 1.10 shows the measured v_2 utilizing event plane as a function of p_{T} for different centrality classes [44] in PbPb collisions at 2.76 TeV. Significant v_2 values are observed, and the v_2 values have strong dependence on p_{T} and centrality.

1.4 Open Heavy Flavor Study in Heavy Ion Collisions

Heavy quarks (charm and bottom) are effective probes to study the properties of the QGP medium produced in heavy ion collisions. They are primarily produced via initial hard scatterings in heavy ion collisions because of their large mass, and thus carry information about the early stages of the QGP [57, 58]. Therefore, heavy quarks are cleaner probes to study the QGP than light quarks and gluons, which may be produced in different stages of the heavy ion collisions.

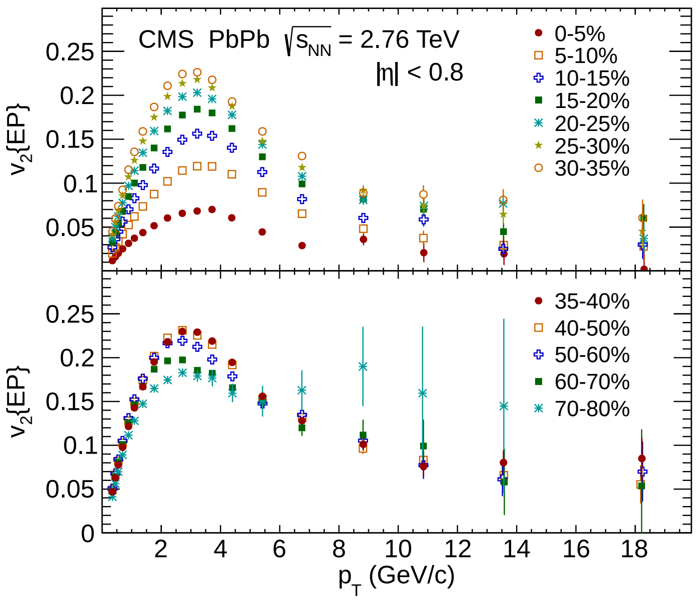

Figure 1.10.: The measured v_2 utilizing event plane as a function of p_{T} for different centrality classes in PbPb collisions at 2.76 TeV. Figure taken from Ref. [44].

As the high-p_{T} light partons, heavy quarks can lose energy via radiative and collisional interactions with the medium constituents when they traverse through the medium. Because the effective color charge of quarks is smaller than that of gluons, quarks are expected to lose less energy than gluons. Besides, the small-angle gluon radiation is expected to be smaller for heavy quarks than for light quarks and gluons, which is defined as the dead-cone effect [59–61]. The dead-cone effect is expected to be more obvious at low p_{T}, where the quark mass is not negligible. Thus, a hierarchy in the *average* radiative energy loss of gluons and quarks is expected at low p_{T}:

$$\langle \Delta E_{\mathrm{gluon}} \rangle > \langle \Delta E_{\mathrm{light}} \rangle > \langle \Delta E_{\mathrm{charm}} \rangle > \langle \Delta E_{\mathrm{bottom}} \rangle. \tag{1.3}$$

This energy loss hierarchy may be transferred to the R_{AA}, but many other factors may affect the R_{AA} hierarchy of the gluons, light quarks and heavy quarks, such as the difference in the p_{T} shapes of light hadrons and heavy flavor hadrons, and also collisional energy loss [62, 63]. Therefore, to get reliable predictions for the R_{AA} hierarchy, one has to rely on theoretical calculations taking all factors into account.

There is no collective motion associated with heavy quarks when they are produced. However, they can acquire collective flow through their interactions with the medium constituents. Therefore, the measurement of azimuthal anisotropy of the final-state heavy flavor hadrons can provide essential insights into the interactions between the heavy quarks and the medium and properties of the QGP. At low and intermediate p_{T}, the heavy flavor hadron v_n coefficients are a good measure of the interaction strength between the heavy quarks and the medium. Comparing the v_n values of heavy flavor and light hadrons can quantify the extent to which heavy quarks flow with the medium. Besides, the measurement can help explore the coalescence mechanism for heavy flavor hadron production, where heavy quarks recombine with light quarks from the medium. The coalescence mechanism can lead to positive v_n of heavy flavor hadrons even if the heavy quarks don't flow with the medium [64, 65]. At high p_{T}, the heavy flavor hadron v_n coefficients can help constrain the path length dependence of heavy quark energy loss [48, 49], providing complementing information to the measurement of R_{AA}.

In this thesis, the analyses on prompt D^0 meson (including both the D^0 and $\overline{D}^0$ states) nuclear modification factor [66,67] and azimuthal anisotropy [68] in PbPb collisions with the CMS detector will be presented. The production of D^0 mesons is found to be strongly suppressed in PbPb collisions, and significant azimuthal anisotropy coefficients v_2 and v_3 of D^0 mesons are observed. Apart from these CMS measurements, similar measurements of D mesons are also performed with the STAR detector [69,70] and the ALICE dector [71–74]. Besides, the R_{pA} of D mesons from ALICE is consistent with unity within uncertainties and no clear initial-state effects are observed [75]. Thus, the suppression of D^0 meson in PbPb collisions cannot be explained by initial-state effects, and is due to the interactions between charm quarks and the QGP medium.

2. The CMS Detector

The work in this thesis is performed using the data collected by the Compact Muon Solenoid (CMS) detector. The CMS detector is a general-purpose detector at the CERN Large Hadron Collider (LHC), which covers broad physics programs, such as the search for and study of the Higgs boson, the exploration of physics beyond the Standard Model, and also heavy ion physics.

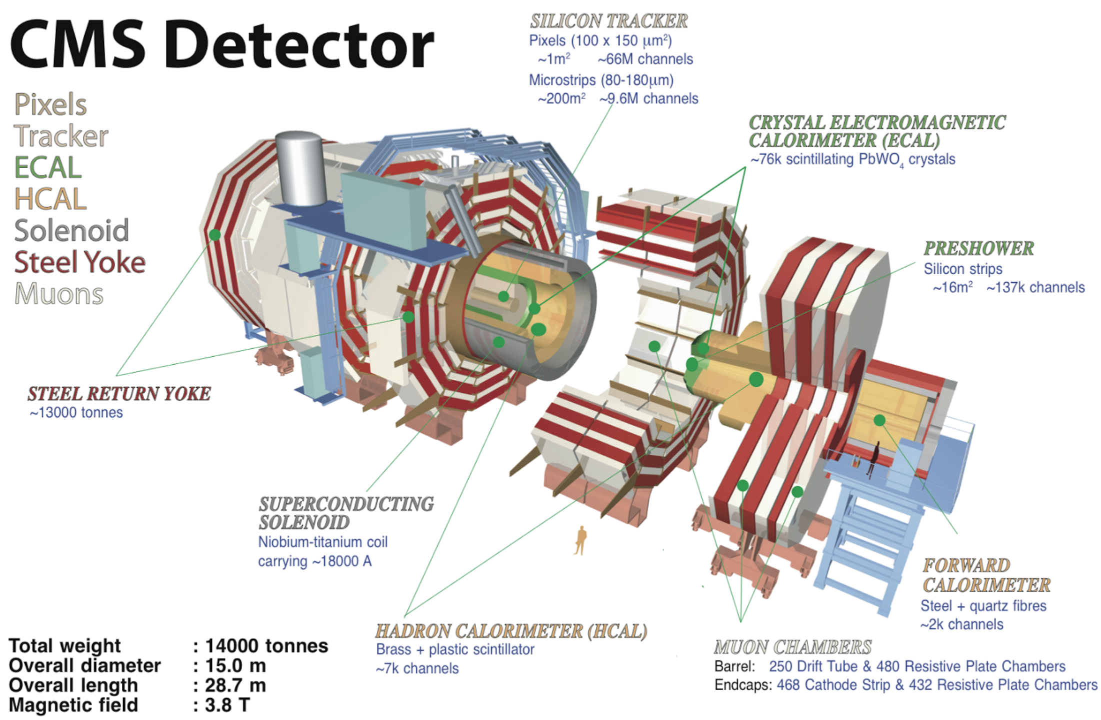

Figure 2.1.: A schematic representation of the CMS detector with its various subsystems in retracted positions (CERN).

Figure 2.1 shows a schematic representation of the CMS detector with its various subsystems in retracted positions. The CMS detector is built around a 13-m long superconducting solenoid magnet with an inner diameter of 6 m, which can generate a magnetic field of 4 Tesla (about 100,000 times the magnetic field of the Earth). The actual strength is 3.8 Tesla during data taking. The strength of the magnetic field is to fulfill the desired momentum resolution. The CMS detector is mainly comprised of the inner tracking system, the superconductiong magnet, the electromagnetic calorimeter, hadron calorimeter, the muon system, and forward detectors. This chapter presents certain details of the detector subsystems relevant to the analyses in this thesis. A complete description of the CMS detector can be found in Ref. [76].

The detector coordinate system has the origin centered at the nominal collision point inside the experiment, with the z axis pointing along the counterclockwise beam direction, the x axis pointing radially inward towards the center of the LHC ring, and the y axis pointing vertically upward.

2.1 The Inner Tracking System

The CMS inner tracking system is designed to precisely and efficiently reconstruct the trajectories of charged particles and the secondary vertices. At the LHC design luminosity, around 1000 particles were expected to be produced within the tracker acceptance from more than 20 overlapping pp collisions per bunch crossing. Fortunately, this is similar to the number of particles produced in a PbPb collision at $\sqrt{s_{\mathrm{NN}}} = 2.76$ and 5.02 TeV. Therefore, the CMS tracker also works well for heavy ion collisions.

The CMS tracker consists of two subdetectors, the pixel tracker and the silicon strip tracker. Figure 2.2 shows a schematic view of the CMS tracker in the $r-z$ plane. The pixel tracker (red lines in Fig. 2.2) resides closest to the beampipe, and consists of three concentric cylindrical barrel layers at midpseudorapidity at a distance of 4.4, 7.3, and 10.2 cm from the nominal collision point, and two disc-shaped endcap layers

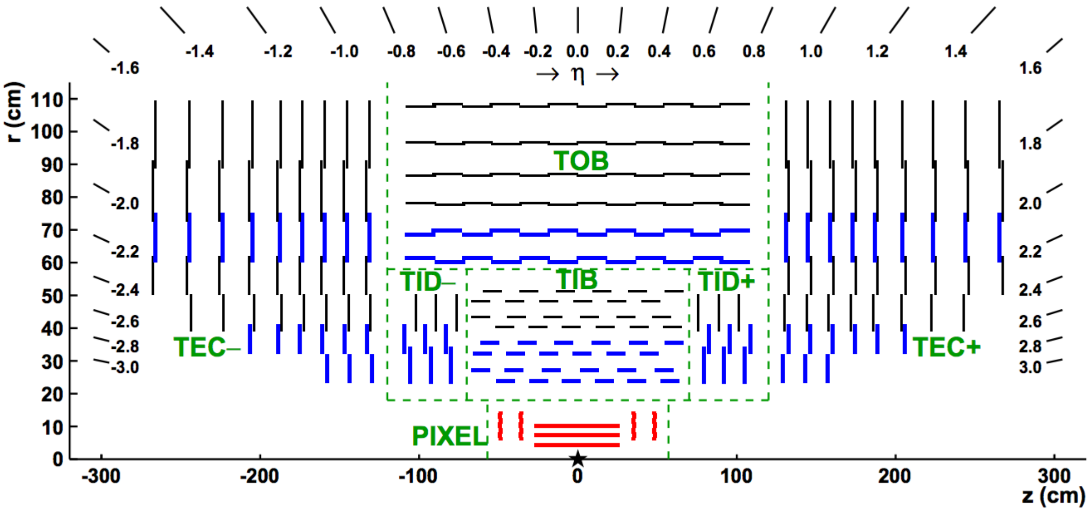

Figure 2.2.: Schematic view of the CMS tracker in the $r - z$ plane. The tracker is symmetric about the horizontal line $r = 0$, so only top half is shown in the Figure. The star, at the center of the tracker, stands for the nominal collision point. The green dashed lines divided the tracker into different parts. Figure taken from Ref. [77].

at forward and backward pseudorapidity. The silicon strip tracker (black and blue lines in Fig. 2.2) is comprised of 10 barrel layers (TIB and TOB) at midpseudorapidity extending outwards to a radius of 110 cm, and 3 smaller disc layers (TID) and 9 larger disc layers (TEC) at forward pseudorapidity. The data used in this thesis was taken before the pixel upgrade in the end of 2016, so the description here is for the pixel tracker before the upgrade. Details of the pixel tracker upgrade can be found in Ref. [78].

The inner tracker system is essential for the reconstruction of D^0 discussed in this thesis. The decay length of D^0 is 122.9 μm, so the flight distance is on similar order at low p_{T} and can be on the order of 1 mm or even higher at high p_{T}. As mentioned in Chapter 3, the reconstruction of the secondary vertex using the two daughter tracks is a prerequisite for candidate selection in D^0 reconstruction. The quality of the secondary vertex reconstruction is determined by the reconstruction performance of particle trajectories, especially the accuracy of the position informa-

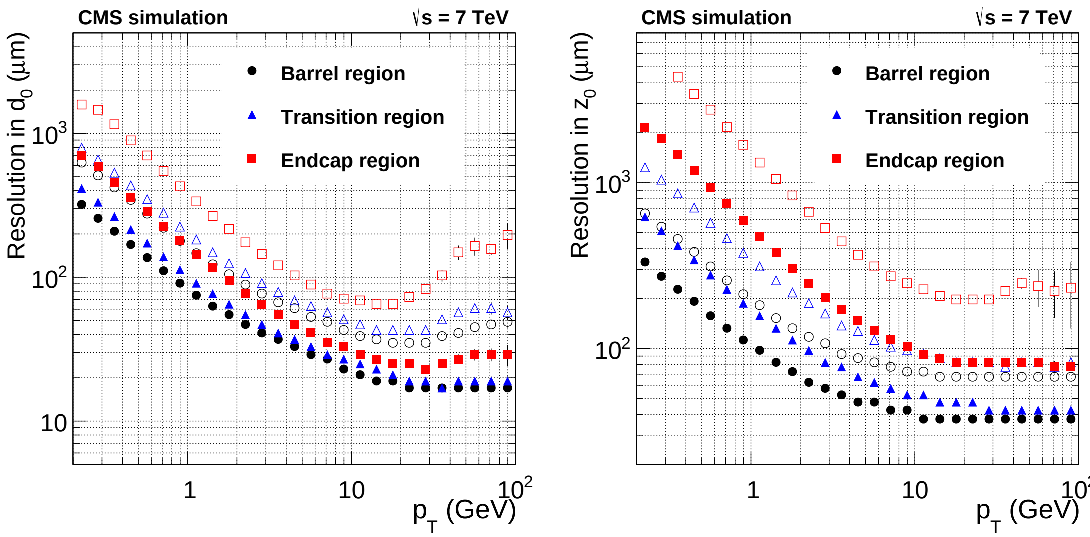

Figure 2.3.: High-purity track transverse (left) and longitudinal (right) impact parameter resolution as a function of p_{T} for the CMS detector. The solid (open) symbols correspond to the half-width at 68% (90%) confidence level. Figures taken from Ref. [77].

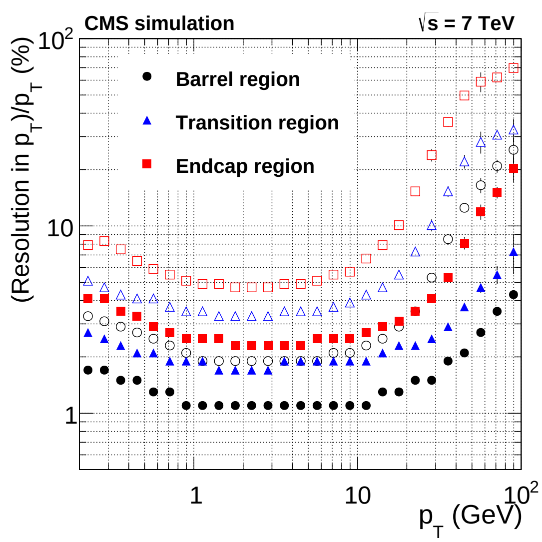

Figure 2.4.: High-purity track p_{T} resolution as a function of p_{T} for the CMS detector. The solid (open) symbols correspond to the half-width at 68% (90%) confidence level. Figures taken from Ref. [77].

tion. The accuracy of the position information can be described by the resolution of track impact parameter. The impact parameter is defined as the minimal distance between the track helix and the primary vertex. Figure 2.3 shows the high-purity track transverse (left) and longitudinal (right) impact parameter resolution as a function of p_{T}. Another important property is the track p_{T} resolution shown in Fig. 2.4. Benefitting from the 3.8-Tesla magnetic field, the p_{T} resolution is typically 1–2% for tracks of $1 < p_{\mathrm{T}} < 10$GeV and $|\eta| < 1.5$. The impact parameter and p_{T} resolutions in the Barrel region are better than those in the Endcap region, which is the reason that only tracks within $|\eta| < 1.5$ are used in D^0 reconstruction. Additional details of the performance of the CMS tracking system can be found in Ref. [77].

2.2 Hadron Foward Calorimeter

The hadron foward calorimeter (HF) is of particular importance to heavy ion collisions because the centrality can be determined with the HF detector, as discussed in Section 1.3.1, and the event plane can be reconstructed with the HF detector, as discussed in Refs. [44, 56].

The HF calorimeter provide azimuthal coverage in the pseudorapidity range $3.0 < |\eta| < 5.2$ and is required to withstand extremely high particle flux. The two halves of the HF calorimeter are located 11.2 m from the interaction region, one on each end. Left panel of Figure 2.5 shows the location of the HF detector on one end. For each pp collision, 760 GeV of total energy will be deposited into the HF on average, while only 100 GeV for all subdetectors within $|\eta| < 3.0$. The HF calorimeter uses 5 mm thick grooved steel as an absorber, with grooves approximately 1 mm wide and deep. Quartz fibers are used as the sensitive material and inserted into the grooves. Each HF calorimeter is comprised of 432 readout towers, containing long and short quartz fibers running parallel to the beam. The short fibers start at a depth of 22 cm from the front of the detector, while the long fibers run the entire depth of the HF calorimeter (165 cm). By reading out the two sets of fibers separately, the showers generated by

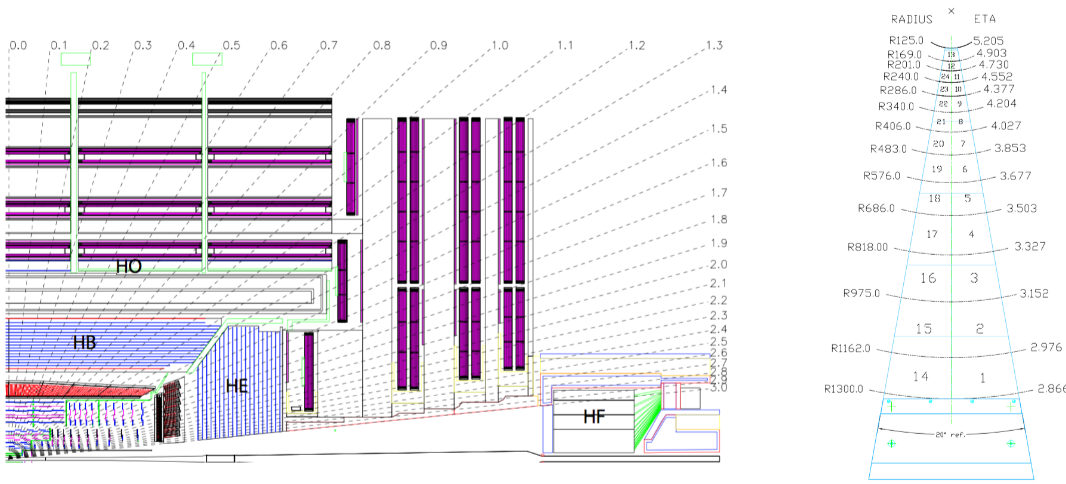

Figure 2.5.: (left) Longitudinal view of the CMS detector showing the locations of the hadron forward (HF) calorimeter and other hadron calorimeters. (right) Transverse segmentation of a single 20° modular edge of the HF detector. Figures taken from Ref. [76].

electrons and photons, which deposit a large fraction of their energy in the long-fiber calorimeter segment, can be distinguished from the showers generated by hadrons, which produce on average nearly equal signals in both calorimeter segments.

The HF calorimeter forms a hollow cylinder with an inner radius of 12.5 cm from the center of the beam line, and an outer radius of 130.0 cm. Azimuthally, each HF calorimeter consists of 18 modular wedges covering 20°. A diagram of the HF segmentation in the transverse plane is showed in the right panel of Fig. 2.5.

2.3 The Level-1 and High Level Trigger System

The collision rates of proton-proton and heavy ion collisions which the LHC provides can be on the order of 10 MHz or even higher. Recording all the collision events to disk will be prohibitively expensive, and processing all these events for analysis will take huge amount of computational resources. Therefore, the task of the trigger system at CMS is to reduce the rate of recording under 1 kHz by keeping the interesting events for analyses and filtering out the uninteresting events. Therefore, the trigger system is an essential part at CMS and determines the data quality of analyses. A two-level trigger system, comprised of Level-1 (L1) Trigger [79] and High-Level Trigger (HLT) [80], is used at CMS. The L1 triggers are hardware-based, while the HLT triggers are software-based.

The L1 triggers consist of custom-built programmable electronics, which are largely integrated with the readout systems of subdetectors. The L1 triggers are designed to reduce the rate under 100 kHz. Within 4 μs, the system must decide whether to drop an event or pass it to the HLT triggers. The L1 triggers are typically implemented using simple threshold algorithms written to field-programmable gate arrays (FPGAs), which allow for a fully customizable hardware circuit.

The HLT triggers select events in a similar way to that used in the offline processing, which can be time consuming. The large reduction factor of the L1 triggers allows much more processing time for the HLT triggers. For each event, objects such as tracks, muons, and jets can be reconstructed and selection criteria can be applied to select the events which may be interesting for offline data analysis. For example, the D^0 meson triggers discussed in Section 4.2.2 involve track reconstruction and D^0 candidate reconstruction. However, the offline reconstruction is usually too time consuming to perform at HLT especially for heavy ion collisons. Therefore, the HLT triggers usually use reconstruction simplied from the offline reconstruction. This can lead to differences in the HLT and offline reconstruction performances, such as efficiencies and resolutions, and further lead to some loss in trigger efficiency, which is the reason that the D^0 meson trigger efficiencies in PbPb collisions are around 90–95%.

One important concept for the trigger system is the prescale factor, which means only fraction of data from a specific L1 or HLT trigger will be further processed by a running counter or random selection. If the output rate of a specific L1 trigger is too high for HLT processing, applying a prescale factor of 3 to this L1 trigger means only 1/3 of events passing this L1 trigger will be passed to the HLT triggers.

2.4 The CMS Computing Model

It is difficult to fulfill the CMS computing and storage requirements at one single place for both technical and funding reasons. Therefore, a distributed system of computing services and resources, which is a global network of tiered computing facilities, has been constructed as the CMS computing environment. Figure 2.6 shows a schematic diagram of the CMS Computing System. A detailed description of the CMS Computing System can be found in Refs. [81].

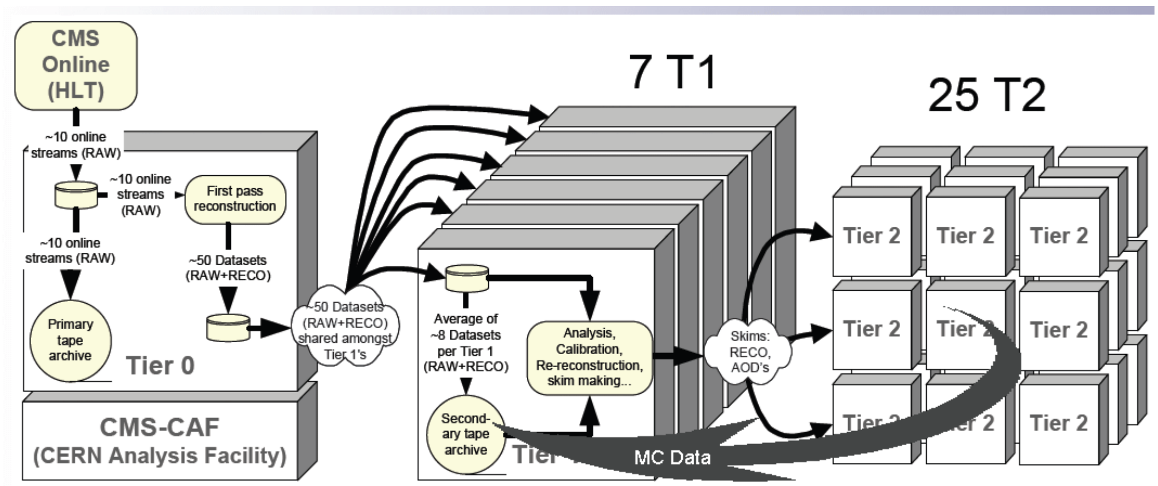

Figure 2.6.: A schematic diagram of the CMS Computing System. Figures taken from Ref. [82].

The first tier of the system, known as Tier-0, is only one site, CERN. The Tier-0 facility accepts, stores, and archives raw collision data from the trigger system, performs an initial "prompt" reconstruction of the data, and distributes raw and reconstruction data among Tier-1 facilities.

The Tier-1 facilities archives (part of) the RAW and reconstruction data (secure second copy), performs additional reconstruction over the data with improved calibrations and algorithms, distributes reconstruction data used for analyses to Tier-2 facilities, and provides secure storage and redistribution for Monte Carlo simulations produced by the Tier-2 facilities.

The Tier-2 facilities keep part of the reconstruction data for physics analyses, provide computing resources (CPU and storage) for user usage, and produce Monte Carlo simulations, which are usually transferred to the Tier-1 facility for wider distribution. The Tier-2 activities are organized by the Tier-2 responsibles in collaboration with physics groups, regional associations, and local communities.

3. D^0 Reconstruction and Signal Extraction

In this thesis, the D^0 mesons are reconstructed through the hadronic decay channel $D^0 \to K^- \pi^+$ with a branching ratio of 3.93±0.04% [83]. Figure 3.1 is the schematic view of the $D^0 \to K^- \pi^+$ decay channel and the variables marked will be defined and discussed below.

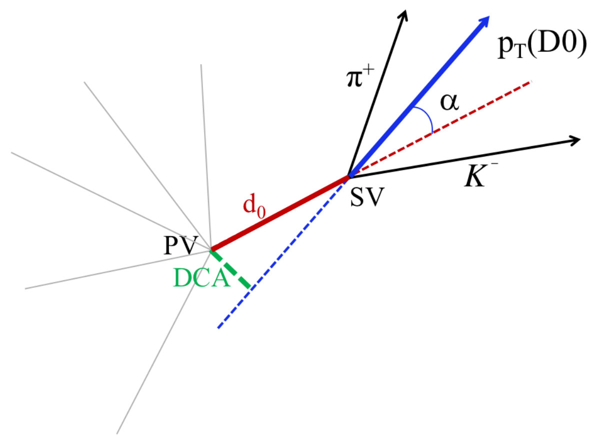

Figure 3.1.: Schematic view of the $D^0 \to K^- \pi^+$ decay channel.

3.1 Reconstruction

The D^0 candidates are formed by combining pairs of oppositely charged tracks and requiring an invariant mass within a ± 200 MeV/c^2 window of the nominal D^0 mass of 1864.83 MeV/c^2 [83]. Tracks are required to pass kinematic selections of $p_T >$ 0.7 GeV/c and $|\eta| < 1.5$, and must satisfy high-purity track quality criteria [77] to reduce the combinatorial background from misreconstructed tracks. For each pair of selected tracks, two D^0 candidates are considered. For the first candidate, the pion mass is attributed to the first track while the other track is assumed to have the kaon mass. The second candidate is defined by swapping the masses attributed to those two tracks. For each candidate, a secondary vertex is reconstructed with a kinematic vertex fit [84]. Based on properties of these two-particle secondary vertices, several selections are applied in order to further reduce the combinatorial background. In particular, the selections are applied to:

- $d_0/\sigma(d_0)$: the 3D distance between the secondary vertex and the primary vertex divided by its uncertainty
- α: the angle between total momentum vector of tracks and the vector from the primary vertex to the secondary vertex
- vertex probability: the χ^2 probability of the secondary vertex fit
- DCA: the distance of the closest approach of D^0 candidates to the primary vertex

The selections on $d_0/\sigma(d_0)$, α, and vertex probability are optimized in Section 3.2 and all applied in the measurements of D^0 meson nuclear clear modification factor analyses discussed in Chapter 4 and azimuthal anisotropy analysis discussed in Chapter 5, while the selection on DCA is only applied in the measurements of D^0 azimuthal anisotropy analysis to reduces the systematic uncertainties from nonprompt D^0 (D^0 from decays of b hadrons) contribution.

3.2 Selection Optimization

The goal of the optimization procedure is to maximize the statistical significance of the signal while keeping reasonably high signal efficiencies. The optimal cut minimizing background efficiency for aspecific signal efficiency is obtained by the TMVA (Toolkit for Multivariate Data Analysis with ROOT) [85]. Rectangular cut is chosen as the classification method in TMVA. Reconstructed candidates which can be matched to generated particles in MC are used as signal sample during training in TMVA, while the sideband of data sample is used as background sample. Sideband is defined as $0.1\ \text{GeV}/c^2 < |M_{D^0} - M_{D^0}^{PDG}| < 0.15\ \text{GeV}/c^2$. The amount of background in the signal region is estimated by a linear interpolation using the sideband. The signal-to-background ratios are p_{T} dependent, so the selections on $d_0/\sigma(d_0)$, α, and vertex probability are optimized each p_{T} bin.

The optimization is done for the measurements of D^0 meson R_{AA} in PbPb collisions at 2.76 TeV, discussed in Section 4.1, and 5.02 TeV, discussed in Section 4.2, respectively. The selections on $d_0/\sigma(d_0)$, α, and vertex probability applied in measurements of D^0 meson azimuthal anisotropy discussed in Chapter 5 are adopted from the optimized selections. The analyses actually don't require the selections to be prefectly optimized as long as the D^0 signal significance after selection is not too bad. The plots shown below are from the optimization for the measurements of D^0 meson R_{AA} in PbPb collisions at 2.76 TeV.

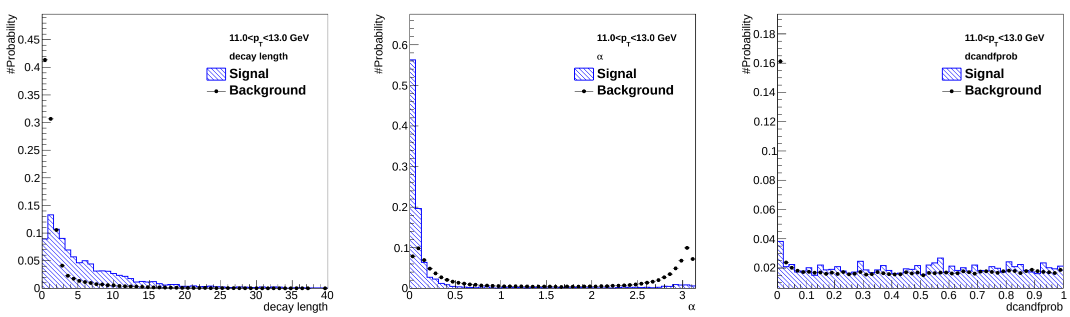

Figure 3.2.: Distributions of D^0 cut variables for background and signal candidates in the p_{T} range 11.0–13.0 GeV/c.

Figure 3.2 shows the distributions of the selection variables of signal and background candidates in the p_{T} range 11.0–13.0 GeV/c. The optimal selection values are defined as the one maximizing the statistical significance $s/\sqrt{s+b}$. Here, s is the expected number of signal yield from the FONLL calculation, multiplied by the efficiency and acceptance from MC, and b is the expected number of background in the signal region. The signal region is defined as $|M_{D^0} - M_{D^0}^{PDG}| < 2\sigma$, where σ is

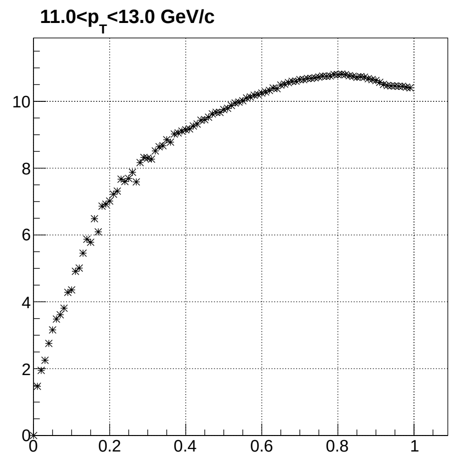

Figure 3.3.: Signal statistical significance versus signal efficiency in the p_{T} range 11.0–13.0 GeV/c.

p_{T}(GeV/c)	$d_0/\sigma(d_0)$	α	**Vertex Probability**
2.5–3.5	> 5.90	< 0.12	> 0.248
3.5–4.5	> 5.81	< 0.12	> 0.200
4.5–5.5	> 5.10	< 0.12	> 0.191
5.5–7.0	> 4.62	< 0.12	> 0.148
7.0–9.0	> 4.46	< 0.12	> 0.102
9.0–11.0	> 4.39	< 0.12	> 0.080
11.0–13.0	> 4.07	< 0.12	> 0.073
13.0–16.0	> 3.88	< 0.12	> 0.060
16.0–20.0	> 3.67	< 0.12	> 0.055
20.0–28.0	> 3.25	< 0.12	> 0.054
28.0–40.0	> 2.55	< 0.12	> 0.050

Table 3.1.: Summary table of the selection criteria in different p_{T} intervals.

the width of D candidates mass fitting in MC. Figure 3.3 presents the values of the signal significance versus the signal efficiency in the p_{T} range 11.0–13.0 GeV/c. The final selection values are reported in Table 3.1.

3.3 Signal Extraction

The raw D^0 yield in each p_{T} interval is extracted through a fit on the mass spectrum of D^0 candidates. The fit function consists of the following components:

- two Gaussian functions with same mean but different width and area to model the signal ($S(m_{inv})$).

- a third-order polynomial or an exponential function to model the combinatorial background ($B(m_{inv})$). In the D^0 R_{AA} in PbPb collisions at 2.76 TeV analysis, a exponential function is used to model the combinatorial background in default fit, while a third order polynomial is used in default fit in the D^0 R_{AA} and v_n in PbPb collisions at 5.02 TeV analyses. When one is used in default fit, the other is used in the evaluation of systematic uncertainties.

- a single Gaussian function to describe the invariant mass shape of D^0 candidates with incorrect mass assignment from the exchange of pion and kaon designation ($SW(m_{inv})$).

The width of $SW(m_{inv})$ is fixed according to MC simulations. Also, the ratio of the yields of $SW(m_{inv})$ and $S(m_{inv})$ is fixed to the value extracted in simulations.

Two Gaussian functions are used to model the signal shape based on studies in MC simulation. As showed in Figure 3.4 and 3.5, two Gaussian functions can better describe the mass spectrum of MC truth D^0 candidates compared to a single Gaussian function. The MC truth D^0 candidates stand for the candidates which can be matched to generator level D^0 signal in simulation.

As discussed previously, two D^0 candidates are formed with each pair of tracks. It is the same for the two tracks from the real D^0 signal. One of the two candidates is real

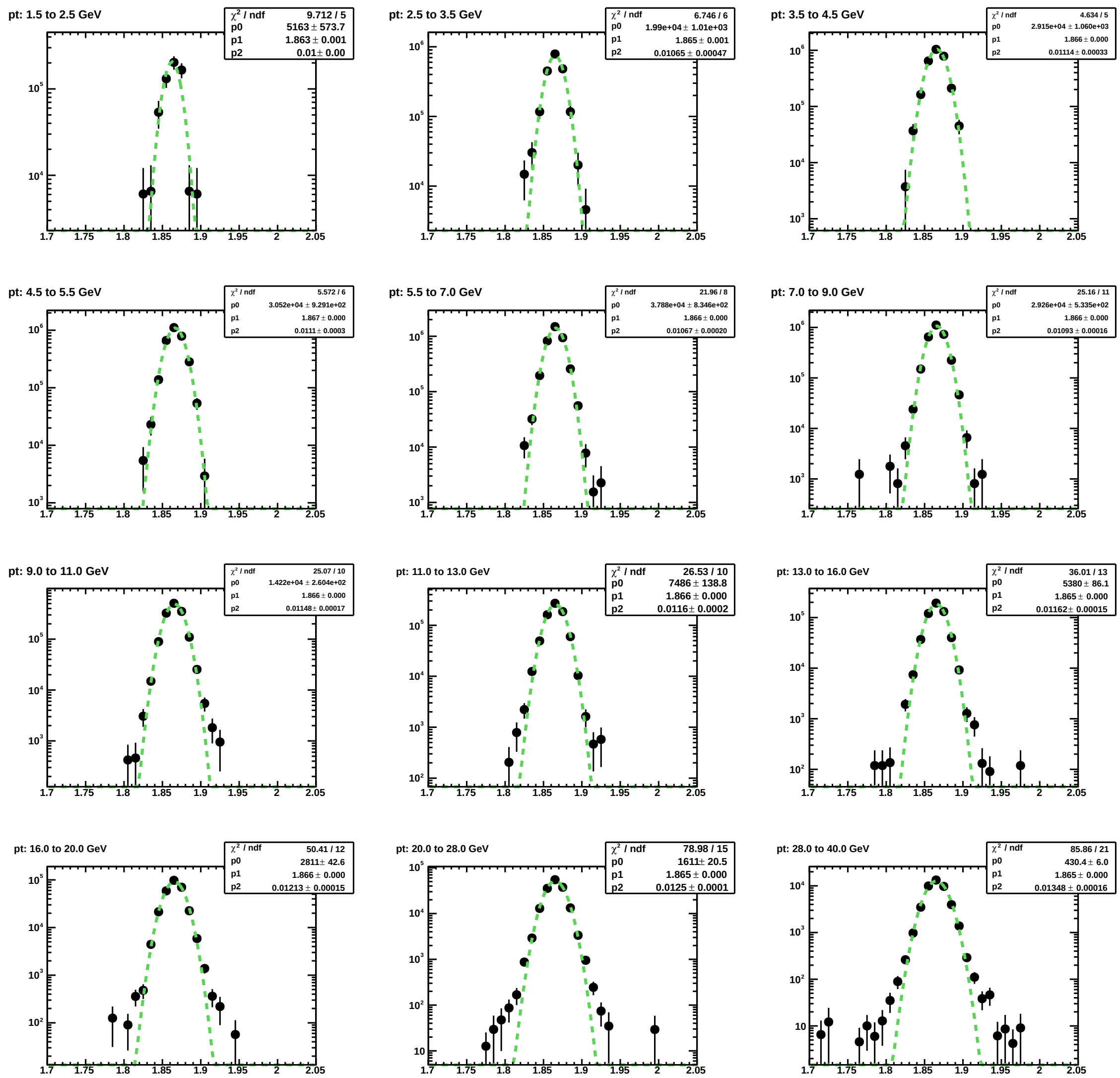

Figure 3.4.: Fit to MC Truth D^0 mass spectrum with a single Gaussian in different p_T intervals with PbPb simulation samples at 2.76 TeV discussed in Section 4.1.1.

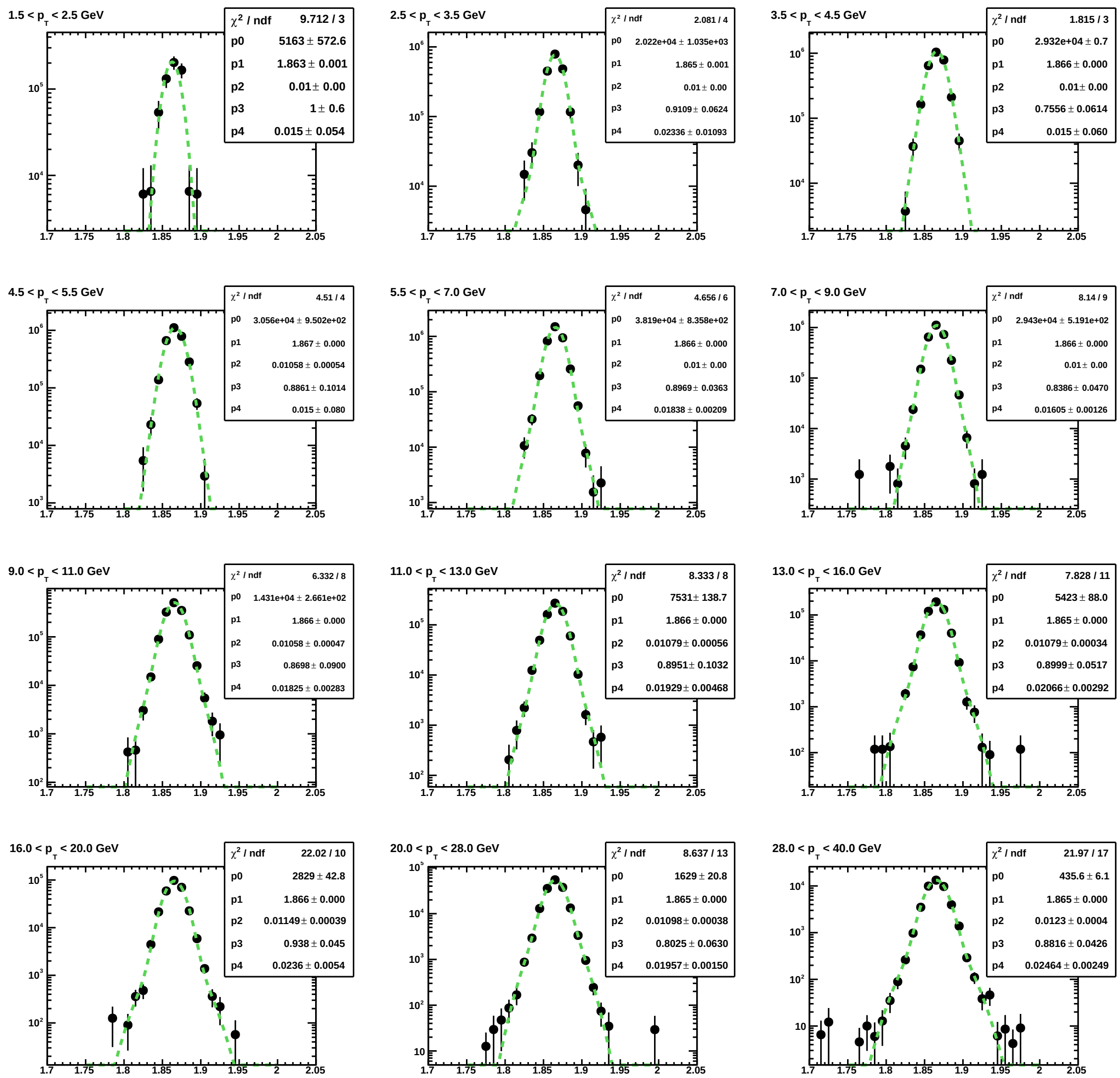

Figure 3.5.: Fit to MC Truth D^0 mass spectrum with two Gaussian functions in different p_{T} intervals for PbPb simulations at 2.76 TeV with PbPb simulation samples at 2.76 TeV discussed in Section 4.1.1.

D^0 signal while the other is background D^0 candidate with wrong mass assignment on tracks. The mass shape of the MC Truth incorrect mass assignment D^0 candidates are fitted with a single Gaussian function in Fig. 3.6 and it is found that a single Gaussian function can describe the mass shape of those candidates well. The MC Truth incorrect mass assignment D^0 candidates are the candidates formed by two tracks from real D^0 signal but with wrong mass assignment on two daughter tracks.

For combinatorial background, a third order polynomial or a exponential function is used because they can describe the mass shape of D^0 candidates in sideband regions in data.

Figure 3.7 shows the example fits to invariant mass distributions of the selected D^0 candidates in several p_{T} intervals for the centrality class 0–100% in PbPb collisions at 2.76 TeV.

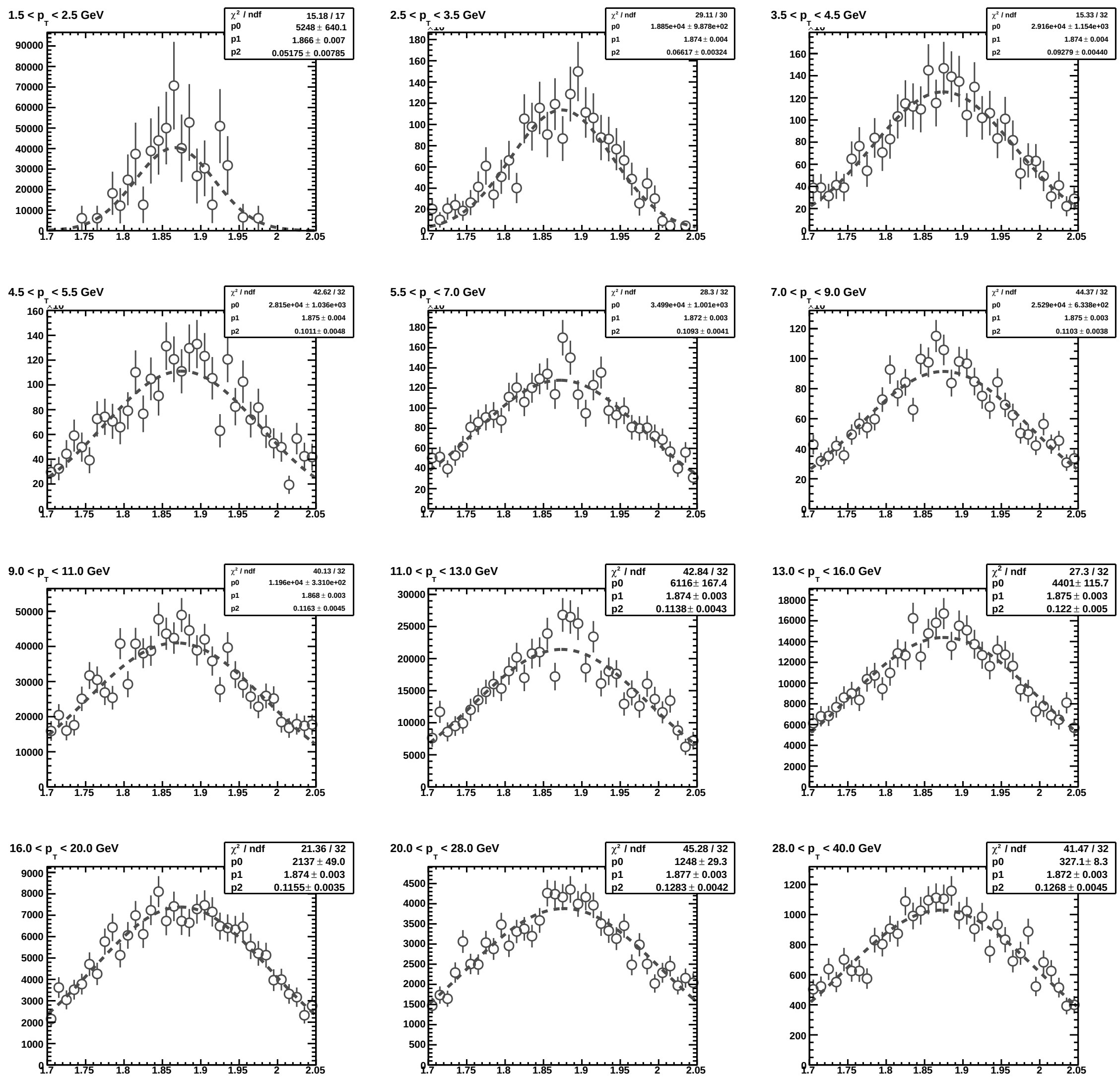

Figure 3.6.: Fit to the mass spectrum of MC Truth incorrect mass assignment D^0 candidates with a single Gaussian in different p_T intervals with PbPb simulation samples at 2.76 TeV discussed in Section 4.1.1.

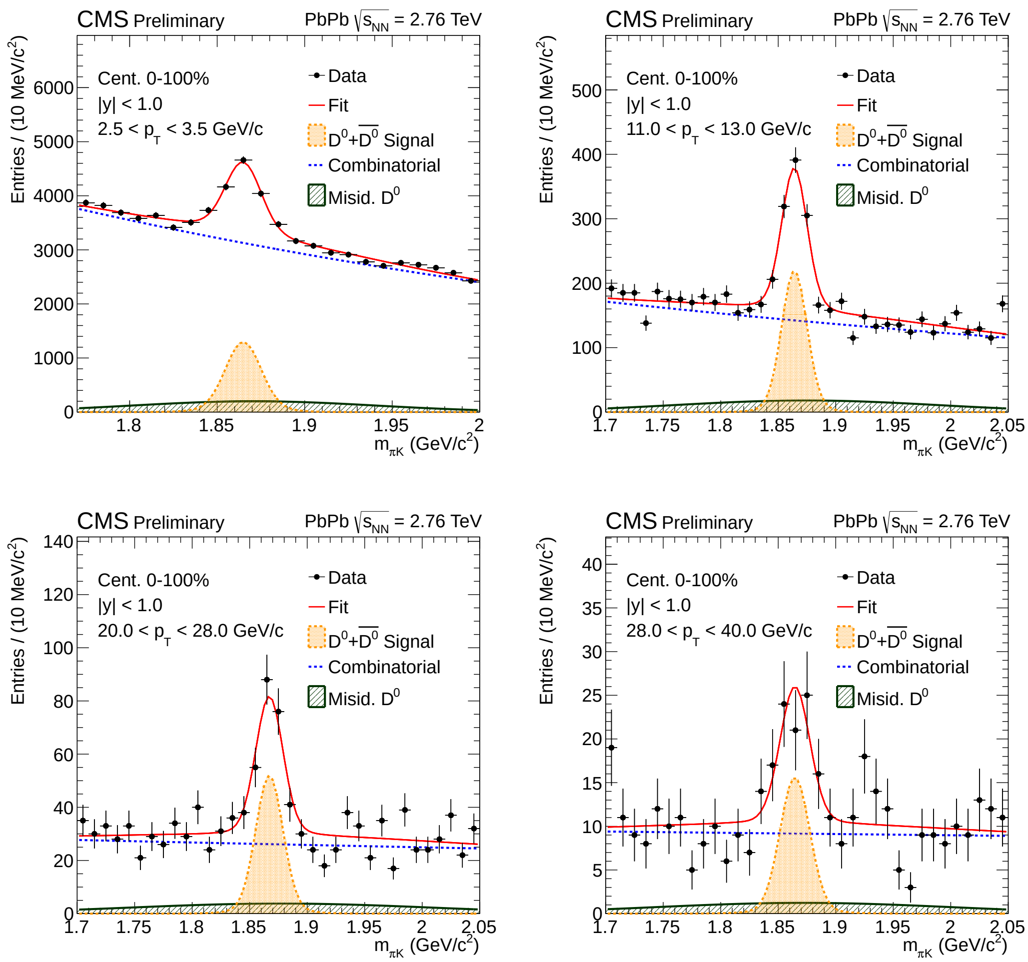

Figure 3.7.: Example fits to invariant mass distributions of D^0 candidates and their charge conjugates in selected p_T intervals for centrality class $0-100\%$ in PbPb collisions at 2.76 TeV. The curves show the fit functions as indicated in the legend.

4. Prompt D^0 Nuclear Modification Factor in PbPb Collisions

This chapter presents the details of the measurement of prompt D^0 nuclear modification factor in PbPb collisions at 2.76 TeV and 5.02 TeV.

4.1 Prompt D^0 Nuclear Modification Factor in PbPb Collisions at 2.76 TeV

This section presents the details of the measurement of prompt D^0 nuclear odification factor in PbPb collisions at 2.76 TeV.

4.1.1 Datasets and Monte Carlo Simulation

This analysis is based on the PbPb data at $\sqrt{s_{\mathrm{NN}}} = 2.76$ TeV collected by the CMS experiment during the 2011 heavy ion run. The data collected by a minimum bias trigger is used. In order to suppress events due to noise, cosmic rays, double-firing triggers, and beam backgrounds, the minimum bias trigger is required to be in coincidence with bunches colliding in the interaction region. These conincident signals may come from either the beam scintillator counters (BSC, $3.23 < |\eta| < 4.65$) or in the steel/quartz-fiber Cherenkov forward hadron calorimeters (HF, $2.9 < |\eta| < 5.2$) from both ends of the detector, as described. The trigger has an acceptance of $(97 \pm 3)\%$ for hadronic inelastic PbPb collisions [86]. The number of events selected by the minimum bias trigger is around 30 million. The event selection used in this analysis is described in detail in previous publications (Refs. [87–90]). The collected events are cleaned for detector noise artifacts with the usage of a hadronic calorimeter (HCAL) noise cleaning filter, and elecromagnetic calorimeter (ECAL) spike removal. Events were sorted into different centrality classes.

Dedicated Monte Carlo (MC) simulations of D^0 mesons are used to determine the signal shape, and evaluate the reconstruction and selection efficiencies. Inclusive QCD events generated by the PYTHIA Monte Carlo generator Tune Z2 [91,92] are filtered for D^0 production and events passing the D^0 filter are embedded into a simulated PbPb background generated by the HYDJET Monte Carlo generator version 1.8 [93]. The parameters of this version of HYDJET are tuned to reproduce the particle multiplicity for different centralities. Around two hundred thousand PYTHIA+HYDJET events are generated for each $\hat{p}_T$ bin with boundaries of [0, 5, 10, 15, 30, 50 , 80, 120, 170]. The D^0 filter requires that there is at least one D^0 with $p_{\mathrm{T}} > 1.0$ GeV/c, and $|\eta| < 2.0$ in the PYTHIA event. In addition, the D^0 decay parameters are redefined such that all D^0 mesons decay through $D^0 \to K^- \pi^+$ channel, which is achieved with the EVTGEN package [94].

4.1.2 MC and Data Comparison

Differences between distributions of the selection variables of D^0 signal in data and MC simulation can introduce bias in efficiency correction. In this section, distributions of the D^0 selection variables are studied for D^0 signal in MC and data. In principle, only distributions of true D^0 signal are plotted in both cases, however this is impossible to ensure in data because of the small signal-to-background ratio. To get distributions of D^0 signal in data, sideband method is used to estimate the distributions of background D^0 candidates. Then the estimated distributions of background D^0 candidates are used to remove the background D^0 candidates in D^0 signal region to get the distributions of real D^0 signal.

The sideband is defined in symmetric windows outside of the true D^0 mass, $0.05\mathrm{GeV}/c^2 < |M_{D^0} - M_{D^0}^{PDG}| < 0.07\mathrm{GeV}/c^2$, while the signal region is defined around the D^0 signal peak, as $|M_{D^0} - M_{D^0}^{PDG}| < 0.03\mathrm{GeV}/c^2$ (D^0 signal width is around 0.015

GeV/c^2). Distributions from simulation are scaled to the entries of data. Prompt and nonprompt D^0 candidates from simulations are scaled according to the fraction of prompt D^0, which is calculated in Section 4.1.4. For each comparison, the prompt D^0 contribution is plotted on the top of the nonprompt D^0 contribution to compare with distributions from data directly.

In data, the signal significance is quite small without D^0 candidate selections of decay length significance ($d_0/\sigma(d_0)$), the pointing angle (α), and vertex probabilty. To get good D^0 signal, the candidates selections applied are:

- $d_0/\sigma(d_0) > 3.5$
- $\alpha < 0.12$
- vertex probability > 0.05

To show how sideband method works in details, the procedure of getting $d_0/\sigma(d_0)$ distribution of D^0 signal with $p_{\mathrm{T}} > 7.0\mathrm{GeV}/c$ in data is showed step by step as followed:

- Cuts on α and vertex probability are applied to increase signal-to-background ratio.
- Fit the mass spectrum as showed in Figure 4.1. With the integral of the backgorund PDF of the fit function, get the number of background candidates in sideband and signal region (N1 and N2).
- Get the $d_0/\sigma(d_0)$ distributions in sideband and signal region, respectively (h1 and h2). So h1 is the $d_0/\sigma(d_0)$ of D^0 background candiates from sideband region and h2 is the $d_0/\sigma(d_0)$ of D^0 signal candidates and background candiates from signal region. Distributions of N2/N1 * h1 and h2 are showed in the left plot of Figure 4.2.
- $d_0/\sigma(d_0)$ distribution of D^0 signal will be h2 - N2/N1 * h1, showed in the right plot of Figure 4.2;

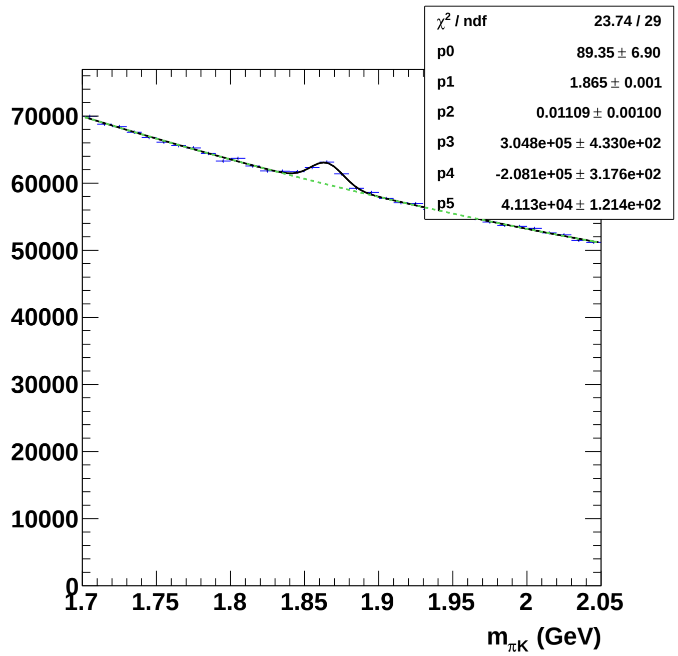

Figure 4.1.: Invariant mass distribution of D^0 candidates in data with $p_{\mathrm{T}} > 7.0\mathrm{GeV}/c$, $\alpha < 0.12$ and vertex probability > 0.05 cuts for centrality class 0-100%.

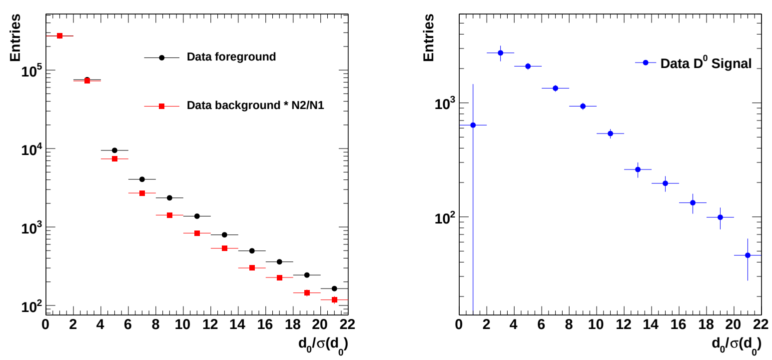

Figure 4.2.: (left) $d_0/\sigma(d_0)$ distributions in sideband scaled by N2/N1 (N2/N1 * h1) (red points) and signal region (h2) (black points). (right) $d_0/\sigma(d_0)$ distribution for D^0 signal in data with $p_{\mathrm{T}} > 7.0\mathrm{GeV}/c$, $\alpha < 0.12$ and vertex probability > 0.05 cuts (h2 - N2/N1 * h1).

Figure 4.3 shows the comparison for D^0 signals with $p_{\mathrm{T}} > 7.0\mathrm{GeV}/c$ for centrality class 0-100%. When one variable is studied, the other selection criteria are applied. Red and blue histograms correspond to nonprompt and prompt D^0 components, respectively. The gray bands in ratio plots are uncertainties from uncertainties of nonprompt D^0 fraction. The plots show that, for D^0 candidate selection variables, MC and data distributions are in reasonable agreement, though with large statistical uncertainty.

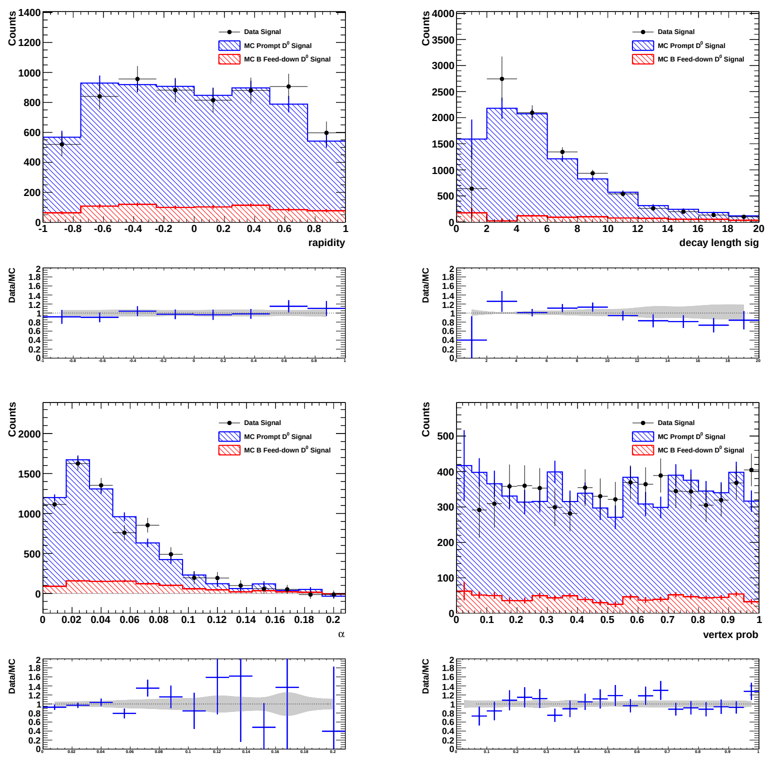

Figure 4.3.: Comparison of variables for centrality class 0-100%. Distributions of rapidity (top left), $d_0/\sigma(d_0)$ (top right), α (mid-left), and vertex probability (mid-right) for D^0 signals from data and MC simulation with $p_{\mathrm{T}} > 7.0\mathrm{GeV}/c$.

The comparison is just done for $p_{\mathrm{T}} > 7.0\mathrm{GeV}/c$ range and it is dificult to do the same study for lower p_{T} range because of small signal-to-background ratio. The remnant discrepancies between distributions of the selection variables of D^0 signal in data and MC simulation showed in Figure 4.3 are studied and considered as source of systematic uncertainties.

4.1.3 Acceptance and Efficiency Correction

The acceptance(α) $\times$ efficiency(ϵ) corrections are computed using the PYTHIA+HYDJET MC simulations and are calculated for prompt and nonprompt D^0 respectively. The efficiency correction is the product of the reconstruction efficiency (ϵ_{reco}) and the selection efficiency (ϵ_{cuts}). Different p_{T} shapes between data and simulation may introduce bias to the correction factors. On the other hand, the generated prompt D^0 p_{T} spectrum is weighted to the measured prompt D^0 spectrum as discussed below. To minimize this bias, the generated non-prompt D^0 spectrum is weighted to R_{AA} scaled nonprompt D^0 spectrum from a fixed-order plus next-to-leading logarithmic (FONLL) [95, 96] calculation for B hadron spectrum and PYTHIA+EVTGEN $B \to D^0$ decay kinetics, which is obtained in Section 4.1.4.

Corrections of acceptance and efficiency can be estimated as a whole by deviding the number of MC Truth D^0 candidates by the number of initially generated D^0. The formula used is the following:

$$\alpha \times \epsilon_{reco+cuts}(p_T, y) = \frac{N^{MC\ Truth\ Candidate}_{|y|<1.0, p_T^{dau\ track} \geq 1.0\mathrm{GeV}/c, |\eta^{dau\ track}|<1.1, all\ track\ quality\ cuts, all\ D^0\ cuts}}{N^{gen}_{|y|<1.0}}, \tag{4.1}$$

where $N^{MC\ Truth\ Candidate}_{|y|<1.0, p_T^{dau\ track} \geq 1.0\mathrm{GeV}/c, |\eta^{dau\ track}|<1.1, all\ track\ quality\ cuts, all\ D^0\ cuts}$ and N^{gen} are the numbers of reconstructed and generated D^0 respectively. It is important to note that in the numerator of Equation 4.1, reconstructed quantities are used for the D^0 p_{T} and y to correct the p_{T} and y resolutions, whereas in the denominator the generator level quantities are used.

$\alpha\times\epsilon_{reco}$ includes effect from the detector accpetance and tracking and is calculated as the following:

$$\alpha \times \epsilon_{reco}(p_T, y) = \frac{N^{MC\ Truth\ Candidate}_{|y|<1.0, p_T^{dau\ track}\geq 1.0\text{GeV}/c, |\eta^{dau\ track}|<1.1, all\ track\ quality\ cuts, no\ D^0\ cuts}}{N^{gen}_{|y|<1.0}} \tag{4.2}$$

ϵ_{cuts} is the D^0 topological cuts efficiency and calculated as the following:

$$\epsilon_{cuts}(p_T, y) = \frac{N^{MC\ Truth\ Candidate}_{|y|<1.0, p_T^{dau\ track}\geq 1.0\text{GeV}/c, |\eta^{dau\ track}|<1.1, all\ track\ quality\ cuts, all\ D^0\ cuts}}{N^{MC\ Truth\ Candidate}_{|y|<1.0, p_T^{dau\ track}\geq 1.0\text{GeV}/c, |\eta^{dau\ track}|<1.1, all\ track\ quality\ cuts, no\ D^0\ cuts}} \tag{4.3}$$

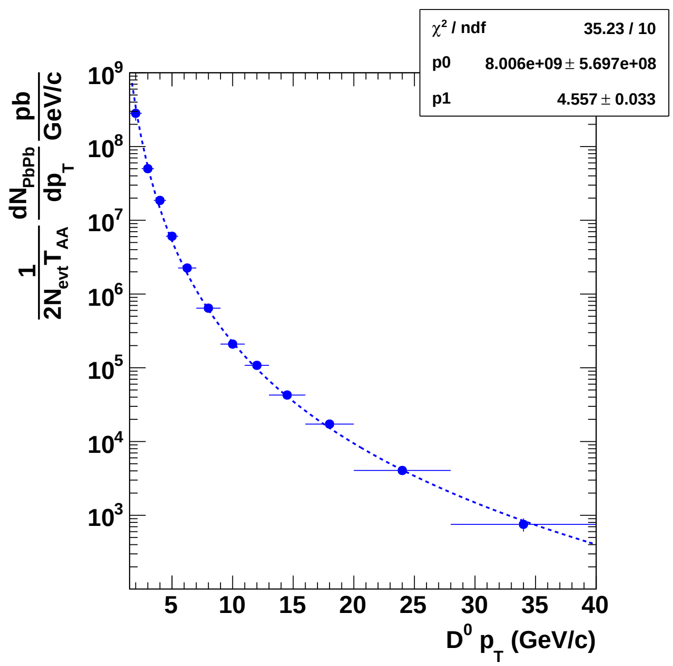

Figure 4.4.: Prompt D^0 spectrum from PbPb data (only with statistical error) fitted with power law function in 0-100% centrality.

To calculate the correction factors, the generated prompt D^0 p_{T} spectrum is weighted to data prompt D^0 spectrum in centrality 0-100% showed in Section 4.1.7. There are three iterations (the last iteration is a stability check) to implement this:

- Iteration 1: The generated prompt D^0 p_{T} spectrum is weighted to FONLL prompt D^0 spectrum, which enables us to get the FONLL weighted prompt D^0

correction factors. The FONLL weighted prompt D^0 correction factors can be used to correct the D^0 raw spectrum to get data prompt D^0 spectrum.

- Iteration 2: The generated prompt D^0 p_T spectrum is weighted to data prompt D^0 spectrum got in iteration 1 and we can get the data spectrum weighted correction factors. With this data weighted correction factor, we get new corrected data prompt D^0 spectrum.

- Iteration 3: The generated prompt D^0 p_T spectrum is weighted to data prompt D^0 spectrum got in iteration 2. Then we can get new data spectrum weighted prompt D^0 correction factors and data prompt D^0 spectrum.

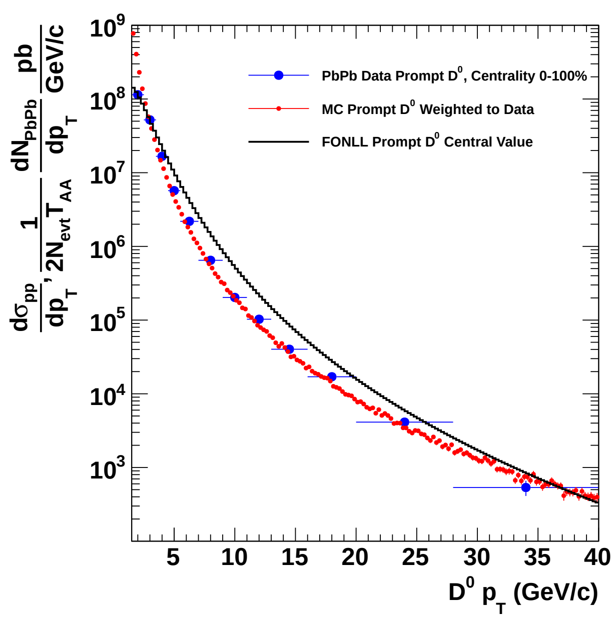

Figure 4.5.: MC prompt D^0 spectrum weighted to data prompt D^0 spectrum, data prompt D^0 spectrum (only with statistical error and FONLL prompt D^0 spectrum).

Figure 4.4 and Figure 4.5 show how the generated prompt D^0 p_T spectrum is weighted to data prompt D^0 spectrum in iteration 2 and 3. Figure 4.4 shows prompt D^0 spectrum from PbPb data (only with statistical error) fitted with power law function in 0-100% centrality. Then MC prompt D^0 spectrum is weighted to the fitted power law function. Figure 4.5 shows the weighted MC prompt D^0 spectrum, which agrees well with prompt D^0 spectrum from PbPb data. And the FONLL prompt D^0 spectrum is also plotted to show the shape difference.

Figure 4.6 shows prompt D^0 acceptance and efficiency from the 3 iterations in 0-100% centrality and the ratios to iteration 2. Difference between $\alpha \times \epsilon$ got from iteration 1 and iteration 2 is within 4.0%. And difference between $\alpha \times \epsilon$ got from iteration 2 and iteration 3 is within 0.1%, which is negligible compared with other systematics. And this small difference means the first two iterations are enough to get data spectrum weighted prompt D^0 correction factors. So in this analysis, correction factors from iteration 2 are used for prompt D^0.

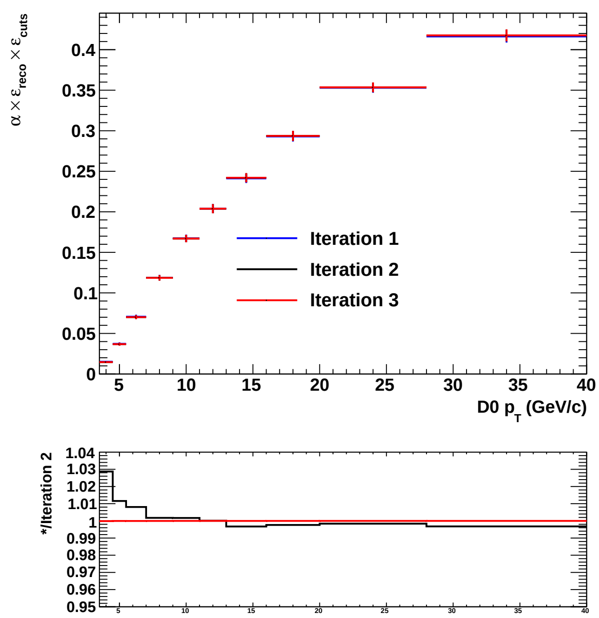

Figure 4.6.: Prompt D^0 acceptance and efficiency from the 3 iterations in 0-100% centrality. The ratios to iteration 2 are also plotted.

Figure 4.7 shows the prompt and nonprompt D^0 $\alpha \times \epsilon_{reco}$, ϵ_{cuts} and $\alpha \times \epsilon_{reco+cuts}$, respectively, as a function of p_{T} for $|y| < 1.0$ and centrality $0 - 100\%$. The $\alpha \times \epsilon_{reco}$

of prompt D^0 is higher than that of nonprompt D^0, which is the consequence of the fact that the heavy-ion tracking efficiency is higher for particles produced closer to the primary vertex. The tracks from prompt D^0 tend to be less displaced from the primary vertex than the tracks from nonprompt D^0. A corresponding effect is seen for ϵ_{cuts}, where the values for prompt D^0 are smaller than nonprompt D^0 because the nonprompt D^0 is more displaced from the primary vertex. The efficiencies are evaluated in centrality classes corresponding to those used in the analysis and the centrality dependence of the efficiency is on the order of 10%.

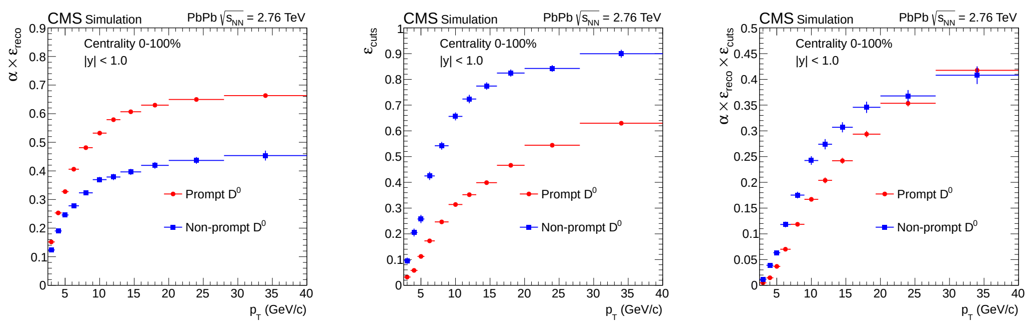

Figure 4.7.: Prompt and nonprompt D^0 $\alpha \times \epsilon_{reco}$ (left), ϵ_{cuts} (middle) and $\alpha \times \epsilon_{reco+cuts}$ (right) as function of p_{T} for $|y| < 1.0$ and centrality $0 - 100\%$

4.1.4 B Feed-down Correction

The number of D^0 from mass spectrum fit in data is the total number prompt D^0 and nonprompt D^0. In order to obtain the prompt D^0 p_{T} spectra, nonprompt D^0 needs to be subtracted from the inclusive D^0 spectra. In this analysis, the prompt D^0 fraction is calcualted based on MC simulations and FONLL calculations, while the prompt D^0 fraction is extracted through template fits on DCA distributions in analysis with PbPb data at 5.02 TeV as discussed in Section 4.2. In this analysis, the basic idea is to calcualted expected number of nonprompt D^0 with FONLL calculation, nonprompt D^0 R_{AA} and $(\alpha \times \epsilon_{reco+cuts})_{nonprompt\ D^0}$. The detail equations are as followed:

$$f_{prompt} = 1 - \frac{N^{raw}_{nonprompt\ D^0}}{\frac{1}{2} N^{raw}_{D^0}} \tag{4.4}$$

$$N^{raw}_{nonprompt\ D^0} = T_{AA} \cdot \left(\frac{d\sigma_{pp}}{dp_{\mathrm{T}}}\right)^{FONLL}_{nonprompt\ D^0} \cdot R^{nonprompt\ D^0}_{AA} \cdot (\alpha \times \epsilon)_{nonprompt\ D^0} \cdot \Delta p_{\mathrm{T}} \cdot Br \cdot N_{\mathrm{MB}} \tag{4.5}$$

The ingredients entering Equation 4.4 and 4.5 are:

- $N^{raw}_{D^0}$: raw number of D^0 from mass spectrum fit in data;
- $\frac{1}{2}$ is because the number from mass spectrum fit is the total number of D^0 and its antiparticle;
- $N^{raw}_{nonprompt\ D^0}$: expected raw number of nonprompt D^0 from calculation;
- T_{AA}: the nuclear overlap function which varies with the centrality;
- $\left(\frac{d\sigma_{pp}}{dp_{\mathrm{T}}}\right)^{FONLL}_{nonprompt\ D^0}$: nonprompt D^0 spectrum from FONLL B hadron spectrum and PYTHIA+EVTGEN decay kinetics;
- $R^{nonprompt\ D^0}_{AA}$: nonprompt D^0 R_{AA} converted from nonprompt J/ψ R_{AA} and B-Jet R_{AA}, which will also be discussed in details later;
- $(\alpha \times \epsilon)_{nonprompt\ D^0}$: $(\alpha \times \epsilon)$ of nonprompt D^0;
- N_{MB} is the number of minimum bias events sampled by the event selection;
- Br is the branching fration of $D^0 \to K^- \pi^+$, which is $3.88 \pm 0.05\%$;

In the 0–100% centrality range, the non-prompt J/ψ results are taken from the preliminary results from HIN-12-014 PAS [97] and the b-jet results [98]. There is no measurements available in the p_{T} range below 3 GeV/c and the $R_{AA} = 1 \pm 1$ is assumed in this range. Based on the b-jet R_{AA} measurements, $R_{AA} = 0.5 \pm 0.5$ is used in the p_{T} range above 30 GeV$/c$. The non-prompt J$/\psi$ R_{AA} values for centrality class 0–100% used in this study is summarized in left panel of Figure 4.8. For the centrality dependent results, the R_{AA} between 6.5-30 GeV used in this study is shown in the right panel of Figure 4.8.

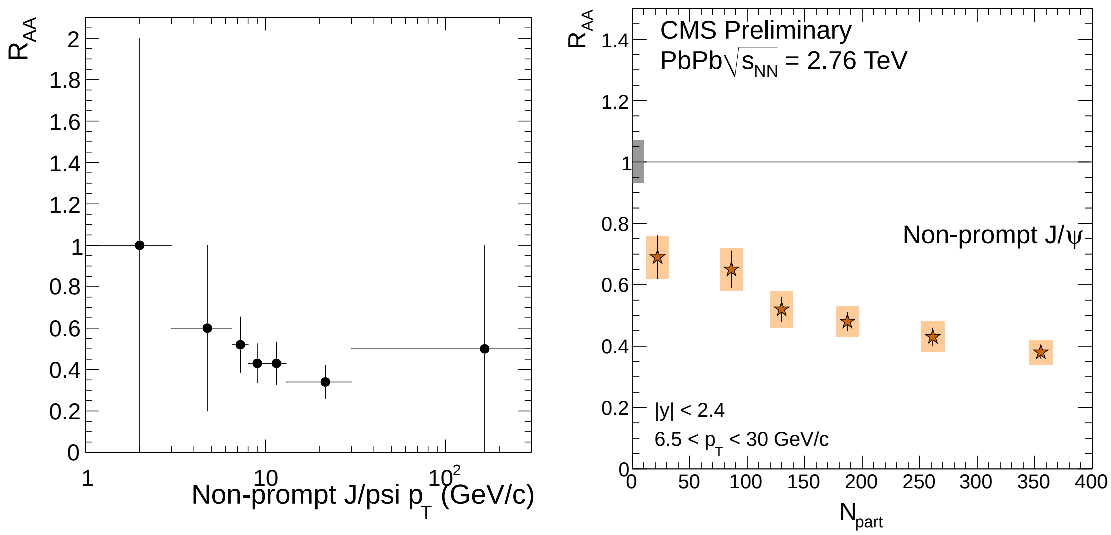

Figure 4.8.: (left) Non-prompt J$/\psi$ R_{AA} in the centrality interval 0–100% used in this study. (right) Non-prompt J$/\psi$ R_{AA} in the centrality interval 0–10%, 10–20%, 20–30%, 30–40%, 40–50% and 50–100% from the HIN-12-014 PAS [97].

In order to obtain the non-prompt D^0 and J$/\psi$ spectra from FONLL calculation, the first step is to calculate the B meson spectra from the FONLL web interface. The decay of B mesons is handled by EvtGen to obtain the non-prompt D^0 and J$/\psi$ spectra. In order to obtain the B meson p_{T} spectra in different centrality bins, the correlation between B meson p_{T} and daughter J$/\psi$ p_{T} is studied which is shown in left panel of Figure 4.9. Using this correlation matrix, the B meson p_{T} spectra and R_{AA} can be calculated form the non-prompt J$/\psi$ R_{AA}. The results are shown in right panel Figure 4.9.

The correlation matrix of B meson p_{T} and the daughter D^0 meson p_{T} is shown in left panel of Figure 4.10. The B meson spectra obtained in the previous section

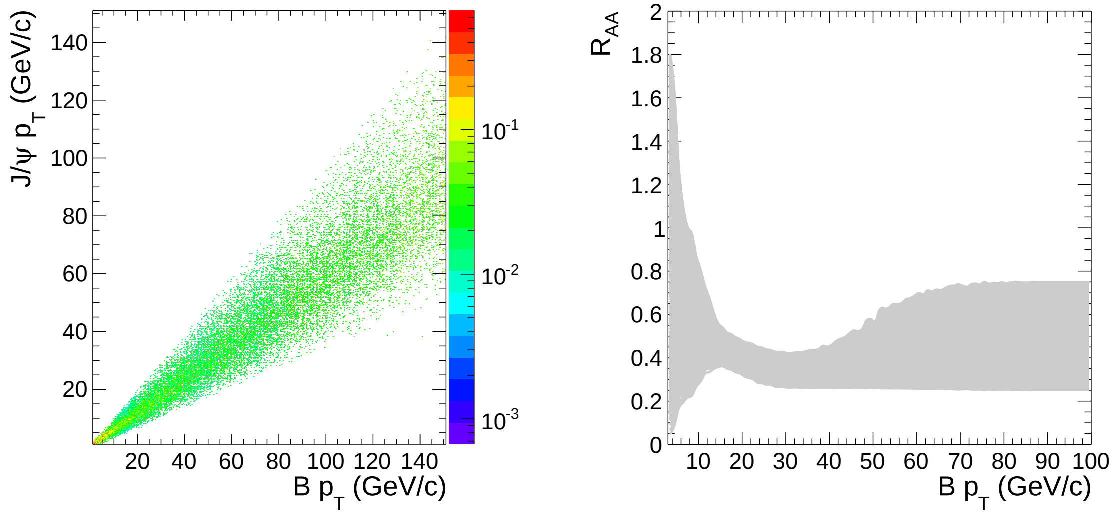

Figure 4.9.: (left) The correlation matrix between B meson p_{T} and daughter J/ψ p_{T} obtained from PYTHIA+EVTGEN. (right) The converted B meson R_{AA} band.

is folded with the correlation materix to produce the non-prompt D^0 spectra. Right panel of Figure 4.10 shows the results for 0–100%.

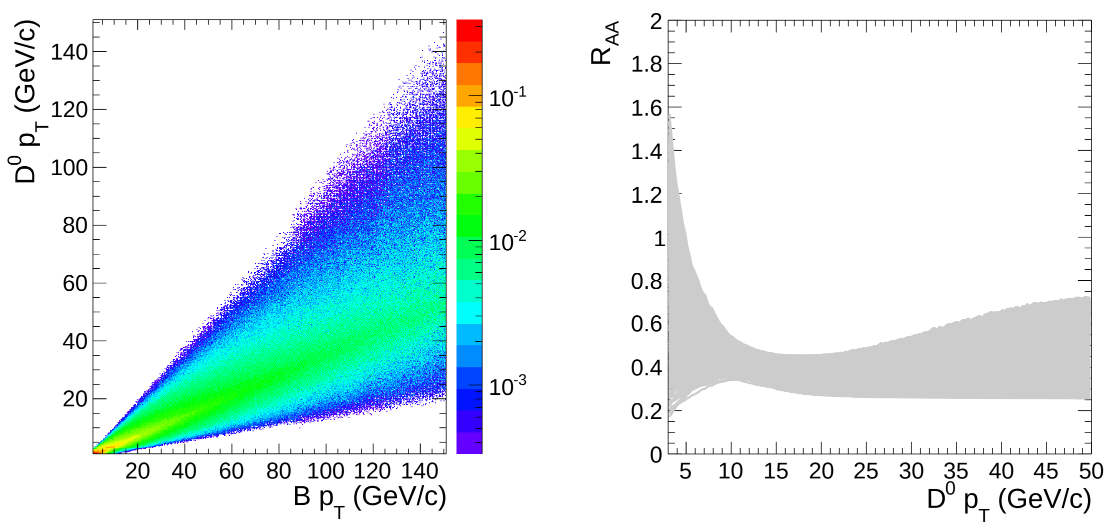

Figure 4.10.: (left) The correlation matrix between B meson p_{T} and daughter D^0 p_{T} obtained from PYTHIA+EVTGEN. (right) The converted non-prompt D^0 R_{AA} band.

Figure 4.11 shows the calculated prompt D^0 fraction $(90-97\%)$ in raw data yield for centrality class 0–100%.

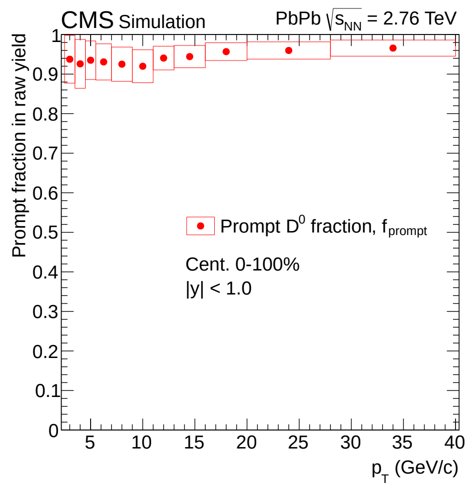

Figure 4.11.: Calculated prompt D^0 fraction in raw data yield for centrality class 0–100%. The open boxes represent the uncertainties of prompt D^0 fraction.

4.1.5 pp Reference at 2.76 TeV

The pp reference used in the analysis is composed of a data-extrapolated reference and a calculation from FONLL. In the range $p_{\mathrm{T}} < 16\mathrm{GeV}/c$, results from the ALICE prompt D^0 measurements at 7 TeV [99] are rescaled to 2.76 TeV with FONLL calculation. The procedure in Ref. [100] is imitated. In the range $p_{\mathrm{T}} > 16\mathrm{GeV}/c$ where data run out of statistics, pure FONLL calculation is used as pp reference. For the FONLL calculation used in scaling data and as a pp reference, the CTEQ6.6 parton distribution functions were considered. The central values of the calculations are obtained considering $\mathrm{m_c}$=1.5 GeV, while the renormalization and factorization scales μ_R=μ_F= μ_0=$\sqrt{\mathrm{m}^2 + \mathrm{p}_{\mathrm{T}}^2}$. The uncertainty band is evaluated by varying the perturbative parameters in the range $1.3 < \mathrm{m_c} < 1.7\ \mathrm{GeV}/c^2$ and μ_F and μ_R independently in the range $0.5 < \mu_F/m_T < 2$, $0.5 < \mu_R/m_T < 2$ with the constraint of

$0.5 < \mu_F/\mu_R < 2$. The pp reference used in this analysis is showed as filled and open triangles in Figure 4.12.

4.1.6 Systematic Uncertainties

Systematic uncertainties on the D^0 R_{AA} include the uncertainties on the D^0 cross section in PbPb collisions and the pp reference. The uncertainties on pp reference has been included when it is built as discussed in Section 4.1.5. Therefore, the uncertainties discussed here are from PbPb data. The sources of systematic uncertainties include the mass spectrum fit, efficiency correction, B feed-down correction, branching fraction, T_{AA}, and N_{MB}.

The systematic uncertainty on the tracking efficiency is 3.9% [101], thus the uncertainty on reconstruction efficiency from tracking efficiency is 7.8% for D^0. Besides, another 5.0% uncertainty is assigned based on MC closure study. Thus the total uncertainty on reconstruction efficiency is 9.3%.

The systematic uncertainty on the D^0 selection efficiency is evaluated as the ratio of each individual selection criteria (e.g. α, $d_0/\sigma(d_0)$, and vertex probability) between data and MC while other selections are applied. For example, the systematic uncertainty from the α parameter is obtained by taking the ratio between data and MC of the α distribution while the selections on $d_0/\sigma(d_0)$ and vertex probability are applied. The uncertainty on the selection efficiency is found to be 14.1%, 5.2% and 11.4% for centrality ranges 0–30%, 30–100% and 0–100%, respectively.

In calculations of efficiency corrections, the generated prompt D^0 p_{T} spectrum is weighted to fitted function of data prompt D^0 spectrum. The shape of fitted function can change slightly if the statistical and systematic uncertainties are taken into account. To evaluate the uncertainty from the p_{T} shape, the prompt D^0 p_{T} distribution is applied a weight, which varies linearly from 1.3 to 0.7 (or from 0.7 to 1.3) over the p_{T} range analyzed to account for the maximum variations from the statistical and systematic uncertainties. The uncertainty is evaluted by the relative differences on the efficiency corrections and found to be 1.0%.

The D^0 reconstruction efficiency decreases sharply as d_0 increases, thus the differences in d_0 distributions of D^0 signal between data and MC can introduce a bias in the efficiency corrections. This uncertainty is evaluated by calculating the ratio of d_0 cut efficiencies in data and MC and found to be 5.0%.

The systematic uncertainty on the mass spectrum fit is evaluated by varying PDFs used to fit both the signal and the background distributions. The background PDF is changed to a linear and a second order polynomial background function and the signal yields extracted are compared with the default yield to estimate the uncertainty from the background PDF. The uncertainty from the signal PDF is obtained by floating the widths of the two gaussians with a fixed ratio to model the D^0 signal, which can account for the possible differences in resolution between data and simulatio. The total uncertainty on mass spectrum fit is found to be 5-25% depending on p_{T} and centrality.

The systematic uncertainty on the B meson feed-down correction is evaluated by adding all individual uncertainties from Eq.(4.5) in quadrature. The total uncertainty on the prompt D^0 fraction is between 1-15% depending on the p_{T} and centrality.

The total systematic uncertainty on the D^0 cross section in PbPb collisions is computed as the sum in quadrature of all the different contributions. The uncertainties for centrality 0-100% are summarized in Table 4.1. The systematic uncertainties for ther centrality classes studied in this analysis are studied in the same way.

4.1.7 Results

The prompt D^0 cross section normalized by T_{AA} in PbPb collisions is calculated as:

$$\frac{1}{T_{\mathrm{AA}}} \left. \frac{dN_{PbPb}}{dp_{\mathrm{T}}} \right|_{|y|<1} = \frac{1}{T_{\mathrm{AA}}} \frac{1}{2} \frac{1}{\Delta p_{\mathrm{T}}} \frac{1}{N_{\mathrm{MB}}\, \mathcal{B}} \left. \frac{f_{\mathrm{prompt}}\, N_{PbPb}}{(\alpha \times \epsilon)_{\mathrm{prompt}}} \right|_{|y|<1}, \tag{4.6}$$

Source	p_{T} interval (GeV/c)					
	2.5-3.5	3.5-4.5	4.5-5.5	5.5-7.0	7.0-9.0	9.0-11.0
Tracking efficiency	9.3%					
D^0 selection efficiency	11.4%					
D^0 decay length consistency	5.0%					
MC p_{T} shape	1.0%					
Signal extraction	7.0%	7.0%	7.0%	7.0%	7.0%	7.0%
B feed-down correction	6.4%	6.7%	5.2%	4.9%	4.7%	4.5%
Sum	18.2%	18.3%	17.9%	17.8%	17.7%	17.7%
Source	p_{T} interval (GeV/c)					
	11.0-13.0	13.0-16.0	16.0-20.0	20.0-28.0	28.0-40.0	
Tracking efficiency	9.3%					
D^0 Selection Efficiency	11.4%					
D^0 decay length consistency	5.0%					
MC p_{T} shape	1.0%					
Signal Extraction	7.0%	7.0%	7.0%	11.3%	17.9%	
B feed-down correction	3.2%	3.0%	2.3%	2.3%	2.1%	
Sum	17.4%	17.3%	17.2%	19.4%	23.8%	
Branching fraction	1.3%					
T_{AA}	5.7%					
N_{MB}	3.0%					
Sum	6.6%					

Table 4.1.: Summary of relative systematics from data for centrality $0-100\%$.

where T_{AA} is the nuclear overlap function which varies with the centrality [102], Δp_{T} is the width of the p_{T} interval, N_{MB} is the number of MB events sampled by the event selection, $\mathcal{B}$ is the branching fraction of the $D^0 \to K^- \pi^+$ channel, $(\alpha \times \epsilon)_{\mathrm{prompt}}$ is the prompt D^0 acceptance and efficiency, f_{prompt} is the fraction of prompt D^0, and N_{PbPb} is the raw yield of D^0 signal in each p_{T} interval. The factor 1/2 accounts for the fact that N_{pp} is the total yield of D^0 and $\overline{D}^0$. Figure 4.12 shows the prompt D^0

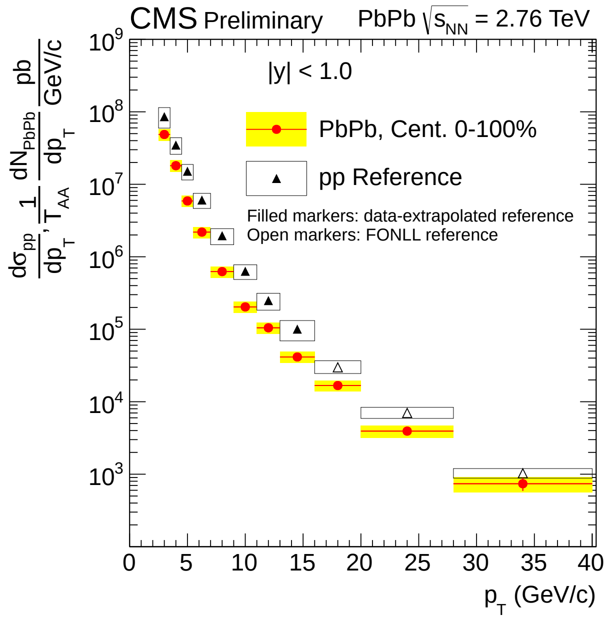

Figure 4.12.: Cross section of prompt D^0 from PbPb data (red circles) for centrality class 0-100% and pp reference (filled and open triangles). For PbPb data, the errors represent statistical errors and the filled boxes represent systematic errirs. For pp reference, the open boxes represent total uncertainties.

cross section normalized by T_{AA} in PbPb collisions at 2.76 TeV for centrality class $0-100\%$ (red circles). For comparison, the pp reference extracted as described in Section 4.1.5 is showed as filled and open triangles. This figure clearly shows that the D^0 cross section in PbPb data is significantly lower than that of the pp reference, indicating that prompt D^0 production in PbPb collisions is strongly suppressed.

Figure 4.13 shows the prompt D^0 R^*_{AA} as a function of p_{T} for centrality classes $0-100\%$ (left) and $0-10\%$ (right). To denote that the pp reference used in this analysis is not measured pp reference spectrum, the measured nuclear modification factor of prompt D^0 is named R^*_{AA}. The R^*_{AA} indicates a trend toward less suppression in high p_{T} range though the differences of the references should be taken into account.

The centrality dependence of prompt D^0 R^*_{AA} is also studied in six p_{T} intervals and four centrality bins. Figure 4.14 shows the prompt D^0 R^*_{AA} as function of p_{T} in

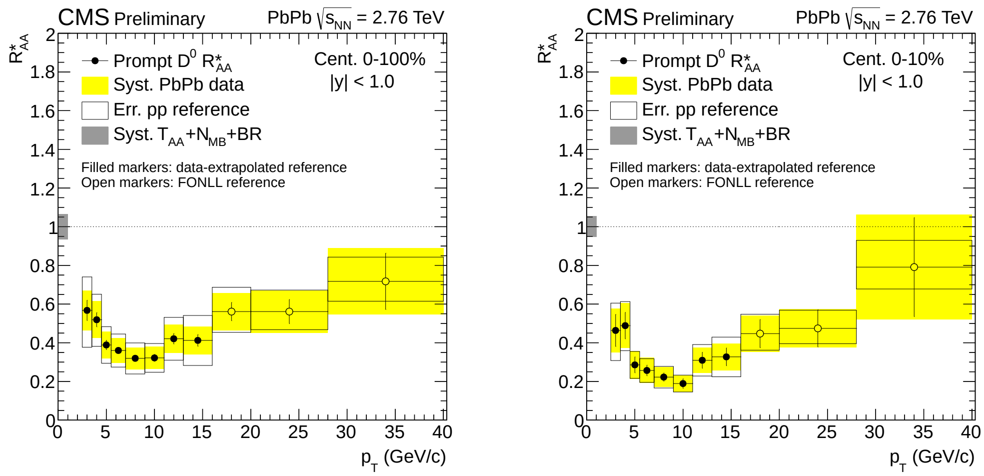

Figure 4.13.: Prompt D^0 R^*_{AA} from PbPb data as function of p_{T} for centrality classes 0-100% (left) and 0-10% (right). The error bars represent statistical errors and the filled boxes represent systematic errors from data only. The open boxes are the errors from pp reference. Systematic errors from T_{AA}, N_{MB} and $D^0 \rightarrow K^- \ \pi^+$ branching fraction are represented by the gray boxes around unity.

centrality classes 0-10%, 10-30%, 30-50% and 50-100%. It is found that the supression of prompt D^0 is larger in central collisions than in peripheral collisions.

In addition, the prompt D^0 R^*_{AA} is compared with charged particle and nonprompt J/ψ R_{AA}. Figure 4.15 shows charged particle R_{AA} ($7.2 < p_{\mathrm{T}} < 9.6$GeV/$c$, $|\eta| < 1.0$) [43], prompt D^0 R^*_{AA} ($8.0 < p_{\mathrm{T}} < 16.0$GeV/$c$, $|y| < 1.0$) and nonprompt J/ψ R_{AA} ($6.5 < p_{\mathrm{T}} < 30.0$GeV/$c$, $|y| < 1.2$) [97] as a function of N_{part}. It is interesting to notice that the prompt D^0 R^*_{AA} falls between charged particle R_{AA} and nonprompt J/ψ R_{AA}, but the uncertainties and the different kinetic ranges should be taken into account.

Figure 4.16 shows comparison of prompt D^0 R^*_{AA} results of this analysis and R_{AA} results from the ALICE collaboration [103] for centrality class 0-20%. While the measurements from ALICE are within the rapidity range $|y| < 0.5$, and the

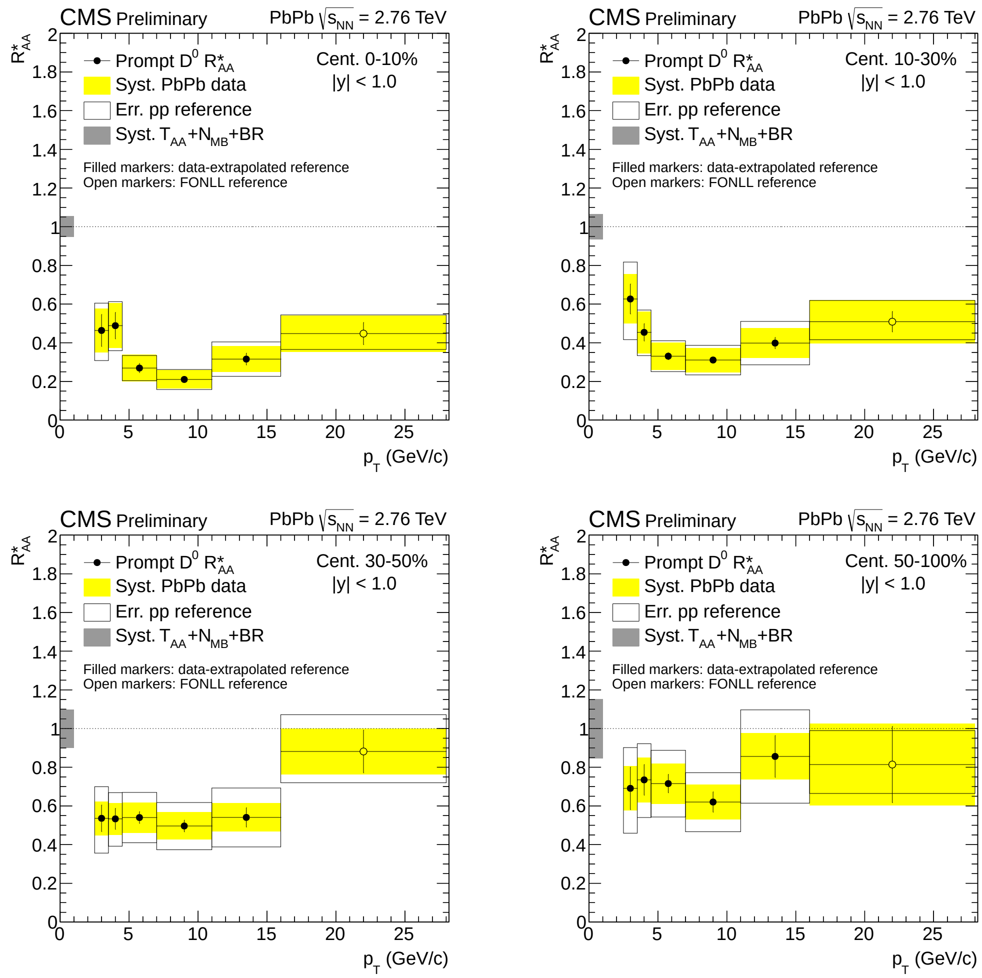

Figure 4.14.: Prompt D^0 R^*_{AA} as function of p_{T} for centrality classes 0-10% (top left), 10-30% (top right), 30-50% (bottom left), and 50-100% (bottom right). The error bars represent statistical errors and the filled boxes represent systematic errors from data only. The open boxes are the errors from pp reference. The systematic errors from T_{AA}, N_{MB} and the $D^0 \to K^- \ \pi^+$ branching ratio are represented by the gray boxes around unity.

measurements from CMS are for the rapidity range $|y| < 1.0$, the two results are consistent within uncertainties.

From above results, it is clear that the production of D^0 mesons are significantly suppressed in semi-central to central PbPb collisions at 2.76 TeV, indicating strong

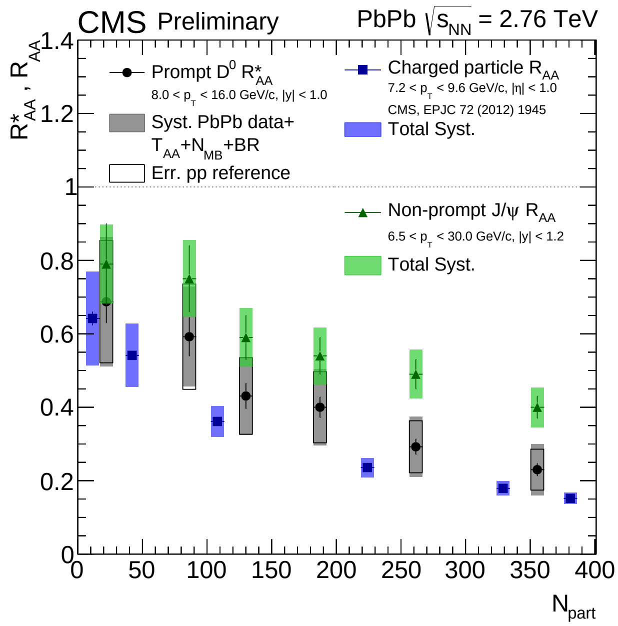

Figure 4.15.: Charged particle R_{AA} (blue squares) [43], preliminary prompt D^0 R^*_{AA} (black circles) and nonprompt J/ψ R_{AA} (green triangles) [97] as function of N_{part}. The systematic errors of charged particle and nonprompt J/ψ R_{AA}, showed as blue and green boxes respectively, include systematic uncertainties from integrated luminosity of the pp data sample and T_{AA}.

energy loss of charm quarks in the medium. The centrality dependence of the suppression is observed.

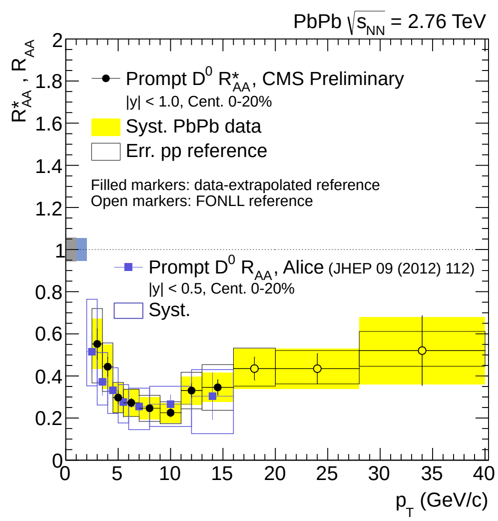

Figure 4.16.: Comparison of prompt D^0 R^*_{AA} as measured by the CMS Collaboration (black circles) and R_{AA} as measured by the ALICE Collaboration (blue squares) [103] as function of p_{T} for centrality class 0–20%. Measurements from ALICE are for rapidity $|y| < 0.5$, while measurements from CMS are for rapidity $|y| < 1.0$.

4.2 Prompt D^0 Nuclear Modification Factor in PbPb Collisions at 5.02 TeV

This analysis has the following main differences compared with the analysis at 2.76 TeV: first, the pp reference in this analysis is measured D^0 cross section with pp data; second, dedicated HLT D^0 triggers are used during pp and PbPb data taking in 2015, thus this analysis reaches much higher p_{T} than the analysis at 2.76 TeV; third, the prompt D^0 fraction is extracted in a data-driven way in this analysis, which is different from the method used in the analysis at 2.76 TeV. In the following sections, we will focus on these differences.

4.2.1 Datasets and Monte Carlo Simulation

This analysis is performed using the pp and PbPb data at $\sqrt{s_{\mathrm{NN}}} = 5.02$ TeV collected in 2015. The total pp sample corresponds to an integrated luminosity of 25.8 pb^{-1} while the PbPb sample to an integrated luminosity of 531 μb^{-1}. The data selected by minimum-bias and D^0 meson triggers is used. The detailed descriptions of the MB triggers can be found in Ref. [42] and detailed descriptions of D^0 triggers will be discussed later. The MB pp sample corresponds to about 2.5 billion events and the PbPb MB samples to about 300 million of events.

To reject events from background processes (beam-gas collisions and beam scraping events), events are required to pass a set of selection criteria in offline analysis as described in Ref. [42]. Both pp and PbPb events are to have at least one reconstructed primary, formed by two or more associated tracks and required to have a distance from the nominal interaction region of less than 15 cm along the beam axis. The PbPb collision events are also required to have at least three towers in each of the HF detectors with energy deposits of greater than 3 GeV per tower.

The Monte Carlo simulations are produced in the similar strategy as the ones used in the D^0 R_{AA} analysis in PbPb collisions at 2.76 TeV discussed in Section 4.1.1.

4.2.2 D^0 Trigger

In order to enhance the statistics of high p_{T} D^0 mesons, dedicated HLT D^0 triggers were designed for both pp and PbPb data taking. Since high p_{T} D^0 mesons are usually associated with jets and high energy calorimeter towers in the HCAL, the HLT D^0 meson triggers are seeded by L1 jet triggers, which are gated with a "BPTX_AND" requrement (both proton or lead beams are present, meaning a collision could happen) in order to lower the L1 rate. To cope with the large underlying event (UE) contribution in PbPb, the L1 jet triggers are constructed with jets with UE removed (denoted as "S1Jet", stage 1 L1 trigger upgrade), using the average energy from a ϕ ring based algorithm. For events in which the desidered L1-seed fired, a track reconstruction routine is performed at HLT, which is adopted from the offline track reconstruction.

After the tracks are reconstructed, D^0 candidates are built at HLT by associating pairs of tracks with opposite charges. To reduce the background contamination and the HLT rate, some topological selections is also applied at HLT, which are lower than the selections in offline analysis to account for the online and offline differences. The L1 triggers associated with each D^0 trigger paths are shown in Table 4.2.

The data collected by the minimum-bias triggers are used to evaluate the D^0 meson trigger efficiency. The trigger efficiencies for both pp and PbPb collisions are defined as following: the denumerators are defined as the number of events with a leading D^0 (candidate with highest p_{T}) that fullfil the loose D^0 selection requirements, while the numerators are the number of events that fires the corresponding HLT D^0 trigger. Figure 4.17 shows the L1 and HLT trigger efficiency as a function of the p_{T} of the leading D^0 candidate for pp data. The trigger efficiency reaches 100% at high p_{T}. Samples recorded with different trigger paths are combined together for the analyses.

In the left panel of Fig 4.18, the L1 trigger efficiency in PbPb are presented as a function of p_{T}. In Fig 4.19, the efficiencies of the D^0 mesons triggers in PbPb collisions are presented. In the left panel, the trigger efficiencies of the trigger paths

Table 4.2.: L1 jet trigger seeds for each D^0 meson trigger path during pp and PbPb data-taking period at 5.02 TeV

DataSet	HLT trigger threshold (GeV/c)	L1 trigger	comment
pp	8	L1_SingleJet16_BptxAND	
pp	15	L1_SingleJet24_BptxAND	
pp	20	L1_SingleJet28_BptxAND	
pp	30	L1_SingleJet40_BptxAND	
pp	50	L1_SingleJet48_BptxAND	Unprescaled
PbPb	20	L1_MinimumBias	
PbPb	40	L1_SingleS1Jet28_BptxAND	
PbPb	60	L1_SingleS1Jet44_BptxAND	Unprescaled

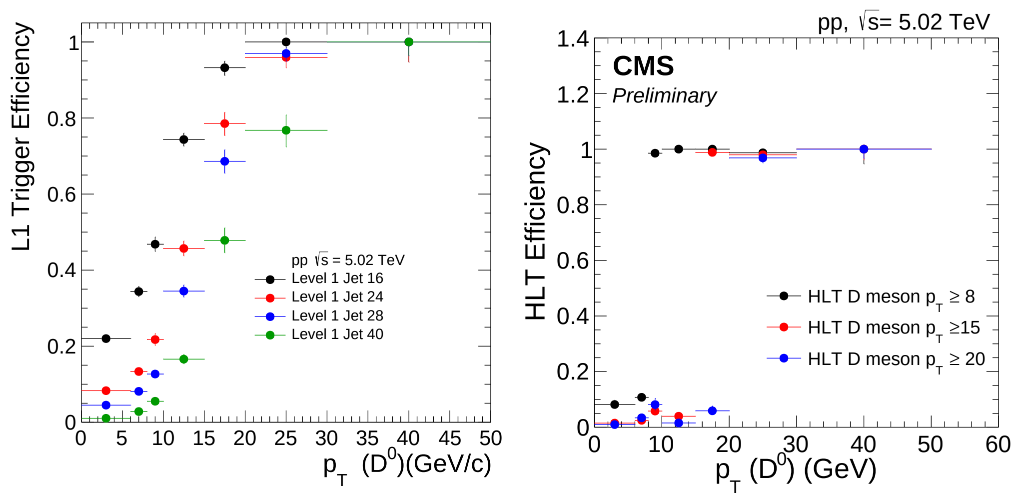

Figure 4.17.: L1 (left) and HLT (right) trigger efficiency as a function of the leading D^0 candidate p_{T} for pp data.

with thresholds at 20, 40, and 60 GeV/c are presented separately as a function of p_{T}. In Fig 4.19(right), the final turn on curve used for deriving the trigger efficiency correction is presented. The HLT trigger efficiency of the algorithm used in each p_{T}

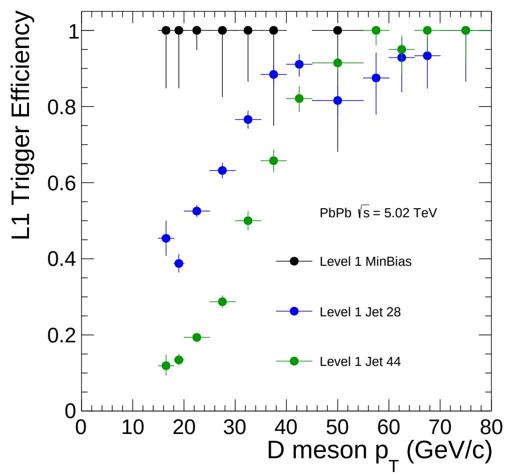

Figure 4.18.: L1 trigger efficiency as a function of the leading D^0 candidate p_{T} for PbPb data.

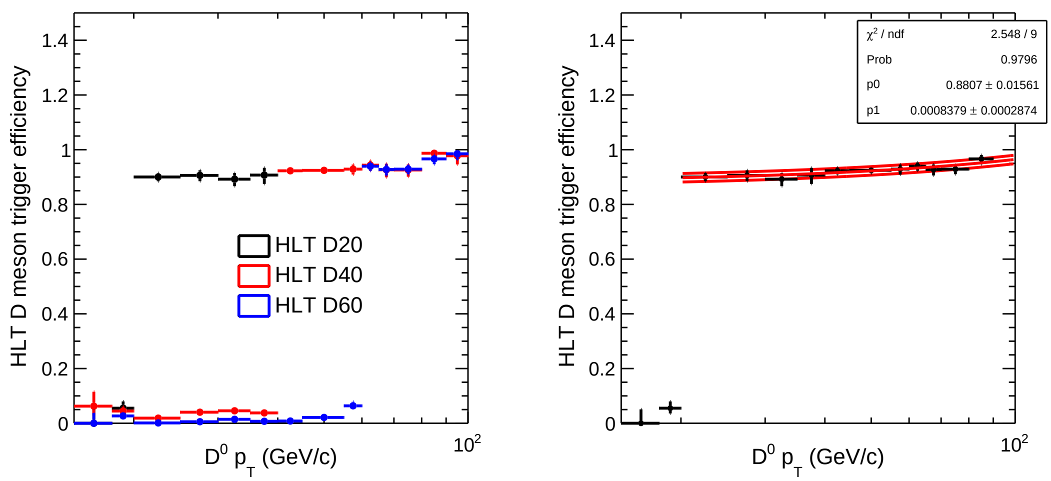

Figure 4.19.: (Left) Trigger efficiencies of the the trigger paths with thresholds at 20, 40, and 60 GeV/c as a function of p_{T}. (Right) Final turn on curves used for deriving the trigger efficiency correction fitted with a linear function.

interval was considered (See Table 4.3). The global turn on curve was fitted with a linear function, that is used to correct the final cross section. The systematic

Table 4.3.: Summary of HLT paths used in the pp and PbPb analysis in different D^0 p_{T} intervals.

Data	p_{T} interval	HLT trigger threshold (GeV/c)
pp	$p_{\mathrm{T}} < 20$	MinimumBias
pp	$20 < p_{\mathrm{T}} < 40$	15
pp	$40 < p_{\mathrm{T}} < 60$	30
pp	$60 < p_{\mathrm{T}} < 80$	50
PbPb	$p_{\mathrm{T}} < 20$	MinimumBias
PbPb	$20 < p_{\mathrm{T}} < 40$	20
PbPb	$40 < p_{\mathrm{T}} < 60$	40
PbPb	$60 < p_{\mathrm{T}} < 80$	60

uncertainty on the trigger efficiency (2%) is defined by the uncertainty on the zero polynomial coefficient of the fit.

4.2.3 B Feed-down Correction

The D^0 signal in data includes both prompt and nonprompt D^0. In order to obtain the prompt D^0 spectra, D^0 from B decays needs to be subtracted from the inclusive D^0 spectra. In this analysis, the prompt D^0 fraction is evaluated with a data-driven method, which performs a template fit on the distribution of DCA of D^0 signal to primary vertex with the DCA shapes of prompt and nonprompt D^0 from the PYTHIA+HYDJET simulations.

Figure 4.20 shows a cartoon of the nonprompt D^0 DCA. For prompt D^0, since they are directly from the primary vertex, the physics D^0 DCA is 0. Only detector resolution leads to finite values. For nonprompt D^0 from B feed down, as in shown

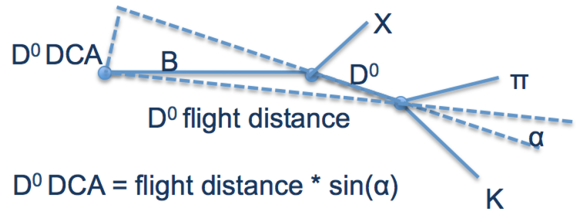

Figure 4.20.: Cartoon of nonprompt D^0 DCA

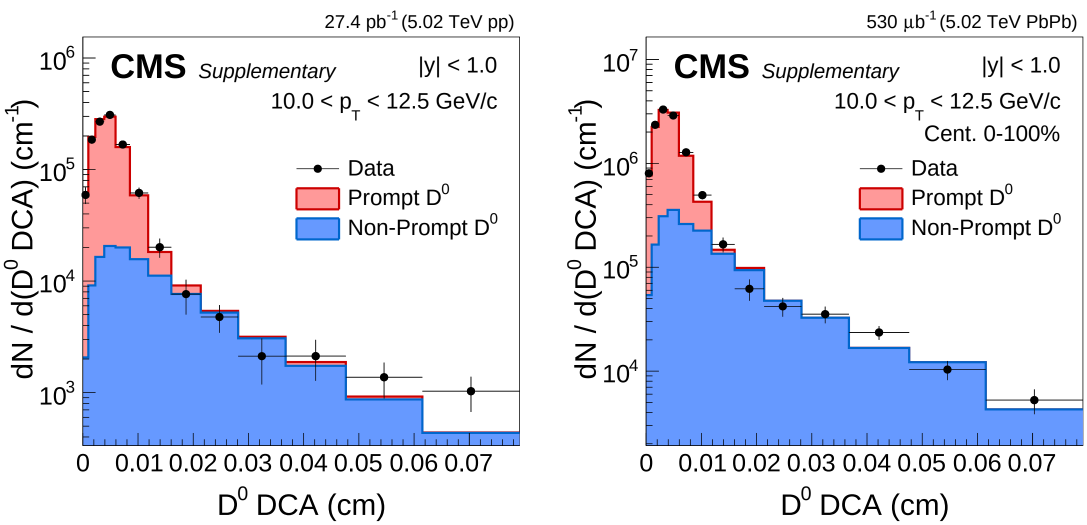

Figure 4.21.: Examples of fit on DCA distribution of D^0 signal from data (black marks) with templates of prompt (red histogram) and nonprompt (blue histogram) D^0 from simulations for pp collisions (left) and 0–100% centrality PbPb collisions (right) at 5.02 TeV.

in Fig. 4.20, the B decay leads to finite physics D^0 DCA. Therefore, the DCA distributions of prompt and nonprompt D^0 are different. A template fit on the DCA distribution of D^0 signal in data with the DCA shapes of prompt and nonprompt D^0 from the simulations can help extract the prompt D^0 fraction. In each p_{T} interval, the DCA distribution of D^0 signal in data is obtained through mass spectrum fit in bins of DCA or sideband substraction depending on the statistics. Figure 4.21 shows

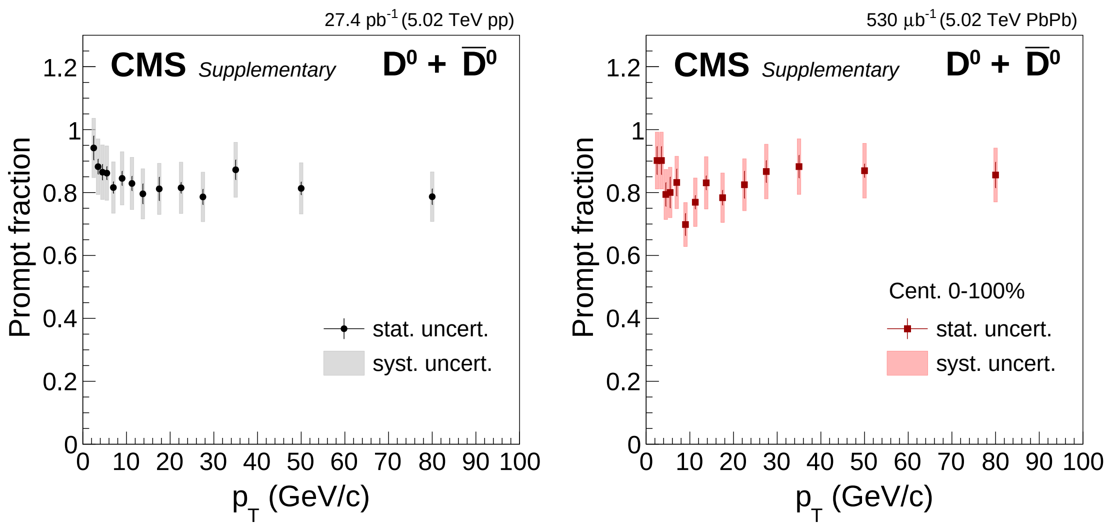

Figure 4.22.: Fractions of prompt D^0 as a function of p_{T} for pp collisions (left) and 0–100% centrality PbPb collisions (right) at 5.02 TeV.

examples of template fit on DCA distribution of D^0 signal for pp collisions (left) and 0–100% centrality PbPb collisions (right) at 5.02 TeV. Figure 4.22 shows the prompt D^0 fractions of as a function of p_{T} for pp collisions (left) and 0–100% centrality PbPb collisions (right) at 5.02 TeV. The prompt D^0 fractions are found to be 75–95%.

Besides, to validate the data driven procedure for the prompt fraction estimation, the results obtained are cross checked with the estimation based on the FONLL+MC based calculations as discussed in Section 4.1.4. The results are found to be consistent within uncertainties.

4.2.4 Results

The prompt D^0 p_{T}-differential cross section in each p_{T} interval in pp collisions is calculated as

$$\left.\frac{d\sigma_{pp}}{dp_{\mathrm{T}}}\right|_{|y|<1} = \frac{1}{2}\frac{1}{\Delta p_{\mathrm{T}}}\frac{1}{\mathcal{L}\,\mathcal{B}}\left.\frac{f_{\mathrm{prompt}}\,N_{pp}}{(\alpha\times\epsilon)_{\mathrm{prompt}}\,\epsilon_{\mathrm{trigger}}}\right|_{|y|<1}, \tag{4.7}$$

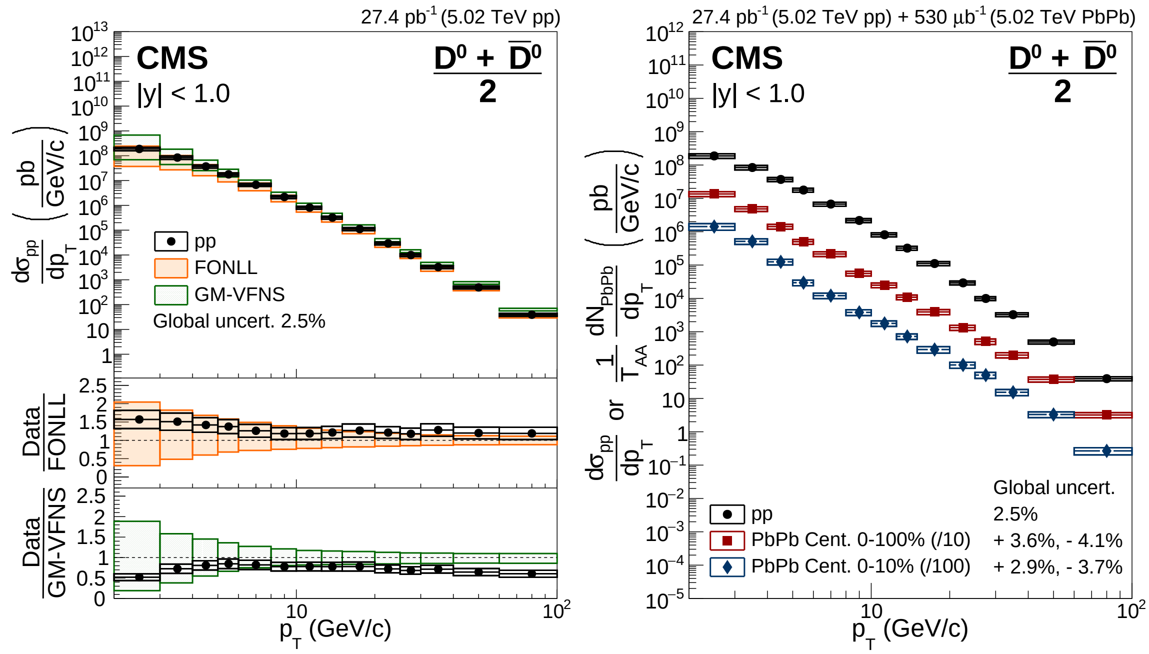

Figure 4.23.: (left) The prompt D^0 p_T-differential cross section in pp collisions at $\sqrt{s} = 5.02$ TeV. The vertical bars (boxes) correspond to statistical (systematic) uncertainties. The global systematic uncertainty, listed in the legend and not included in the point-to-point uncertainties, comprises the uncertainties in the integrated luminosity measurement and the D^0 meson $\mathcal{B}$. Results are compared to FONLL [95] and GM-VFNS [104–106] calculations. (right) The prompt D^0 p_T-differential production yields divided by the nuclear overlap functions T_AA for PbPb collisions in the 0–100% (red) and 0–10% (blue) centrality ranges compared to the same pp cross sections shown in the left panel (black).

where Δp_T is the width of the p_T interval, $\mathcal{L}$ is the integrated luminosity, $\mathcal{B}$ is the branching fraction of the $D^0 \rightarrow K^- \ \pi^+$ channel, $(\alpha \times \epsilon)_\mathrm{prompt}$ is the prompt D^0 acceptance and efficiency, f_prompt is the fraction of prompt D^0, $\epsilon_\mathrm{trigger}$ is the D^0 trigger efficiency (for minimum bias trigger, it is 1), and N_{pp} is the raw yield of D^0 signal in each p_T interval. The factor 1/2 accounts for the fact that N_{pp} is the total yield of D^0 and $\overline{D}^0$. The measured prompt D^0 p_T-differential cross section in pp collisions at 5.02 TeV is presented in the left panel of Fig. 4.23. The calculations from FONLL and a general-mass variable flavour number scheme (GM-VFNS) [104–106] are plotted for comparison. It is found that the measured results are close to the upper bound of the FONLL calculation and the lower bound of the GM-VFNS calculation.

The prompt D^0 p_{T}-differential production yield in each p_{T} interval in PbPb collisions normalized by T_{AA} is calculated as:

$$\frac{1}{T_{\mathrm{AA}}} \frac{dN_{PbPb}}{dp_{\mathrm{T}}}\bigg|_{|y|<1} = \frac{1}{T_{\mathrm{AA}}} \frac{1}{2} \frac{1}{\Delta p_{\mathrm{T}}} \frac{1}{N_{\mathrm{MB}}\,\mathcal{B}} \frac{f_{\mathrm{prompt}}\,N_{PbPb}}{(\alpha \times \epsilon)_{\mathrm{prompt}}\;\;\epsilon_{\mathrm{trigger}}}\bigg|_{|y|<1}, \tag{4.8}$$

where N_{MB} is the number of MB events used for the analysis and T_{AA} is the nuclear overlap function [27]. The values of T_{AA} are $5.61\mathrm{mb}^{-1}$ for inclusive PbPb collisions and $23.2\mathrm{mb}^{-1}$ for central events [42]. The other terms were defined in analogy with Eq. (4.7). The prompt D^0 p_{T}-differential production yields divided by the nuclear overlap functions T_{AA} in PbPb collisions for centrality classes 0–100% and 0–10% are presented in the right panel of Fig. 4.23 and pp cross section shown in the left panel is plotted for comparison.

The R_{AA} for the centrality class 0–100% is presented in the left panel of Fig. 4.24. It is found that the prompt D^0 production is suppressed by a factor of 3 to 4 in the p_{T} range 6–8 GeV/c. The suppression factor decreases towards higher p_{T} range. The R_{AA} for the centrality class 0–10% is shown in the right panel of Fig. 4.24, which shows similar p_{T} dependence to the R_{AA} for the centrality class 0–100%.

The measured prompt D^0 R_{AA} results are also compared to calculations of different models: M. Djordjevic [107] and CUJET 3.0 [108–110], which are two pQCD-based models including both collisional and radiative energy loss, I. Vitev [111, 112], which is a pQCD-based model including radiative energy loss only, S. Cao *et al.* [113, 114], which is a transport model based on a Langevin equation and includes both collisional and radiative energy loss, PHSD [115, 116], which is a microscopic off-shell transport model based on a Boltzmann approach and includes collisional energy loss only, AdS/CFT [117], which is a model based on the anti-de Sitter/conformal field theory (AdS/CFT) correspondence and includes thermal fluctuations in the energy loss for heavy quarks. For AdS/CFT calculations, two settings of the diffusion coefficient of the heavy quark propagation through the medium (dependent on, and independent of the quark momentum) are provided. In the range of $p_{\mathrm{T}} > 40$ GeV/c, the calculations from M. Djordjevic, CUJET 3.0 and I. Vitev are consistent with the measured results in both centrality ranges within the uncertainties, though the calculated central values tend to be lower than the experimental results. The calculations from S. Cao *et al.* can generally descirbe the measurement well in the centrality range 0–100%, while it overestimate the suppression for the central events. The calculations from AdS/CFT are consistent with the measured results in both centrality ranges. In the p_{T} range of 10–40 GeV, all models describe well the measured results in both centrality ranges. For $p_{\mathrm{T}} < 10$ GeV/c, the calculations from PHSD with shadowing are consistent with the measured results in the centrality range 0-100%, while the calculations from S. Cao *et al.* overestimate the suppression and the calculations from AdS/CFT lie at the lower bound of the the experimental uncertainties for both centrality ranges.

The prompt D^0 R_{AA} is compared to the measurements of the R_{AA} of charged particles [42], $B^{\pm}$ mesons [118] and nonprompt J/ψ meson [119] preformed at the same energy and in the same centrality range 0–100% in the left panel of Fig. 4.25. For $p_{\mathrm{T}} > 5$GeV/c, The D^0 meson R_{AA} is consistent with that of charged particles, while the D^0 meson R_{AA} tends to be higher than that of charged particles for $p_{\mathrm{T}} < 5$GeV/c. The $B^{\pm}$ meson R_{AA}, which is measured in the p_{T} range of 7–50 GeV/c and the rapidity range of $|y| < 2.4$, is found to be consistent with the D^0 results within uncertainties. The nonprompt J/ψ meson R_{AA} is higher than the D^0 meson R_{AA} in the measured p_{T} range. Right panel of Fig. 4.25 shows the comparison between the R_{AA} of D^0 meson and charged particles in the centrality range 0–10%, which shows similar trend as in the centrality range 0–100%.

In summary, the p_{T}-differential cross sections of prompt D^0 mesons in pp and PbPb collisions at 5.02 TeV, and the R_{AA} in PbPb collisions at 5.02 TeV are measured in the p_{T} range of 2–100 GeV/c at midrapidity ($|y| < 1.0$) with the CMS detector. It is found that the production of prompt D^0 mesons is strongly supressed in PbPb

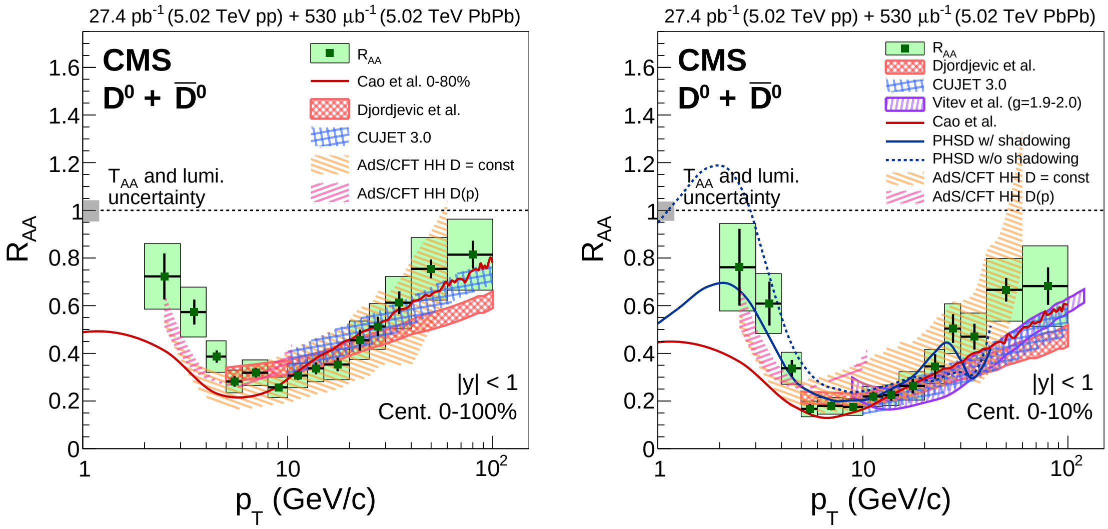

Figure 4.24.: R_{AA} as a function of p_{T} in the centrality range 0–100% (left) and 0–10% (right). The vertical bars (boxes) correspond to statistical (systematic) uncertainties. The global systematic uncertainty, represented as a grey box at $R_{\mathrm{AA}} = 1$, comprises the uncertainties in the integrated luminosity measurement and T_{AA} value. The D^0 R_{AA} values are also compared to calculations from various theoretical models [107–117].

collisions. The D^0 R_{AA} is found to be consistent with the charged particle R_{AA} for $p_{\mathrm{T}} > 5$ GeV/c, while tend to be higher for $p_{\mathrm{T}} < 5$ GeV/c. The D^0 R_{AA} is consistent with the $B^{\pm}$ R_{AA}, while lower than nonprompt J/ψ R_{AA}. The D^0 meson R_{AA} is also compared with calculations from different theoretical models and provides important inputs to the theoretical studies.

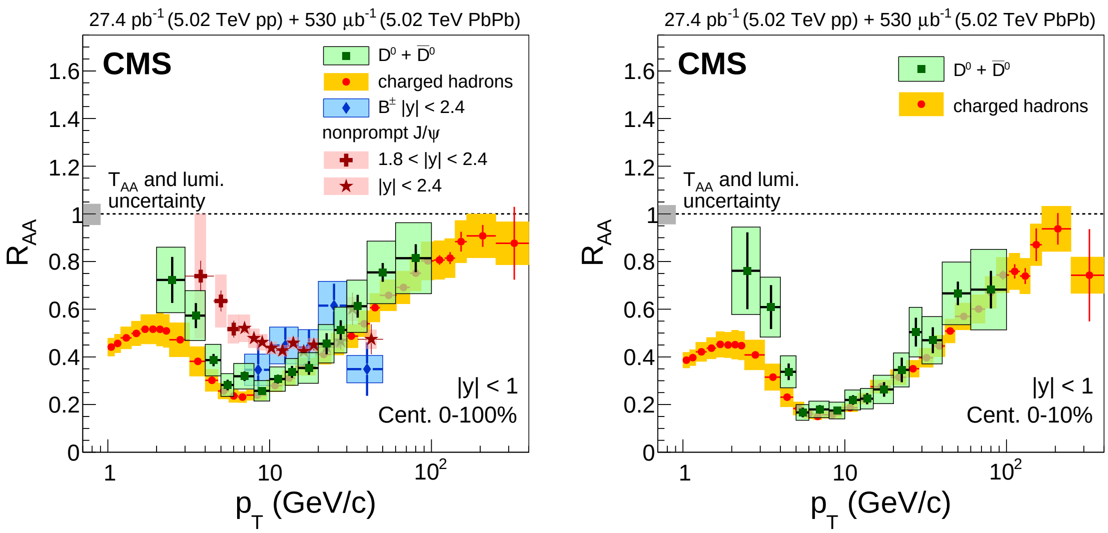

Figure 4.25.: (left) Nuclear modification factor R_{AA} as a function of p_{T} in the centrality range 0–100% (green squares) compared to the R_{AA} of charged particles (red circles) [42], $B^{\pm}$ mesons (blue triangles) [118] and nonprompt J/ψ meson (purple crosses and stars) [119] in the same centrality range at 5.02 TeV. (right) Nuclear modification factor R_{AA} as a function of p_{T} in the centrality range 0–10% (green squares) compared to the R_{AA} of charged particles (red circles) [42] in the same centrality range.

5. Prompt D^0 Azimuthal Anisotropy in PbPb Collisions

This chapter presents the details of the measurement of the prompt D^0 azimuthal anisotropy in PbPb Collisions at 5.02 TeV.

5.1 Datasets and Monte Carlo Simulation

The data used in this analysis is the PbPb data at 5.02 TeV collected by the CMS detector in 2015. The data selected by a minimum bias trigger and a 30–100% centrality trigger is used. The minimum bias trigger was prescaled by a larger factor than the centrality trigger during data taking. The 30–100% centrality trigger is to enhance the statistics in centrality 30–50% analysis. The event selections applied in offline analysis is the same with the D^0 meson R_{AA} analysis at 5.02 TeV discussed in Section 4.2.1. The numbers of events used in this analysis for the centrality classes 0–10%, 10–30%, and 30–50% are 32 million, 64 million and 151 million, respectively.

The Monte Carlo samples used in the R_{AA} analysis at 5.02 TeV analysis discussed in Section 4.2.1 are used in this analysis.

5.2 D^0 Candidate Selection

As discussed in Section 3.1, apart from the selections on $d_0/\sigma(d_0)$, α, and vertex probability, the selection DCA < 0.008 cm is applied in this analysis to suppress the nonprompt D^0 in data. Figure 5.1 shows the DCA < 0.008 cm selection efficiency for prompt and nonprompt D^0 after other analysis selections are applied. It shows the efficiency for prompt D^0 is 80–98% while the efficiency for nonprompt D^0 is 35–50%, which means the DCA < 0.008 cm selection can reduce the nonprompt D^0 fraction by around 50%. This property is utilized in the evaluation of systematic uncertainty from nonprompt D^0 discuss in Section 5.4.

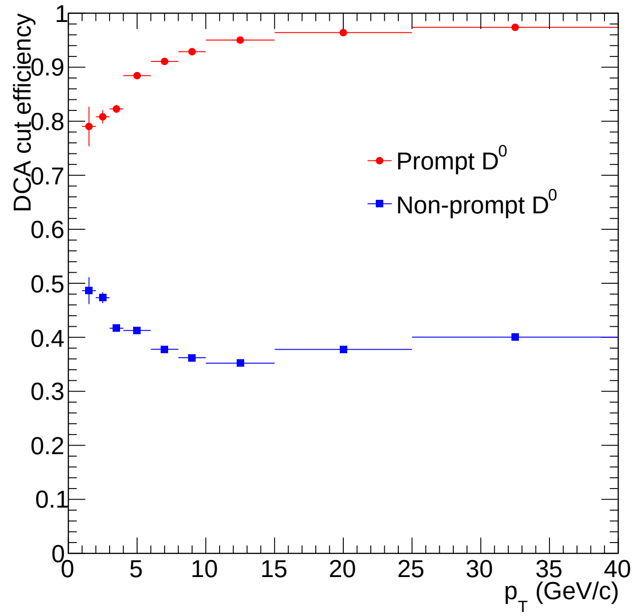

Figure 5.1.: DCA $<$ 0.008 cm selection efficiency for prompt and nonprompt D^0 after other analysis selections are applied.

5.3 Analysis Techniques

This section discusses the techniques used in thie analysis to extract the D^0 v_n coefficient.

5.3.1 EP and SP Method

With the event plane, the anisotropy coefficient v_n can be measured with event plane method (EP method) and scalar product method (SP method).

The event plane angle Ψ_n can be expressed with Q-vectors. The Q-vector of event plane is defined as:

$$Q_n = \sum_{k=1}^{M} \omega_k e^{in\phi_k}, \tag{5.1}$$

where M represents the subevent multiplicity, ϕ_k is the azimuthal angle of the kth particle, and ω_k is a weighting factor.

The Q-vector of each D^0 candidate, Q_{n,D^0}, is defined as:

$$Q_{n,D^0} = e^{in\phi}, \tag{5.2}$$

where ϕ is the azimuthal angle of the D^0 candidate.

With the EP method, the v_n is calculated with Q-vectors as:

$$v_n\{\mathrm{EP}\} \equiv \frac{\left\langle Q_{n,D^0} \frac{Q_{nA}^*}{|Q_{nA}|} \right\rangle}{\sqrt{\frac{\left\langle \frac{Q_{nA}}{|Q_{nA}|} \frac{Q_{nB}^*}{|Q_{nB}|} \right\rangle \left\langle \frac{Q_{nA}}{|Q_{nA}|} \frac{Q_{nC}^*}{|Q_{nC}|} \right\rangle}{\left\langle \frac{Q_{nB}}{|Q_{nB}|} \frac{Q_{nC}^*}{|Q_{nC}|} \right\rangle}}}, \tag{5.3}$$

where the denominator on the right is defined as the event plane resolution R_n.

With the SP method, the v_n is calculated with Q-vectors as:

$$v_n\{\mathrm{SP}\} = \frac{\langle Q_{n,D^0} Q_{nA}^* \rangle}{\sqrt{\frac{\langle Q_{nA} Q_{nB}^* \rangle \langle Q_{nA} Q_{nC}^* \rangle}{\langle Q_{nB} Q_{nC}^* \rangle}}}, \tag{5.4}$$

In this analysis, the subscript A and B refer to event planes defined using calorimeter data, with the HF_n^- planes covering the pseudorapidity range of $-5 < \eta < -3$ and HF_n^+ planes covering the range $3 < \eta < 5$, respectively. The subscript C refers to event plane defined with tracker data with $-0.75 < \eta < 0.75$. The denominator of Eq. (5.4) and (5.3) effectively correct for the finite resolution of the A event plane that results from finite particle multiplicities and detector effects. The averages $\langle Q_{nA} Q_{nB}^* \rangle$, $\langle Q_{nA} Q_{nC}^* \rangle$ and $\langle Q_{nB} Q_{nC}^* \rangle$ are taken over all events, while the average $\langle Q_n, D^0 Q_{nA}^* \rangle$ is over all D^0 candidates in all events. The real part is taken for all averages of Q-vector products. To avoid the nonflow effects, the η gap between D^0 candidates and the correlated event plane A is required to be at least 3 units. Thus

HF_n^- planes are used as event plane A and HF_n^+ planes are used as event plane B for D^0 candidates from the positive η region, and vice versa.

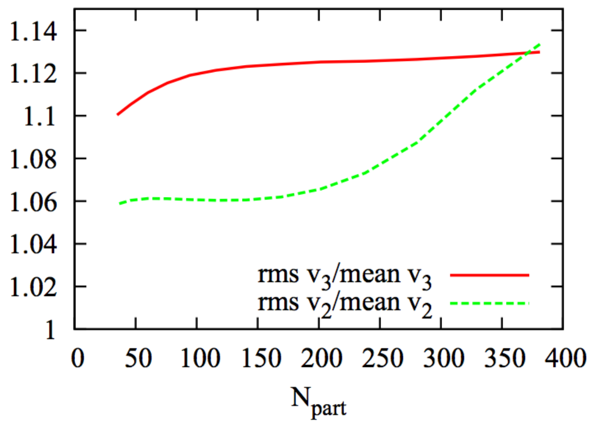

Figure 5.2.: Ratios of RMS to mean values of elliptic and triangular flow for PbPb collisions at 2.76 TeV. The results assume the flow coefficients are proportional to the corresponding Glauber model eccentricities. This figure is copied from Ref. [120].

Luzum and Ollitrault have argued that it would be better to present experimental results using the SP method than using the EP method [120]. The argument is that that the results of the event plane method depend on the value of the event plane resolution, with

$$v_n\{\text{EP}\} \underset{\text{highres.}}{\xrightarrow{M}} \langle v_n \rangle \tag{5.5}$$

and

$$v_n\{\text{EP}\} \underset{\text{lowres.}}{\xrightarrow{M}} \sqrt{\langle v_n^2 \rangle}. \tag{5.6}$$

With the scalar product method one has

$$v_n\{\text{SP}\} \equiv \sqrt{\langle v_n^2 \rangle}. \tag{5.7}$$

Figure 5.2, copied from Ref. [120], illustrates how the mean and RMS values are expected to differ for PbPb collisions at 2.76 TeV. Thus in this analysis, the SP method is used as the default analysis method, while the $\Delta\phi$ bins method, which is derived from the EP method, is used as a cross check.

5.3.2 Extraction of D^0 Signal v_n

After v_n of each D^0 candidate is calculated with Eq. (5.4), to extract v_n of D^0 signal (v_n^S), a simultaneous fit on mass spectrum and v_n as function of invariant mass is performed. As discussed in Section 3.3, the mass spectrum fit function is composed of $B(m_{inv})$ for combinatorial background, $S(m_{inv})$ for D^0 signal, and $SW(m_{inv})$ for D^0 candidates with incorrect mass assignment. The average v_n of all D^0 candidtes as a function of invariant mass, $v_n^{S+B}(m_{inv})$, is fitted with

$$v_n^{S+B}(m_{inv}) = \alpha(m_{inv})v_n^S + (1 - \alpha(m_{inv}))v_n^B(m_{inv}), \tag{5.8}$$

where

$$\alpha(m_{inv}) = (S(m_{inv}) + SW(m_{inv}))/(S(m_{inv}) + SW(m_{inv}) + B(m_{inv})). \tag{5.9}$$

Here, $v_n^B(m_{inv})$ is the v_n of background D^0 candidates and is modeled as a linear function of invariant mass, while $\alpha(m_{inv})$ is the D^0 signal fraction as a function of invariant mass, which is from mass spectrum fit function. The K-π swapped compontent is inlcuded in signal fraction because these candidates are from real D^0 and should have same v_n value with real D^0 signal. The left panel of Fig. 5.3 shows an example of a simultaneous fit to the mass spectrum and $v_2^{S+B}(m_{\rm inv})$ in the $p_{\rm T}$ interval 4–5 GeV/c for the centrality class 10–30%. The right panel of Fig. 5.3 shows an example of a simultaneous fit to the mass spectrum and $v_3^{S+B}(m_{\rm inv})$ in the $p_{\rm T}$ interval 5–6 GeV/c for the centrality class 30–50%.

The D^0 signal in data is a mixture of prompt and nonprompt D^0, thus the measured v_n^S above is also a combination of v_n of prompt and nonprompt D^0, expressed as

$$v_n^S = f_{prompt}v_n^{prompt} + (1 - f_{prompt})v_n^{nonprompt}. \tag{5.10}$$

In Eq. (5.10), v_n^{prompt} and $v_n^{nonprompt}$ is the v_n of prompt and nonprompt D^0 respectively, and f_{prompt} is fraction of prompt D^0 in data. To extract the v_n of prompt D^0, the v_n of D^0 from data without the DCA < 0.008 cm selection is also measured

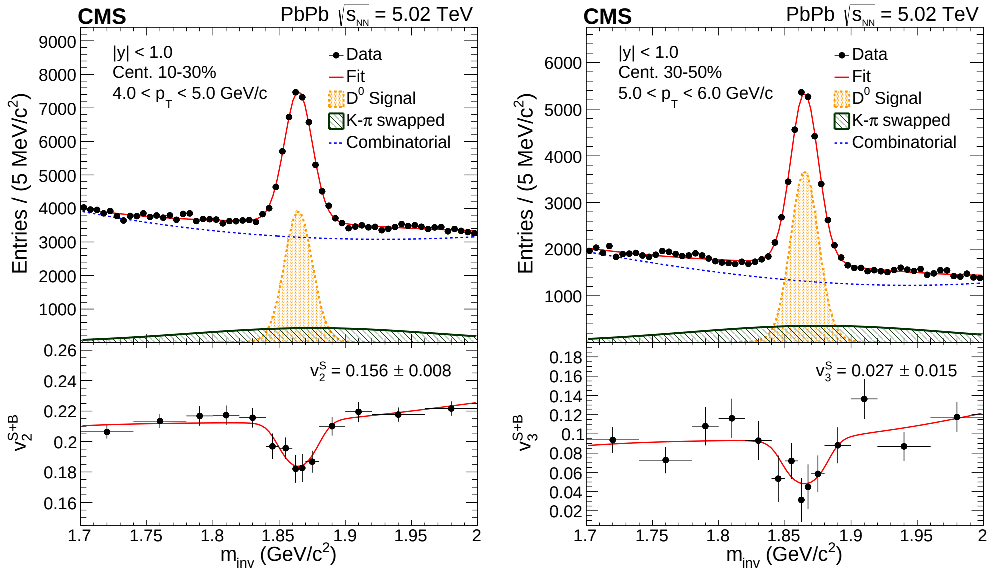

Figure 5.3.: Left: example of simultaneous fit to the invariant mass spectrum and $v_2^{S+B}(m_{\mathrm{inv}})$ in the p_{T} interval 4–5 GeV/c for the centrality class 10–30%. Right: example of simultaneous fit to the invariant mass spectrum and $v_3^{S+B}(m_{\mathrm{inv}})$ in the p_{T} interval 5–6 GeV/c for the centrality class 30–50%.

besides the results with all analysis selections. With some calculations, v_n^{prompt} can be expressed as

$$v_n^{prompt} = v_{n,1}^S + \frac{1 - f_{prompt,1}}{f_{prompt,1} - f_{prompt,2}}(v_{n,1}^S - v_{n,2}^S), \tag{5.11}$$

where subscripts 1 and 2 refer to with and without DCA < 0.008 cm selection, respectively. The v_n of D^0 from data with all analysis selections, $v_{n,1}^S$, is kept as central values in this analysis while the second term,

$$\frac{1 - f_{prompt,1}}{f_{prompt,1} - f_{prompt,2}}(v_{n,1}^S - v_{n,2}^S),$$

is assigned as systematic uncertainty due to nonprompt D^0. The detail study on systematic uncertainty from remaining nonprompt D^0 is discussed in Section 5.4.

5.3.3 $\Delta\phi$ Bins Method

The azimuthal dependence of the particle yield can be written in terms of an harmonic expansion with [47]:

$$E\frac{d^3N}{d^3p} = \frac{1}{2\pi}\frac{d^2N}{p_T dp_T dy}\left(1 + \sum_{n=1}^{\infty} 2v_n \cos\left[n\left(\phi - \Psi\right)\right]\right), \tag{5.12}$$

where ϕ, E and p_T are the particle's azimuthal angle, energy, and transverse momentum, respectively. Therefore, another method to measure the D^0 v_n is to divide the D^0 candidates into several $\Delta\phi$ bins and use the raw D^0 yield in each $\Delta\phi$ bin.

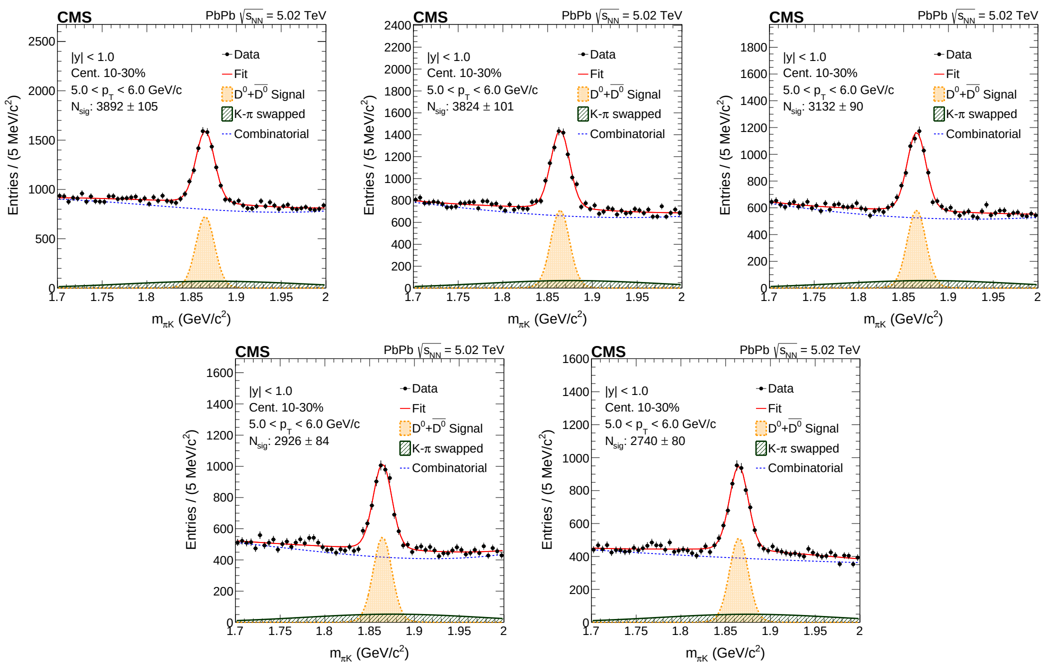

Figure 5.4.: D^0 mass spectrum fit in different $\Delta\phi$ bins for v_2 in p_{T} interval 5.0–6.0 GeV/c and centrality 10–30%

Figure 5.4 shows an example of mass spectrum fit for v_2 in p_{T} interval 5.0–6.0 GeV/c and centrality 10–30%. Then v_n^{obs} can be extracted with a fit on the $d^2N/(dp_{\mathrm{T}}d\Delta\phi)$ distribution using Eq. (5.13), where N_0 and v_n^{obs} are free parameters.

$$N_0 + 2v_n^{obs}cos(n\Delta\phi) \tag{5.13}$$

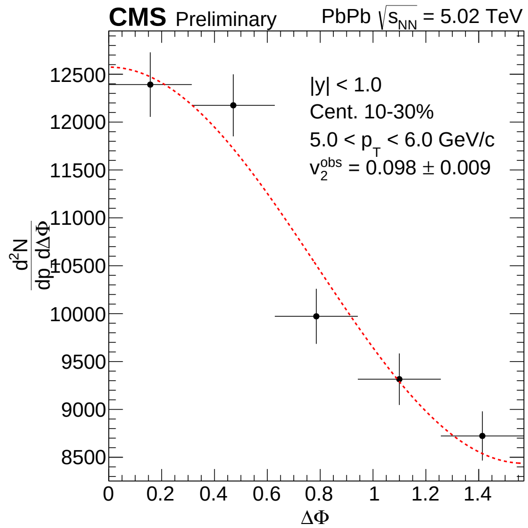

Figure 5.5.: $d^2N/(dp_\mathrm{T}d\Delta\phi)$ fit for v_2 in p_T interval 5.0–6.0 GeV/c and centrality 10–30%.

The D^0 v_n is v_n^{obs} corrected by event plane resolution R_n, given as

$$v_n = \frac{v_n^{obs}}{R_n}. \tag{5.14}$$

Figure 5.5 shows $d^2N/(dp_\mathrm{T}d\Delta\phi)$ fit for v_2 in p_T interval 5.0–6.0 GeV/c and centrality 10–30%. The v_n^{obs} values are shown in the figures.

5.4 Systematic Uncertainties

This section presents the studies of systematic uncertainties for both the SP method and the $\Delta\phi$ bins method. The systematic sources include remaining non-prompt D^0 as discussed in Section 5.3.2, the background mass PDF, the track selection, the D^0 meson yield correction (acceptance and efficiency) and the background v_n PDF. Because the D^0 v_n values are pretty close to zero, especially in the high p_{T} range, absolute uncertainties are assigned in this analysis. The systematic uncertainty studies are discussed in detail below:

- Systematic uncertainty from the remaining nonprompt D^0

  As discussed in Section 5.3.2, the second term of Equation 5.11,

$$\frac{1 - f_{prompt,1}}{f_{prompt,1} - f_{prompt,2}}(v_{n,1}^{sig} - v_{n,2}^{sig}),$$

  is taken as systematic uncertainties from non-prompt D^0, where subscript 1 and 2 refer to with and without DCA < 0.008 cm selection, respectively.

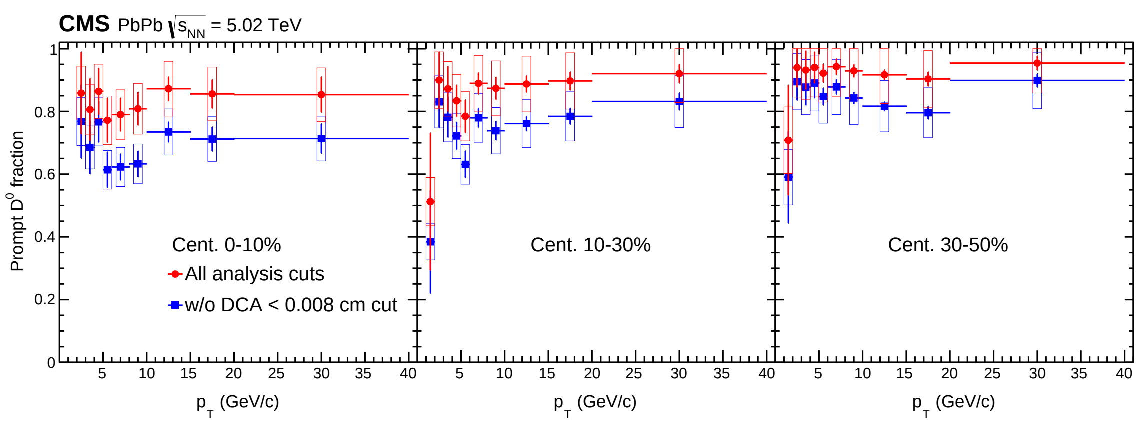

Figure 5.6.: Prompt D^0 fraction with (red) and without (blue) DCA < 0.008 cm selection for centrality classes 0-10%, 10-30%, and 30-50%.

In this analysis, the prompt D^0 fraction f_{prompt} is evaluated from the template fit to the DCA distribution of D^0 signal in data as discussed in Section 4.2.3.

The discrimination between prompt and nonprompt D^0 mesons lies mainly in the large DCA region, thus the fit is performed on the entire range without the DCA $<$ 0.008 cm selection, where both $f_{prompt,1}$ and $f_{prompt,2}$ are evaluated. Figure 5.6 shows the prompt D^0 fraction with (red) and without (blue) DCA $<$ 0.008 cm selection. We can see the nonprompt D^0 fraction is suppressed by around 50% with the DCA selection. In the procedure of evaluating $\frac{1-f_{prompt,1}}{f_{prompt,1}-f_{prompt,2}}$, the statistical and systematic uncertainties of $f_{prompt,1}$ and $f_{prompt,2}$ are considered. The uncertainties of $f_{prompt,1}$ and $f_{prompt,2}$ are strongle correlated, thus we take $f_{prompt,1}$ and $f_{prompt,2}$ minimum or maximum values at the same time.

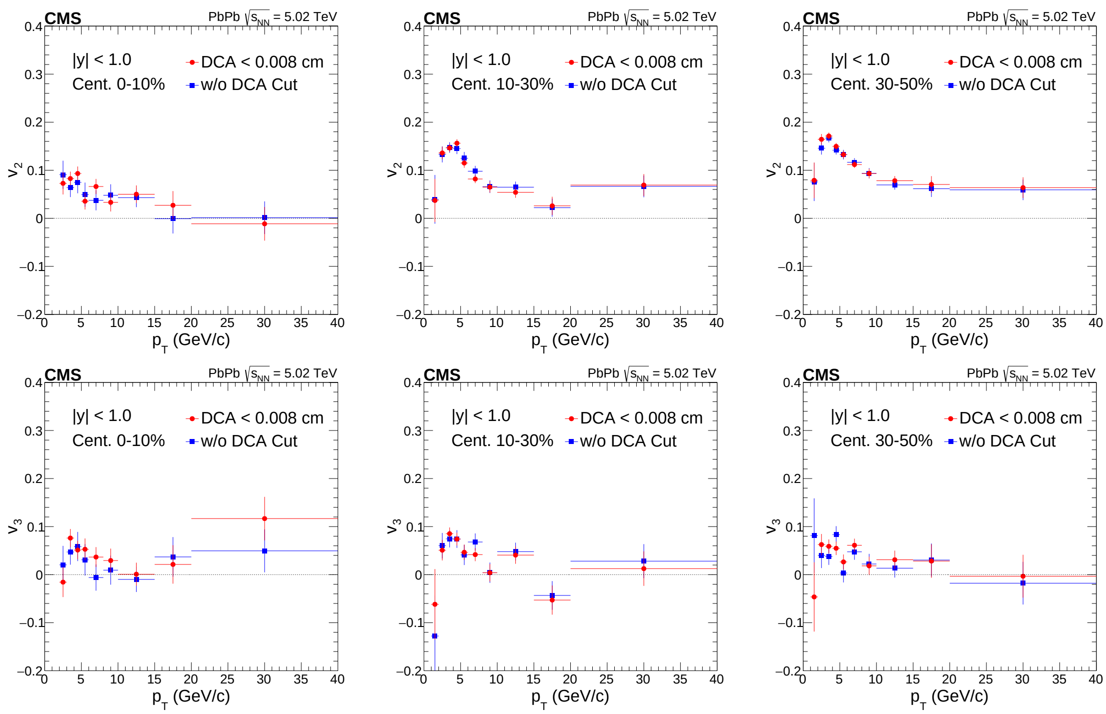

Figure 5.7.: D^0 signal v_2 (upper) and v_3 (lower) with (red) and without (blue) DCA $<$ 0.008 cm selection for centrality classes 0-10%, 10-30%, and 30-50%.

Figure 5.7 shows the D^0 signal v_2 (upper) and v_3 (lower) with (red) and without (blue) DCA $<$ 0.008 cm selection for centrality classes 0-10%, 10-30%, and 30-50%. We can see that the differences between v_n values with and without the

DCA selection are actually small. With the information in Figs. 5.6 and 5.7, we are able to calculate the

$$\frac{1 - f_{prompt,1}}{f_{prompt,1} - f_{prompt,2}}(v_{n,1}^{sig} - v_{n,2}^{sig}).$$

One problem in this procedure is that the calculated $v_{n,1}^{sig} - v_{n,2}^{sig}$ values not only include the effect from nonprompt D^0 fraction change, but may also be affected by uncertainties form other sources, such as statistical fluctuations. In this case, the systematic uncertainty from nonprompt D^0 may be overestimated. To minimize the effects from other uncertainties, the systematic uncertainty from nonprompt D^0 is evaluated in wide p_{T} intervals 1-2 GeV/c, 2-8 GeV/c, and 8-40 GeV/c.

- Systematic uncertainty from the background mass PDF

  The background mass PDF is varied to a 2nd order polynomial and a exponential function, then the extracted v_n values are compared with the default values.

- Systematic uncertainty from the track selection

  The track selections applied in D^0 reconstruction are varied and the effect on v_n results is studied.

- Systematic uncertainty from the D^0 meson yield correction

  Both D^0 yield correction factor (acceptance and efficiency) and v_n are functions of p_{T}. In the v_n ananlysis, there may be be systematic uncertainties from D^0 correction factor. To evaluate the uncertainty from efficiency, each D^0 candidate is corrected by the correction factor, then v_n values are extracted with the corrected distributions and compared with the default values.

- Systematic uncertainty from the background v_n PDF

  The background v_n PDF is changed to a 2nd order polynomial in the v_n vs mass fit and the extracted v_n values are compared with the default values.

Tables 5.1 and 5.2 show summary of systematic uncertainties for v_2 and v_3, respectively.

Centrality and Source	Invariant mass (SP) method				$\Delta\phi$ bins method			
	1-2GeV/c	2-8	8-20	20-40	1-2	2-8	8-20	20-40
Centrality 0-10%								
Bkg mass PDF variation	-	0.001	0.001	0.001	-	0.005	0.005	0.005
Efficiency correction	-	0.003	0.003	0.005	-	0.005	0.005	0.005
Track cuts variation	-	0.01	0.02	0.02	-	0.02	0.02	0.02
Bkg v_n PDF	-	0.01	0.005	0.02	-	-	-	-
Non-prompt D^0	-	0.02	0.01	0.01	-	0.02	0.01	0.01
Centrality 10-30%								
Bkg mass PDF variation	0.001	0.001	0.001	0.001	0.005	0.005	0.005	0.005
Efficiency correction	0.002	0.002	0.002	0.002	0.01	0.01	0.005	0.005
Track cuts variation	0.005	0.005	0.005	0.02	0.02	0.01	0.01	0.01
Bkg v_n PDF	0.03	0.005	0.001	0.001	-	-	-	-
Non-prompt D^0	0.03	0.01	0.01	0.01	0.03	0.01	0.01	0.01
Centrality 30-50%								
Bkg mass PDF variation	0.001	0.001	0.001	0.001	0.015	0.005	0.005	0.005
Efficiency correction	0.003	0.003	0.003	0.003	0.005	0.005	0.005	0.005
Track cuts variation	0.01	0.01	0.01	0.01	0.025	0.01	0.01	0.01
Bkg v_n PDF	0.06	0.006	0.006	0.006	-	-	-	-
Non-prompt D^0	0.03	0.01	0.01	0.01	0.03	0.01	0.01	0.01

Table 5.1.: Summary of systematic uncertainties for D^0 v_2 in PbPb collisions at 5.02 TeV.

5.5 Cross Checks

In this section, some cross checks on the analysis are presented.

Centrality and Source	Invariant mass (SP) method				$\Delta\phi$ bins method			
	1-2GeV/c	2-8	8-20	20-40	1-2	2-8	8-20	20-40
Centrality 0-10%								
Bkg mass PDF variation	-	0.001	0.001	0.001	-	0.005	0.002	0.002
Efficiency correction	-	0.005	0.005	0.005	-	0.01	0.01	0.005
Track cuts variation	-	0.02	0.02	0.02	-	0.01	0.03	0.03
Bkg v_n PDF	-	0.01	0.01	0.01	-	-	-	-
Non-prompt D^0	-	0.02	0.02	0.02	-	0.02	0.02	0.02
Centrality 10-30%								
Bkg mass PDF variation	0.001	0.001	0.001	0.001	0.01	0.002	0.01	0.01
Efficiency correction	0.004	0.004	0.004	0.004	0.005	0.005	0.005	0.005
Track cuts variation	0.015	0.015	0.015	0.015	0.01	0.01	0.02	0.02
Bkg v_n PDF	0.005	0.005	0.015	0.02	-	-	-	-
Non-prompt D^0	0.05	0.01	0.01	0.01	0.05	0.01	0.01	0.01
Centrality 30-50%								
Bkg mass PDF variation	0.001	0.001	0.001	0.001	0.005	0.005	0.005	0.005
Efficiency correction	0.004	0.004	0.004	0.004	0.01	0.01	0.005	0.005
Track cuts variation	0.01	0.01	0.01	0.005	0.04	0.01	0.015	0.02
Bkg v_n PDF	0.01	0.01	0.015	0.01	-	-	-	-
Non-prompt D^0	0.05	0.02	0.01	0.01	0.05	0.02	0.01	0.01

Table 5.2.: Summary of systematic uncertainties for D^0 v_3 in PbPb collisions at 5.02 TeV.

5.5.1 η Gap Study

As discussed in Section 5.3.1, the η gap between D^0 candidates and correlated event plane A is required to be at least 3 units to avoid nonflow effects. However, there may be still residual nonflow effects. The evaluate the remaining nonflow effect, the η gap between D^0 candidates and correlated event plane A is varied to see if there is clear trend on the v_n values while the η gap changes. This study was performed by defining a number of new event planes covering different η ranges using the ECAL and HCAL detectors in addition for the HF detectors.

Figure 5.8 shows v_2 with different η gaps between D^0 candidates and correlatd event plane A for centrality 0-10% (left), 10-30% (middle) and 30-50% (right). No clear ordering on v_2 results with different η gaps are observed with current uncertainties, so no clear non-flow effects are observed and no systematic uncertainties from non-flow effects are assigned in the analysis. Figure 5.9 shows same plots for v_3 and no clear non-flow effects are observed.

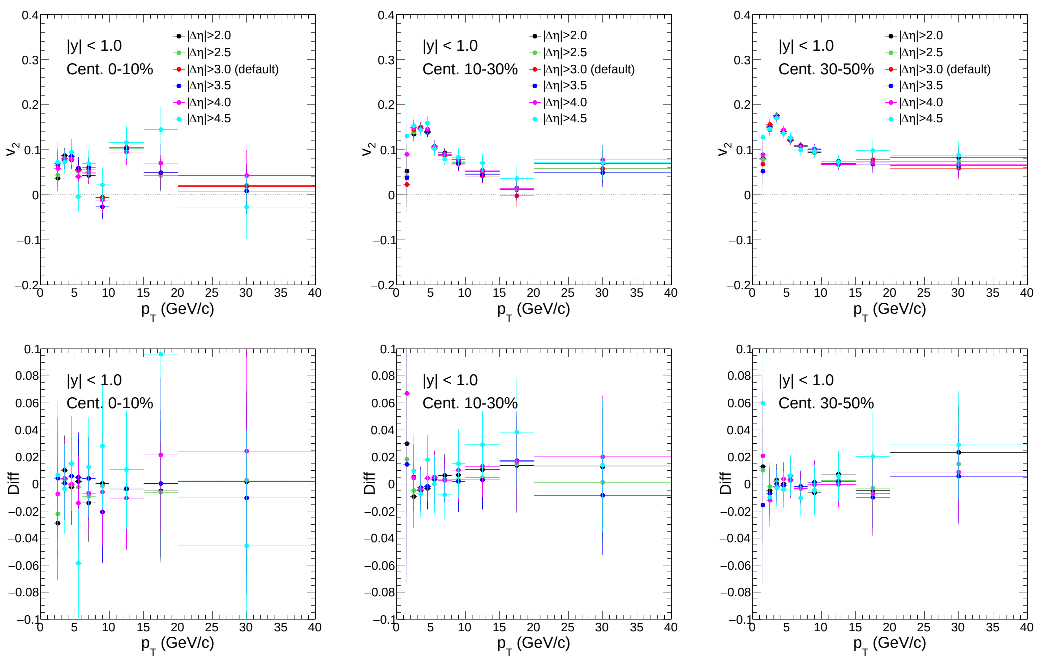

Figure 5.8.: v_2 results with different η gaps between D^0 candidates and correlatd event plane A for centrality 0-10% (left), 10-30% (middle) and 30-50% (right). Lower panels show absolute differences from default.

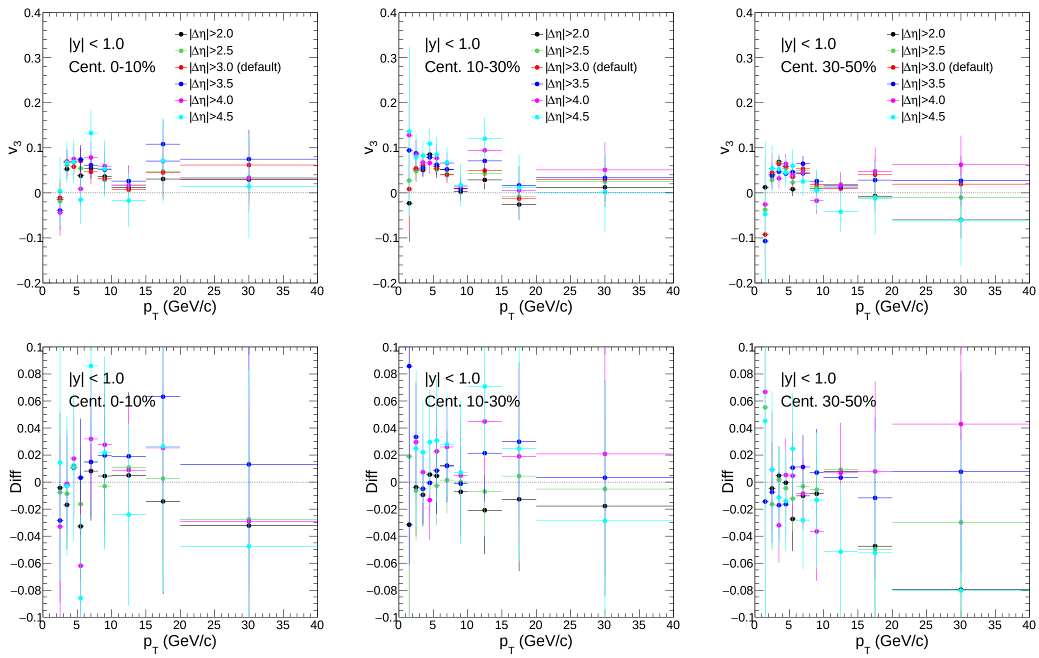

Figure 5.9.: v_3 results with different η gaps between D^0 candidates and correlatd event plane A for centrality 0-10% (left), 10-30% (middle) and 30-50% (right). Lower panels show absolute differences from default.

5.5.2 Check on the Statistical Uncertainty of v_n Results from Simultaneous Fit

This check is done to make sure that the statistical uncertainty of D^0 v_n results from the simultaneous fit discussed in Section 5.3.2 is correct. The study is done by randomly dividing the data into 8 subsets and the D^0 v_n are measured for each subset. Then the pull distributions of v_n results in the 8 subsets are calculated and fitted with Gaussian function. If the σ of the fitted Gaussian function is close to unity, the statistical errors of v_n results are correct. Figure 5.10 show v_2 (lower) and v_3 (upper) from all data (solid points) and 8 randomly divided subsets (empty points). Figure 5.11 shows pull distributions for v_2 (left) and v_3 (right). The distributions are fitted with Gaussian functions (read lines). The σ of fitted Gaussian functions, 1.04 ± 0.06 and 0.96 ± 0.06, are consistent with unity within one error bar. Thus, no clear bias on the statistical errors of D^0 v_n results from the simultaneous fit is observed.

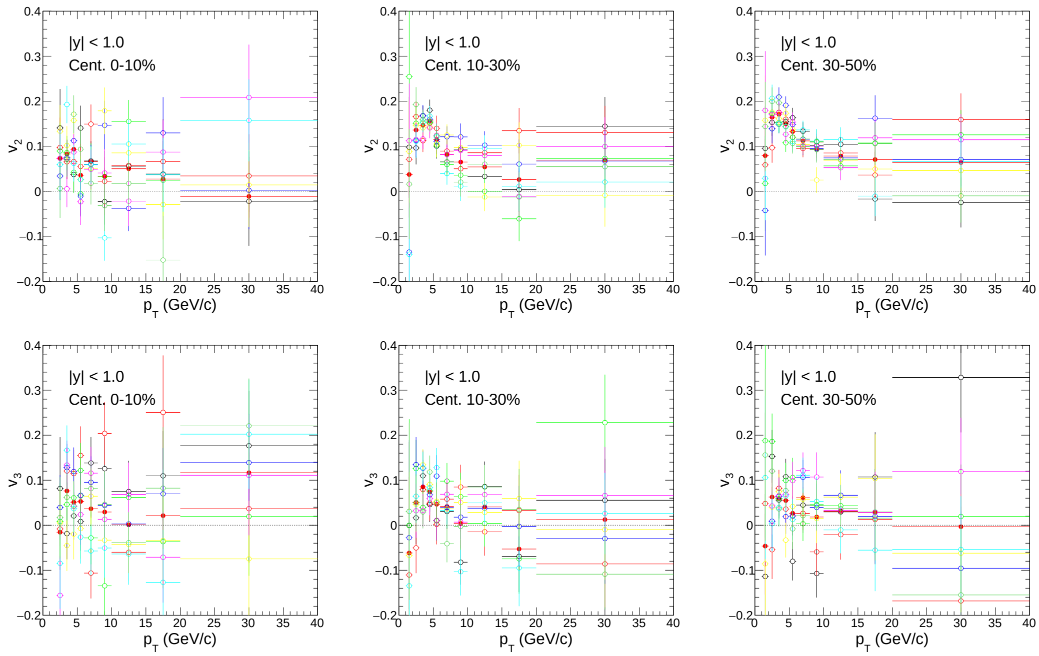

Figure 5.10.: v_2 (upper) and v_3 (lower) from all data (solid points) and 8 randomly divided subsets (empty points) for centrality 0-10% (left), 10-30% (middle) and 30-50% (right).

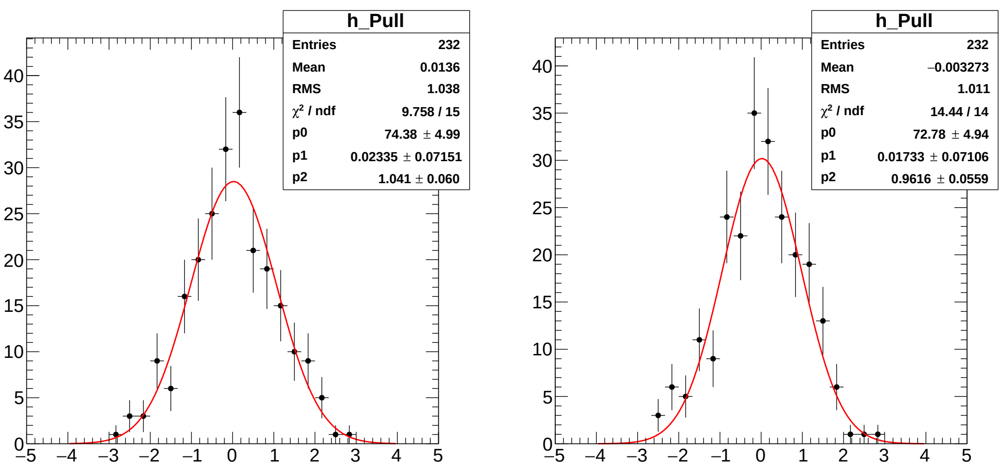

Figure 5.11.: Pull distributions for v_2 (left) and v_3 (right) from the 8 subsets showed in Figure 5.10 and 5.11. The distributions are fitted with Gaussian functions (read lines).

5.6 Results

Figure 5.12 shows the prompt D^0 meson v_2 (upper) and v_3 (lower) coefficients at midrapidity ($|y| < 1.0$) for the centrality classes 0–10% (left), 10–30% (middle), and 30–50% (right), and compares them to those of charged particles (dominated by light flavor hadrons) at midpseudorapidity ($|\eta| < 1.0$) [121]. The D^0 meson v_2 and v_3 coefficients increase with p_{T} to significantly positive values in the low-p_{T} region, and then decrease for higher p_{T}. For $p_{\mathrm{T}} < 6$ GeV/c, the comparison between the measured results and theoretical calculations suggests a collective motion of charm quarks as discussed below. For $p_{\mathrm{T}} > 6$ GeV/c, the D^0 meson v_2 values remain positive, suggesting a path length dependence of the charm quark energy loss; the D^0 meson v_3 precision is limited by the available data. Compared to those of charged particles, the D^0 meson v_2 and v_3 coefficients exhibit a similar p_{T} dependence, while the magnitudes are smaller for $p_{\mathrm{T}} < 6$ GeV/c for the centrality classes 10–30% and 30–50%. Further study may determine whether it is a pure mass ordering or whether other effects, such as the degree of charm quark thermalization, coalescence, and the path length dependence of energy loss, are at play. For $p_{\mathrm{T}} > 6$ GeV/c, the D^0 meson v_2 values are consistent with those of charged particles, suggesting that path length dependence of the charm quark energy loss is similar to that of light quarks. As has been observed for charged particles, the D^0 meson v_2 coefficient increases with decreasing centrality in the 0–50% centrality range, while the v_3 coefficient shows little centrality dependence. This is consistent with an increasing elliptical eccentricity with decreasing centrality [44], and an approximately constant triangularity stemming from geometry fluctuations [56].

Figure 5.12 also compares calculations from theoretical models [108, 116, 122–124] to the prompt D^0 meson v_2 and v_3 experimental results. The calculations from LBT [122], CUJET 3.0 [108], and SUBATECH [123] include collisional and radiative energy losses, while those from TAMU [124] and PHSD [116] include only collisional energy loss. Initial-state fluctuations [125] are included in the calculations from LBT,

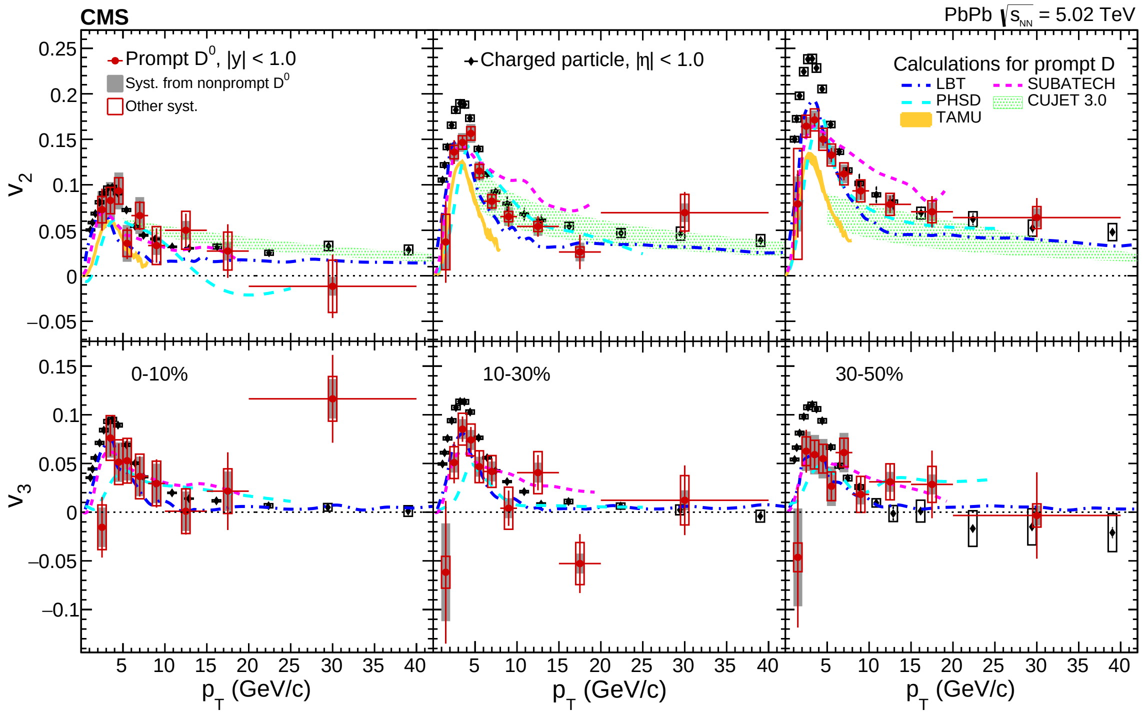

Figure 5.12.: Prompt D^0 meson v_2 (upper) and v_3 (lower) coefficients at midrapidity ($|y| < 1.0$) for the centrality classes 0–10% (left), 10–30% (middle), and 30–50% (right). The vertical bars represent statistical uncertainties, grey bands represent systematic uncertainties from nonprompt D^0 mesons and open boxes represent other systematic uncertainties. The measured v_n coefficient of charged particles at midpseudorapidity ($|\eta| < 1.0$) [121] and theoretical calculations for prompt D meson v_n coefficient [108, 116, 122–124] are also plotted for comparison.

SUBATECH, and PHSD; thus calculations for v_3 coefficient are only available from these three models. For $p_T < 6$ GeV/c, LBT, SUBATECH, TAMU, and PHSD can qualitatively describe the shapes of the measured v_2, while the TAMU model underestimates the v_2 values. This may suggest that the heavy quark potential in the TAMU model needs to be tuned [126] or that the addition of radiative energy loss is needed. The calculations from LBT and SUBATECH are in reasonable agreement with the v_3 results, while the PHSD calculations are systematically below the measured v_3 for centrality class 10–30%. In the calculations from LBT, SUBATECH, TAMU, and PHSD, the charm quarks have acquired significant elliptic and triangular flow through interactions with the medium constituents, and the coalescence mechanism is also incorporated. Without including the interactions between charm quarks and the medium, the calculations from these models will be significantly lower than the data results as showed in Fig. 5.13. Thus, the fact that the calculated v_n values are close or even lower than the measured results suggests that the charm quarks take part in the collective motion of the system. Whether and how well the D^0 anisotropy can be described by hydrodynamics and thermalization requires further investigation. For $p_{\mathrm{T}} > 6$ GeV/c, PHSD and CUJET can generally describe the v_2 results. LBT and SUBATECH predict lower and higher v_2 values than in data, respectively, indicating that improvements of the energy loss mechanisms in the two models are necessary.

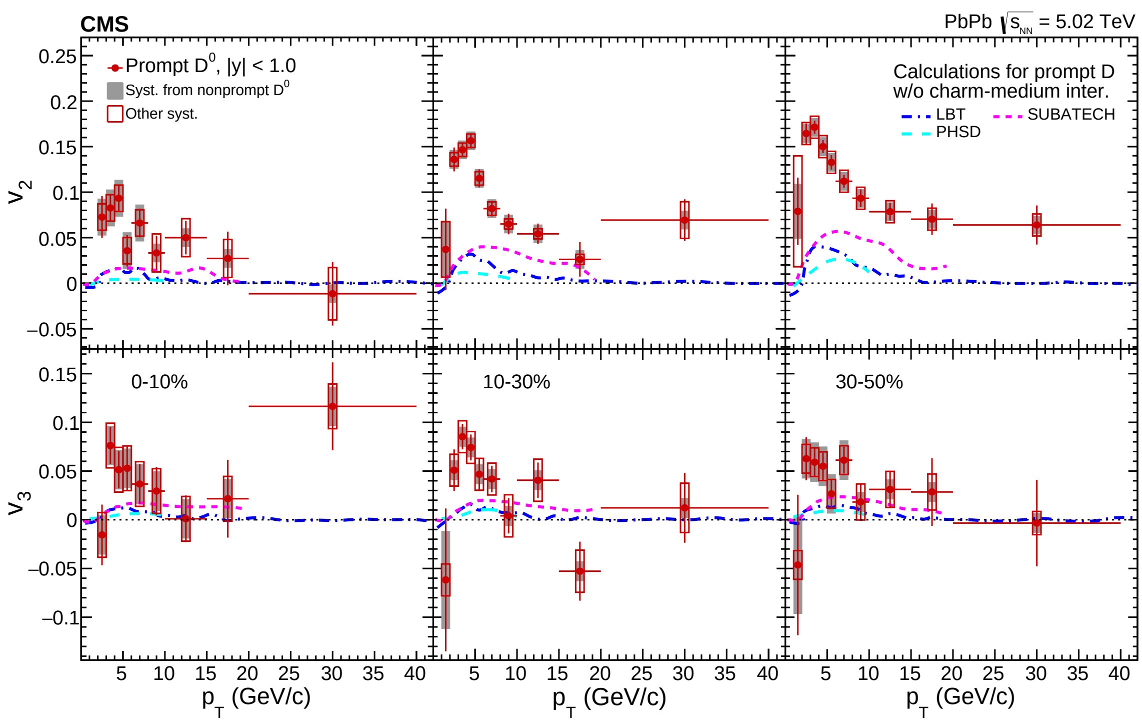

Figure 5.13.: The comparison of the D^0 meson v_2 (upper) and v_3 (lower) results and theoretical calculations removing the interactions between charm quarks and the medium for prompt D meson v_n coefficient [108, 116, 122–124].

The D^0 meson v_2 results are also compared with results from ALICE in PbPb collisions at 2.76 TeV [73] and 5.02 TeV [74] in Fig. 5.14, which shows the results are consistent within uncertainties.

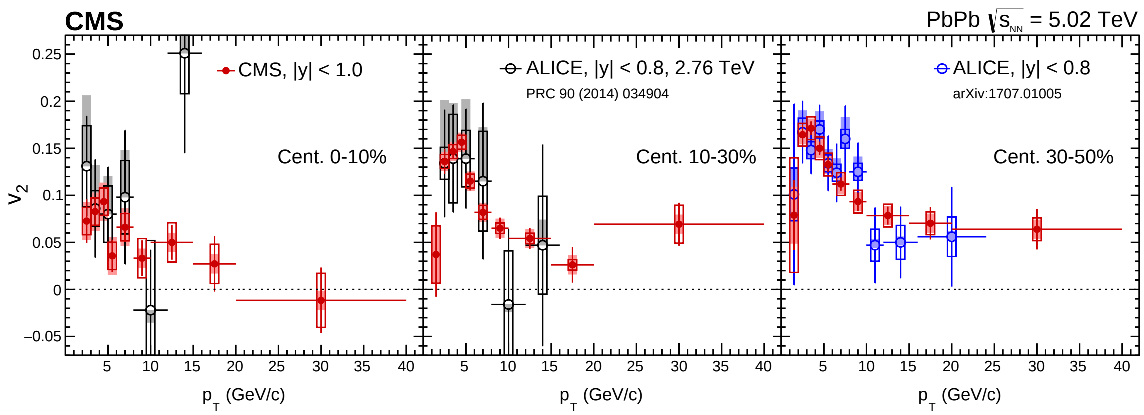

Figure 5.14.: The comparison of prompt D^0 meson v_2 from this analysis with results from ALICE in PbPb collisions at 2.76 TeV [73] and 5.02 TeV [74].

Figure 5.15 shows D^0 meson v_2 and v_3 from the SP method and $\Delta\phi$ bins method for centrality 0-10%, 10-30% and 30-50%. The results from the two methods are consistent within uncertainties.

In summary, the measurements of prompt D^0 meson azimuthal anisotropy coefficients v_2 and v_3 using the SP method in PbPb collisions at $\sqrt{s_{\mathrm{NN}}} = 5.02$ TeV have been presented. It is the first measurement of D^0 meson v_3 coefficient. The v_2 coefficient is found to be positive in the p_{T} range of 1 to 40 GeV/c, and positive v_3 values are observed for $p_{\mathrm{T}} < 6$ GeV/c. Centrality dependence is observed for v_2 coefficient, while v_3 coefficient shows little centrality dependence. Compared with those of charged particles, the measured D^0 meson v_2 and v_3 coefficients are found to be smaller for $p_{\mathrm{T}} < 6$ GeV/c. The v_2 values for $p_{\mathrm{T}} > 6$ GeV/c, which are consistent with those of charged particles, suggest that the path length dependence of charm quark energy loss is similar to that of light quarks. The comparison between the measured results and theoretical calculations suggests that the charm quarks take part in the

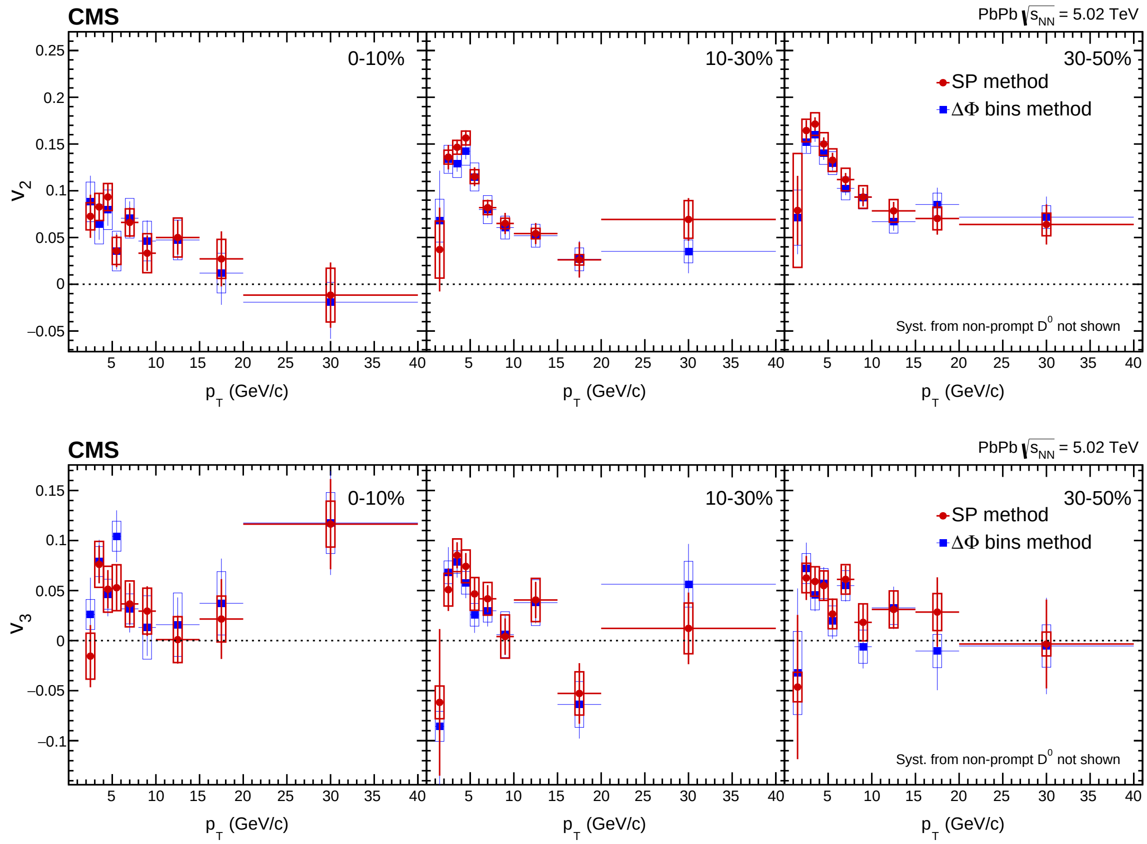

Figure 5.15.: D^0 meson v_2 (upper) and v_3 (lower) from SP method and $\Delta\phi$ bins method for centrality 0-10% (left), 10-30% (middle) and 30-50% (right).

collective motion of the system. The results provide new constraints on theories of the interactions between charm quarks and the QGP medium, and the charm quark energy loss mechanisms.

6. Summary

In summary, the measurements of prompt D^0 meson nuclear modification factor R_{AA} and azimuthal anisotropy coefficients v_2 and v_3 in PbPb collisions with the CMS tector have been presented. It is the first measurement of the D^0 meson v_3.

The R_{AA} results show that the production of prompt D^0 mesons are strongly suppressed in semi-central to central PbPb collisions. The suppression have strong dependences on centrality and p_{T}. The D^0 meson R_{AA} is consistent with that of light hadrons for $p_{\mathrm{T}} > 5$ GeV/c, while a hint that D^0 R_{AA} is higher than light hadron R_{AA} is observed for $p_{\mathrm{T}} < 5$ GeV/c. The D^0 meson R_{AA} is consistent with the $B^{\pm}$ meson R_{AA} in the pt range of 7–50 GeV/c, but the uncertainties on the $B^{\pm}$ meson results are stil large. Compared with that of nonprompt J/ψ meson, the D^0 meson R_{AA} is significantly lower for $p_{\mathrm{T}} < 10$ GeV/c. These comparisons provide important information on differences of the energy loss of different flavors.

The prompt D^0 meson v_2 coefficient is found to be positive in the measured p_{T} range of 1–40 GeV/c, and the v_2 is found to be positive for $p_{\mathrm{T}} < 6$ GeV/c. Centrality dependence is observed for v_2 coefficient, while v_3 coefficient shows little centrality dependence. Compared with those of light hadrons, the prompt D^0 meson v_2 and v_3 values are found to be smaller for $p_{\mathrm{T}} < 6$ GeV/c, while have a similar p_{T} dependence. The v_2 values are consistent with those of charged particles for p_{T} > 6 GeV/c, suggesting that the path length dependence of charm quark energy loss is similar to that of light quarks. The comparison between the light hadron and D^0 results provide essential insights into the interaction strength between the charm quarks and the QGP medium. Through the comparison with theoretical calculations, the v_2 and v_3 results at low p_{T} suggests that the charm quarks take part in the collective motion of the system.

These measurements show that the charm quarks strongly interact with the QGP medium. Comparison between the results of heavy flavor and light hadrons provide important inputs on the differences of interactions with the QGP of different flavors. The D^0 meson R_{AA}, v_2, and v_3 results provide important constraints on the models of the interactions between the charm quarks and the QGP medium, and the charm quark energy loss mechanisums. The work presented in this thesis allows us to set an important milestone in our understanding of the interactions between the charm quarks and the QGP medium.

REFERENCES

REFERENCES

[1] S. L. Glashow. Partial Symmetries of Weak Interactions. *Nucl. Phys.*, 22:579–588, 1961.

[2] Steven Weinberg. A Model of Leptons. *Phys. Rev. Lett.*, 19:1264–1266, 1967.

[3] Abdus Salam. Weak and Electromagnetic Interactions. *Conf. Proc. C*, 680519:367–377, 1968.

[4] C. Patrignani et al. Review of Particle Physics. *Chin. Phys. C*, 40(10):100001, 2016.

[5] `https://en.wikipedia.org/wiki/Standard_Model`.

[6] Serguei Chatrchyan et al. Observation of a new boson at a mass of 125 GeV with the CMS experiment at the LHC. *Phys. Lett. B*, 716:30–61, 2012.

[7] Georges Aad et al. Observation of a new particle in the search for the Standard Model Higgs boson with the ATLAS detector at the LHC. *Phys. Lett. B*, 716:1–29, 2012.

[8] Peter W. Higgs. Broken Symmetries and the Masses of Gauge Bosons. *Phys. Rev. Lett.*, 13:508–509, 1964.

[9] `http://web.mit.edu/sahughes/www/8.022/lec01.pdf`.

[10] M. Y. Han and Yoichiro Nambu. Three Triplet Model with Double SU(3) Symmetry. *Phys. Rev.*, 139:B1006–B1010, 1965.

[11] H. David Politzer. Reliable Perturbative Results for Strong Interactions? *Phys. Rev. Lett.*, 30:1346–1349, 1973.

[12] Jeff Greensite. An introduction to the confinement problem. *Lect. Notes Phys.*, 821:1–211, 2011.

[13] David J. Gross and Frank Wilczek. Ultraviolet Behavior of Nonabelian Gauge Theories. *Phys. Rev. Lett.*, 30:1343–1346, 1973.

[14] Siegfried Bethke. Experimental tests of asymptotic freedom. *Prog. Part. Nucl. Phys.*, 58:351–386, 2007.

[15] A. Bazavov et al. Equation of state and QCD transition at finite temperature. *Phys. Rev. D*, 80:014504, 2009.

[16] Edward V. Shuryak. Theory of Hadronic Plasma. *Sov. Phys. JETP*, 47:212–219, 1978. [Zh. Eksp. Teor. Fiz.74,408(1978)].

[17] John C. Collins and M. J. Perry. Superdense Matter: Neutrons Or Asymptotically Free Quarks? *Phys. Rev. Lett.*, 34:1353, 1975.

[18] Szabolcs Borsanyi, Gergely Endrodi, Zoltan Fodor, Antal Jakovac, Sandor D. Katz, Stefan Krieg, Claudia Ratti, and Kalman K. Szabo. The QCD equation of state with dynamical quarks. *JHEP*, 11:077, 2010.

[19] F. Karsch and E. Laermann. Thermodynamics and in medium hadron properties from lattice QCD. pages 1–59, 2003.

[20] J. Adams et al. Experimental and theoretical challenges in the search for the quark gluon plasma: The STAR collaboration's critical assessment of the evidence from RHIC collisions. *Nucl. Phys. A*, 757:102, 2005.

[21] K. Adcox et al. Formation of dense partonic matter in relativistic nucleus-nucleus collisions at RHIC: Experimental evaluation by the PHENIX collaboration. *Nucl. Phys. A*, 757:184, 2005.

[22] I. Arsene et al. Quark gluon plasma and color glass condensate at RHIC? The perspective from the BRAHMS experiment. *Nucl. Phys. A*, 757:1, 2005.

[23] B. B. Back et al. The PHOBOS perspective on discoveries at RHIC. *Nucl. Phys. A*, 757:28, 2005.

[24] B. Muller, J. Schukraft, and B. Wyslouch. First results from Pb+Pb collisions at the LHC. *Ann. Rev. Nucl. Part. Sci.*, 62:361, 2012.

[25] N. Armesto and E. Scomparin. Heavy-ion collisions at the Large Hadron Collider: a review of the results from Run 1. *Eur. Phys. J. Plus*, 131:52, 2016.

[26] Yasuyuki Akiba et al. The Hot QCD White Paper: Exploring the Phases of QCD at RHIC and the LHC. 2015.

[27] Michael L. Miller, Klaus Reygers, Stephen J. Sanders, and Peter Steinberg. Glauber modeling in high energy nuclear collisions. *Ann. Rev. Nucl. Part. Sci.*, 57:205, 2007.

[28] Serguei Chatrchyan et al. Dependence on pseudorapidity and centrality of charged hadron production in PbPb collisions at a nucleon-nucleon centre-of-mass energy of 2.76 TeV. *JHEP*, 08:141, 2011.

[29] Roger D. Woods and David S. Saxon. Diffuse Surface Optical Model for Nucleon-Nuclei Scattering. *Phys. Rev.*, 95:577–578, 1954.

[30] `http://www.staff.science.uu.nl/~misch101/research.htm`.

[31] Miklos Gyulassy and Michael Plumer. Jet Quenching in Dense Matter. *Phys. Lett.*, B243:432–438, 1990.

[32] R. Baier, Yuri L. Dokshitzer, Alfred H. Mueller, S. Peigne, and D. Schiff. Radiative energy loss and p_{T} broadening of high-energy partons in nuclei. *Nucl. Phys.*, B484:265–282, 1997.

[33] Jorge Casalderrey-Solana and Carlos A. Salgado. Introductory lectures on jet quenching in heavy ion collisions. *Acta Phys. Polon. B*, 38:3731–3794, 2007.

[34] J. D. Bjorken. Energy Loss of Energetic Partons in Quark - Gluon Plasma: Possible Extinction of High p_T Jets in Hadron - Hadron Collisions. 1982.

[35] Markus H. Thoma and Miklos Gyulassy. Quark Damping and Energy Loss in the High Temperature QCD. *Nucl. Phys.*, B351:491–506, 1991.

[36] K. J. Eskola, H. Paukkunen, and C. A. Salgado. EPS09: A New Generation of NLO and LO Nuclear Parton Distribution Functions. *JHEP*, 04:065, 2009.

[37] Michele Arneodo. Nuclear effects in structure functions. *Phys. Rept.*, 240:301–393, 1994.

[38] L. L. Frankfurt and M. I. Strikman. Hard Nuclear Processes and Microscopic Nuclear Structure. *Phys. Rept.*, 160:235–427, 1988.

[39] Vardan Khachatryan et al. Nuclear Effects on the Transverse Momentum Spectra of Charged Particles in pPb Collisions at $\sqrt{s_{_\mathrm{NN}}} = 5.02$ TeV. *Eur. Phys. J. C*, 75(5):237, 2015.

[40] Betty Bezverkhny Abelev et al. Transverse momentum dependence of inclusive primary charged-particle production in p-Pb collisions at $\sqrt{s_\mathrm{NN}} = 5.02$ TeV. *Eur. Phys. J. C*, 74(9):3054, 2014.

[41] Georges Aad et al. Transverse momentum, rapidity, and centrality dependence of inclusive charged-particle production in $\sqrt{s_{NN}} = 5.02$ TeV p + Pb collisions measured by the ATLAS experiment. *Phys. Lett. B*, 763:313–336, 2016.

[42] Vardan Khachatryan et al. Charged-particle nuclear modification factors in PbPb and pPb collisions at $\sqrt{s_{_\mathrm{NN}}} = 5.02$TeV. *JHEP*, 04:039, 2017.

[43] Serguei Chatrchyan et al. Study of high-pT charged particle suppression in PbPb compared to pp collisions at $\sqrt{s_{NN}} = 2.76$ TeV. *Eur. Phys. J. C*, 72:1945, 2012.

[44] S. Chatrchyan et al. Measurement of the elliptic anisotropy of charged particles produced in PbPb collisions at $\sqrt{s_{_\mathrm{NN}}} = 2.76$TeV. *Phys. Rev. C*, 87:014902, 2013.

[45] Edward V. Shuryak. What RHIC experiments and theory tell us about properties of quark-gluon plasma? *Nucl. Phys. A*, 750:64, 2005.

[46] Miklos Gyulassy and Larry McLerran. New forms of QCD matter discovered at RHIC. *Nucl. Phys. A*, 750:30, 2005.

[47] Arthur M. Poskanzer and S. A. Voloshin. Methods for analyzing anisotropic flow in relativistic nuclear collisions. *Phys. Rev. C*, 58:1671, 1998.

[48] M. Gyulassy, I. Vitev, and X. N. Wang. High p_T Azimuthal Asymmetry in Noncentral $A + A$ at RHIC. *Phys. Rev. Lett.*, 86:2537, 2001.

[49] E. V. Shuryak. Azimuthal asymmetry at large p_t seem to be too large for a "jet quenching". *Phys. Rev. C*, 66:027902, 2002.

[50] Zhi Qiu. *Event-by-event Hydrodynamic Simulations for Relativistic Heavy-ion Collisions.* PhD thesis, Ohio State U., 2013.

[51] B. Alver et al. Event-by-Event Fluctuations of Azimuthal Particle Anisotropy in Au + Au Collisions at $\sqrt{s_{NN}} = 200$ GeV. *Phys. Rev. Lett.*, 104:142301, 2010.

[52] Zhi Qiu and Ulrich W. Heinz. Event-by-event shape and flow fluctuations of relativistic heavy-ion collision fireballs. *Phys. Rev. C*, 84:024911, 2011.

[53] Hannu Holopainen, Harri Niemi, and Kari J. Eskola. Event-by-event hydrodynamics and elliptic flow from fluctuating initial state. *Phys. Rev. C*, 83:034901, 2011.

[54] Hannah Petersen, Guang-You Qin, Steffen A. Bass, and Berndt Muller. Triangular flow in event-by-event ideal hydrodynamics in Au+Au collisions at $\sqrt{s_{\rm NN}} = 200A$ GeV. *Phys. Rev. C*, 82:041901, 2010.

[55] Fernando G. Gardim, Frederique Grassi, Matthew Luzum, and Jean-Yves Ollitrault. Mapping the hydrodynamic response to the initial geometry in heavy-ion collisions. *Phys. Rev. C*, 85:024908, 2012.

[56] S. Chatrchyan et al. Measurement of higher-order harmonic azimuthal anisotropy in PbPb collisions at $\sqrt{s_{\rm NN}} = 2.76$TeV. *Phys. Rev. C*, 89:044906, 2014.

[57] P. Braun-Munzinger. Quarkonium production in ultra-relativistic nuclear collisions: Suppression versus enhancement. *J. Phys. G*, 34:S471, 2007.

[58] F.-M. Liu and S.-X. Liu. Quark-gluon plasma formation time and direct photons from heavy ion collisions. *Phys. Rev. C*, 89:034906, 2014.

[59] Yuri L. Dokshitzer and D. E. Kharzeev. Heavy quark colorimetry of QCD matter. *Phys. Lett. B*, 519:199, 2001.

[60] Nestor Armesto, Carlos A. Salgado, and Urs Achim Wiedemann. Medium induced gluon radiation off massive quarks fills the dead cone. *Phys. Rev. D*, 69:114003, 2004.

[61] A. Andronic et al. Heavy-flavour and quarkonium production in the LHC era: from proton-proton to heavy-ion collisions. *Eur. Phys. J. C*, 76:107, 2016.

[62] Magdalena Djordjevic. Collisional energy loss in a finite size QCD matter. *Phys. Rev. C*, 74:064907, 2006.

[63] Azfar Adil and Ivan Vitev. Collisional dissociation of heavy mesons in dense QCD matter. *Phys. Lett. B*, 649:139–146, 2007.

[64] D. Molnar and S. A. Voloshin. Elliptic Flow at Large Transverse Momenta from Quark Coalescence. *Phys. Rev. Lett.*, 91:092301, 2003.

[65] V. Greco, C. M. Ko, and P. Lévai. Parton Coalescence and Antiproton/Pion Anomaly at RHIC. *Phys. Rev. Lett.*, 90:202302, 2003.

[66] Nuclear Modification Factor of prompt D^0 in PbPb Collisions at $\sqrt{s_{\rm NN}} = 2.76$ TeV. Technical Report CMS-PAS-HIN-15-005, CERN, Geneva, 2015.

[67] Albert M Sirunyan et al. Nuclear modification factor of D^0 mesons in PbPb collisions at $\sqrt{s_{\rm NN}} = 5.02$TeV. Submitted to Phys. Lett. B, 2017.

[68] Albert M Sirunyan et al. Measurement of prompt D^0 meson azimuthal anisotropy in PbPb collisions at $\sqrt{s_{NN}} = 5.02$ TeV. Accepted by Phys. Rev. Lett., 2017.

[69] L. Adamczyk et al. Observation of D^0 Meson Nuclear Modifications in Au+Au Collisions at $\sqrt{s_{\mathrm{NN}}} = 200$GeV. *Phys. Rev. Lett.*, 113:142301, 2014.

[70] L. Adamczyk et al. Measurement of D^0 Azimuthal Anisotropy at Midrapidity in Au + Au Collisions at $\sqrt{s_{\mathrm{NN}}} = 200$GeV. *Phys. Rev. Lett.*, 118:212301, 2017.

[71] J. Adam et al. Centrality dependence of high-p_{T} D meson suppression in Pb-Pb collisions at $\sqrt{s_{\mathrm{NN}}} = 2.76$TeV. *JHEP*, 11:205, 2015.

[72] J. Adam et al. Transverse momentum dependence of D-meson production in Pb-Pb collisions at $\sqrt{s_{\mathrm{NN}}} = 2.76$TeV. *JHEP*, 03:081, 2016.

[73] B. Bezverkhny Abelev et al. Azimuthal anisotropy of D meson production in Pb-Pb collisions at $\sqrt{s_{\mathrm{NN}}} = 2.76$TeV. *Phys. Rev. C*, 90:034904, 2014.

[74] Shreyasi Acharya et al. *D*-meson azimuthal anisotropy in midcentral Pb-Pb collisions at $\sqrt{\mathbf{s}_{\mathrm{NN}}} = \mathbf{5.02}$ TeV. *Phys. Rev. Lett.*, 120(10):102301, 2018.

[75] Betty Bezverkhny Abelev et al. Measurement of prompt *D*-meson production in $p - Pb$ collisions at $\sqrt{s_{NN}} = 5.02$ TeV. *Phys. Rev. Lett.*, 113(23):232301, 2014.

[76] S. Chatrchyan et al. The CMS Experiment at the CERN LHC. *JINST*, 3:S08004, 2008.

[77] Serguei Chatrchyan et al. Description and performance of track and primary-vertex reconstruction with the CMS tracker. *JINST*, 9(10):P10009, 2014.

[78] A Dominguez, D Abbaneo, K Arndt, N Bacchetta, A Ball, E Bartz, W Bertl, G M Bilei, G Bolla, H W K Cheung, M Chertok, S Costa, N Demaria, Daniel Dominguez Vazquez, K Ecklund, W Erdmann, K Gill, G Hall, K Harder, F Hartmann, R Horisberger, W Johns, H C Kaestli, K Klein, D Kotlinski, S Kwan, M Pesaresi, H Postema, T Rohe, C Schfer, A Starodumov, S Streuli, A Tricomi, P Tropea, J Troska, F Vasey, and W Zeuner. CMS Technical Design Report for the Pixel Detector Upgrade. Technical Report CERN-LHCC-2012-016. CMS-TDR-11, Sep 2012. Additional contacts: Jeffrey Spalding, Fermilab, Jeffrey.Spalding@cern.ch Didier Contardo, Universite Claude Bernard-Lyon I, didier.claude.contardo@cern.ch.

[79] S. Dasu et al. CMS. The TriDAS project. Technical design report, vol. 1: The trigger systems. 2000.

[80] P. Sphicas et al. CMS: The TriDAS project. Technical design report, Vol. 2: Data acquisition and high-level trigger. 2002.

[81] Claudio Grandi, David Stickland, Lucas Taylor, Achille Petrilli, and Alain Herv. CMS Computing Model: The "CMS Computing Model RTAG". Technical Report CMS-NOTE-2004-031. CERN-LHCC-2004-035. LHCC-G-083, CERN, Geneva, Dec 2004.

[82] `https://twiki.cern.ch/twiki/bin/view/CMSPublic/WorkBookComputingModel`.

[83] Particle Data Group, C. Patrignani, et al. Review of Particle Physics. *Chin. Phys. C*, 40:100001, 2016.

[84] G. E. Forden and D. H. Saxon. Improving vertex position determination by using a kinematic fit. *Nucl. Instrum. Meth. A*, 248:439, 1986.

[85] Helge Voss, Andreas Höcker, Jörg Stelzer, and Frerik Tegenfeldt. TMVA, the toolkit for multivariate data analysis with ROOT. In *XIth International Workshop on Advanced Computing and Analysis Techniques in Physics Research (ACAT)*, page 40, 2007.

[86] CMS. Observation and studies of jet quenching in pbpb collisions at $\sqrt{s_{NN}} = 2.76$ tev. *Phys. Rev. C*, 2011.

[87] Serguei Chatrchyan et al. Studies of jet quenching using isolated-photon+jet correlations in PbPb and pp collisions at $\sqrt{s_{NN}} = 2.76$ TeV. 2012.

[88] Serguei Chatrchyan et al. Jet momentum dependence of jet quenching in PbPb collisions at $\sqrt{s_{NN}}$=2.76 TeV. 2012.

[89] Serguei Chatrchyan et al. Measurement of jet fragmentation into charged particles in pp and PbPb collisions at $\sqrt{s_{NN}}$= 2.76 TeV. 2012.

[90] Serguei Chatrchyan et al. Observation and studies of jet quenching in PbPb collisions at $\sqrt{s_{NN}}$=2.76 TeV. *Phys. Rev. C*, 84:024906, 2011.

[91] Torbjörn Sjöstrand, Stephen Mrenna, and Peter Skands. PYTHIA 6.4 physics and manual. *JHEP*, 05:026, 2006.

[92] Rick Field. Early LHC Underlying Event Data - Findings and Surprises. 2010.

[93] I. P. Lokhtin and A. M. Snigirev. A model of jet quenching in ultrarelativistic heavy ion collisions and high-p_{T} hadron spectra at RHIC. *Eur. Phys. J. C*, 45:211, 2006.

[94] D.J. Lange. The EvtGen particle decay simulation package. *Nucl. Instrum. Meth. A*, 462:152–155, 2001.

[95] Matteo Cacciari, Mario Greco, and Paolo Nason. The p_{T} spectrum in heavy flavor hadroproduction. *JHEP*, 05:007, 1998.

[96] Matteo Cacciari, Stefano Frixione, and Paolo Nason. The p(T) spectrum in heavy flavor photoproduction. *JHEP*, 03:006, 2001.

[97] CMS Collaboration. Prompt and non-ptompt $j/\psi r_{AA}$ with 150 μb^{-1} integrated pbpb luminosity at $\sqrt{s_{NN}} = 2.76$ tev. *CMS PAS HIN-12-014*, 2012.

[98] Serguei Chatrchyan et al. Evidence of b-Jet Quenching in PbPb Collisions at $\sqrt{s_{NN}} = 2.76..$TeV. *Phys.Rev.Lett.*, 113(13):132301, 2014.

[99] B. Abelev et al. Measurement of charm production at central rapidity in proton-proton collisions at $\sqrt{s} = 7$ TeV. *JHEP*, 1201:128, 2012.

[100] R. Averbeck, N. Bastid, Z. Conesa del Valle, P. Crochet, A. Dainese, and X. Zhang. Reference heavy flavour cross sections in pp collisions at sqrt (s)= 2.76 TeV, using a pQCD-driven sqrt (s)-scaling of ALICE measurements at sqrt (s)= 7 TeV. 2011.

[101] CMS Collaboration. Measurement of tracking efficiency. CMS Physics Analysis Summary CMS-PAS-TRK-10-002, 2010.

[102] Serguei Chatrchyan et al. Observation and studies of jet quenching in PbPb collisions at nucleon-nucleon center-of-mass energy = 2.76 TeV. *Phys.Rev. C*, 84:024906, 2011.

[103] et. al. Abalev, B. Suppression of high transverse momentum D mesons in central PbPb collisions at $\sqrt{s_{NN}} = 2.76$ TeV. *JHEP*, 09:112, 2012.

[104] B. A. Kniehl, G. Kramer, I. Schienbein, and H. Spiesberger. Inclusive $D^{*\pm}$ production in $p\bar{p}$ collisions with massive charm quarks. *Phys. Rev. D*, 71:014018, 2005.

[105] B. A. Kniehl, G. Kramer, I. Schienbein, and H. Spiesberger. Collinear subtractions in hadroproduction of heavy quarks. *Eur. Phys. J. C*, 41:199, 2005.

[106] B. A. Kniehl, G. Kramer, I. Schienbein, and H. Spiesberger. Inclusive charmed-meson production at the CERN LHC. *Eur. Phys. J. C*, 72:2082, 2012.

[107] Magdalena Djordjevic and Marko Djordjevic. Predictions of heavy-flavor suppression at 5.1TeVPb+Pb collisions at the CERN Large Hadron Collider. *Phys. Rev. C*, 92:024918, 2015.

[108] J. Xu, J. Liao, and M. Gyulassy. Bridging soft-hard transport properties of quark-gluon plasmas with CUJET3.0. *JHEP*, 02:169, 2016. And private communication.

[109] Jiechen Xu, Alessandro Buzzatti, and Miklos Gyulassy. Azimuthal jet flavor tomography with CUJET2.0 of nuclear collisions at RHIC and LHC. *JHEP*, 08:063, 2014.

[110] Jiechen Xu, Jinfeng Liao, and Miklos Gyulassy. Consistency of perfect fluidity and jet quenching in semi-quark-gluon monopole plasmas. *Chin. Phys. Lett.*, 32:092501, 2015.

[111] Zhong-Bo Kang, Robin Lashof-Regas, Grigory Ovanesyan, Philip Saad, and Ivan Vitev. Jet quenching phenomenology from soft-collinear effective theory with Glauber gluons. *Phys. Rev. Lett.*, 114:092002, 2015.

[112] Yang-Ting Chien, Alexander Emerman, Zhong-Bo Kang, Grigory Ovanesyan, and Ivan Vitev. Jet quenching from QCD evolution. *Phys. Rev. D*, 93:074030, 2016.

[113] Shanshan Cao, Tan Luo, Guang-You Qin, and Xin-Nian Wang. Linearized Boltzmann transport model for jet propagation in the quark-gluon plasma: Heavy quark evolution. *Phys. Rev. C*, 94:014909, 2016.

[114] S. Cao, T. Luo, G.-Y. Qin, and X.-N. Wang. Heavy and light flavor jet quenching at RHIC and LHC energies. 2017.

[115] Taesoo Song, Hamza Berrehrah, Daniel Cabrera, Juan M. Torres-Rincon, Laura Tolos, Wolfgang Cassing, and Elena Bratkovskaya. Tomography of the quark-gluon-plasma by charm quarks. *Phys. Rev. C*, 92:014910, 2015.

[116] T. Song, H. Berrehrah, D. Cabrera, W. Cassing, and E. Bratkovskaya. Charm production in Pb+Pb collisions at energies available at the CERN Large Hadron Collider. *Phys. Rev. C*, 93:034906, 2016. And private communication.

[117] W. A. Horowitz. Fluctuating heavy quark energy loss in a strongly coupled quark-gluon plasma. *Phys. Rev. D*, 91:085019, 2015.

[118] CMS Collaboration. Measurement of $B^{+/-}$ meson differential production cross sections in pp and PbPb collisions at $\sqrt{s_{NN}} = 5.02$TeV. *Phys. Rev. Lett.*, 119:152301, Oct 2017.

[119] CMS Collaboration. Measurement of prompt and nonprompt charmonium suppression in pbpb collisions at 5.02 tev. Submitted to Eur. Phys. J. C, 2017.

[120] M. Luzum and J.-Y. Ollitrault. Eliminating experimental bias in anisotropic-flow measurements of high-energy nuclear collisions. *Phys. Rev. C*, 87:044907, 2013.

[121] A. M. Sirunyan et al. Azimuthal anisotropy of charged particles with transverse momentum up to 100 GeV/ c in PbPb collisions at $\sqrt{s_{\mathrm{NN}}} = 5.02$TeV. *Phys. Lett. B*, 776:195, 2018.

[122] S. Cao, T. Luo, G.-Y. Qin, and X.-N. Wang. Linearized Boltzmann transport model for jet propagation in the quark-gluon plasma: Heavy quark evolution. *Phys. Rev. C*, 94:014909, 2016. And private communication.

[123] M. Nahrgang, J. Aichelin, S. Bass, P. B. Gossiaux, and K. Werner. Elliptic and triangular flow of heavy flavor in heavy-ion collisions. *Phys. Rev. C*, 91:014904, 2015. And private communication.

[124] M. He, R. J. Fries, and R. Rapp. Heavy flavor at the large hadron collider in a strong coupling approach. *Phys. Lett. B*, 735:445, 2014. And private communication.

[125] B. Alver and G. Roland. Collision geometry fluctuations and triangular flow in heavy-ion collisions. *Phys. Rev. C*, 81:054905, 2010.

[126] Shuai Y. F. Liu and Ralf Rapp. An in-medium heavy-quark potential from the $Q\bar{Q}$ free energy. *Nucl. Phys. A*, 941:179, 2015.

VITA

VITA

Jian Sun graduated from University of Science and Technology of China in May 2011 with a Bachelor of Science Degree in Physics. He pursued his graduate study in Purdue University from 2011 to 2018. Jian joined the high energy nuclear physics group under Prof. Wei Xie, as a member of the CMS Collaboration. He worked on studies of open heavy flavor production and azimuthal anisotropy in heavy ion collisions. Jian will graduate from Purdue University with a Ph.D. in Physics in 2018.